DESIGN, EVALUATION, AND MODELING OF MEDIUM VOLTAGE DC ENERGY CONVERSION TESTBED WITH EMPHASIS ON ELECTROCHEMICAL ENERGY STORAGE

by

DAVID A. DODSON

Presented to the Faculty of the Graduate School of
The University of Texas at Arlington in Partial Fulfillment
of the Requirements
for the Degree of

DOCTOR OF PHILOSOPHY

THE UNIVERSITY OF TEXAS AT ARLINGTON
May 2019

To everybody that has been around all these years that I have been working on my studies, including my father Dereck, my mother Stacey, my brothers Glenn and Roger, and everyone who has mentored me and helped me develop into the person that I am today.

Thank you to David, Matt, Clint, Derek, Chris, Isaac, Brian, Jacob, Chaz, Caroline, and Alex.

ACKNOWLEDGEMENTS

I would like to thank all of the faculty that I have developed such a meaningful professional and personal relationship with over the last eight years that I have spent at the University of Texas at Arlington. Without the guidance, knowledge, and experience I have received through my time with Dr. Wei-Jen Lee, Dr. Rasool Kanarangui, Dr. William Dillon, and Dr. Ali Davoudi, I would not have been able to accomplish the tasks that I have here. I am so appreciative of everyone's dedication to the field of electrical engineering and their passion for educating the next generation of engineers. My time in the Pulsed Power & Energy Laboratory under the guidance of Dr. David Wetz and Dr. Gregory Turner has helped me develop into the engineer that I am today. I want to give so much thanks and appreciation to my family for supporting and believing in me and the importance of the education I have been pursuing. Thank you to everyone that has helped me through everything!

April 2nd, 2019

ABSTRACT

DESIGN, EVALUATION, AND MODELING OF MEDIUM VOLTAGE DC ENERGY CONVERSION TESTBED WITH EMPHASIS ON ELECTROCHEMICAL ENERGY STORAGE

DAVID A. DODSON, Ph.D.

The University of Texas at Arlington, 2019

Supervising Professor: David A. Wetz

Much work has been done in recent years regarding the emphasis and newfound importance of energy storage and energy conversion within systems that, at one time, functioned off of simple alternating current (AC) busses. With the advancement in technology has come unique and demanding electrical loads and equipment, creating a need for many different electrical topologies and requirements. The scope of the work done here is related to current efforts and interests in islanded microgrid power systems. Microgrid electrical systems are evolving and new, demanding electrical systems are being invented and introduced. For example, advancements in communication and sensor systems has brought with it increasing electrical demands, specifically demands that occur in a transient manner. With these new electrical demands placed upon the islanded power system of a microgrid, new system topologies have risen up to meet these unique and transient requirements. Some of these topologies include the presence of medium voltage DC distribution busses within these systems to supply these new loads efficiently, as well as the inclusion and integration

of energy storage used to augment traditional rotational generation in the event that a high power transient electrical load is placed upon the system.

The inclusion of these topological changes has shown a need for modeling and evaluation of these newer, more complex systems. As these power systems become more complicated, there is an increasing number of variables that need to be considered in the integration of new systems. Energy conversion is important between the different, growing numbers of busses in place, and the evaluation of the different interactions between these busses has proven to be an expensive and difficult task to perform at the full multi-megawatt level of a typical commercial microgrid power system.

The work presented here is to create a testbed of equipment and controls that are representative of this modern power system architecture, including a multitude of busses with both AC and DC voltages at different levels. These different voltage levels are to be tied together with various power electronic converters, such that energy can be transferred around the system as needed. Many different electrical loads will be implemented, in the form of traditional constant base loads and varying, transient loads of different pulse shapes and characteristics. The interactions and implications these loads have with the power system as a whole will be studied, including impacts on power quality and efficiency. These systems will operate at a power level that is more attainable than the multi-megawatt microgrid power system level, but one that is still significant enough to offer valuable insight into the operation of real, representative equipment. The power range utilized throughout this system will be between 100 and 300 kW, operating at voltages including 480 VAC 3Ø, 4160 VAC 3Ø, 1000 VDC, 6000 VDC, 12000 VDC.

The specification of equipment will be presented here, along with a fundamental model of the system for analysis.

TABLE OF CONTENTS

LIST OF ILLUSTRATIONS

LIST OF TABLES

CHAPTER 1

INTRODUCTION

1.1 Modern Power Systems

Modern power systems are becoming increasingly technologically advanced and complex. With increase in complexity of the systems located within islanded platforms, more complex supporting power systems have become critically important. Microgrids are islanded systems, meaning that they do not have the benefit of being interconnected to a much larger and stronger power system or grid. Due to this islanded nature, the primary source of power for the microgrid systems is local, non-stiff generation sources. These sources are typically large gas turbine or diesel generators. Due to the operational nature of these generators, there are limitations on the generation capabilities and, more specifically, the output slew rates. Modern electrical loads, which will be discussed in further detail later, are often much more transient in nature than previous systems. Because of this, the limited slew rates available for the traditional rotational generation sources must be considered and compensated for. Another challenge for these generation sources located in islanded systems is the critical need for the local generation to support these newer, transient and highly demanding loads while still supporting the base loads. These base loads are things like lighting, HVAC, communication systems, etc.

Electrical loads are changing as modern systems transition towards high power, transiently operated loads. These can be things ranging from high energy radar and communication systems to new, complex electrical loads that are still being developed. These loads may require power at levels over what is available from the traditional

rotational generation sources within an islanded system, but only for a short duration. These extreme slew rates and power demands that exceed the capabilities of conventional generation have brought the need for alternative generation systems in order to maintain acceptable power system operation and power quality.

This transient, severe loading has a very negative impact on the operation of the generation sources. Transient loading of the generators can generate a large amount of undesired harmonic distortion within the power system. These harmonics can cause complications for other systems within the power system and create inefficiencies. There are some standards in place that outline what percentage of transient loading is acceptable for a generation source, as well as what level of harmonics are acceptable, further specified based on harmonic order. These standards provide an important guideline and figure of merit for the operation of a power system, specifically when subjected to transient loading. Through the use of such standards, strict requirements are placed upon the operation of a power system. Even at the consumer or commercial level, standards like these would result in a good amount of protection and a solid foundation at which the power system should operate.

In order to compensate for the lack of capability in traditional microgrid generation systems, the power system can be augmented with energy storage elements. This energy storage can be used to provide power to the transiently operated systems in the islanded system. This benefit extends deeper, however. Whenever the transient event is over, the energy storage can be used to baseload the generation system while it is recharging. Therefore, the generation source operates as if it is continuously base loaded, while the energy storage is able to provide instantaneous energy for transient, high demand loads. This is the operating principle for a hybrid energy storage module (HESM), which integrates this ideology with multiple, controlled energy storage

elements to create a versatile and efficient power system topology. Previous work has been done by Cohen on a HESM-based system.

Energy storage for use in this application can come in a variety of different forms. There are many different kinds of electrochemical energy storage commonly available on the market today. A few examples of this are thermal batteries, lithium-ion batteries, ultracapacitors, and lithium-ion capacitors. For batteries, each type of chemistry has advantages and disadvantages. For instance, lithium metal batteries have the highest combined power and energy density of the common chemistries, but they are primary cells, meaning that they can only be used once and cannot be recharged. This, combined with the high cost of these types of batteries, makes them undesirable for the application presented here. Lithium-ion batteries (LIBs) are the next most power and energy dense of the chemistries. The blanket term 'lithium-ion' covers a broad spectrum of different chemical compositions and combinations. In general, lithium-ion batteries are rechargeable; however they do have some lifetime concerns. Over the course of their use in an islanded power system, things like capacity fade and discharge/recharge cycles must be considered. Other alternatives are lithium-ion capacitors and ultracapacitors. While not as energy dense as their battery counterparts, lithium-ion capacitors are capable of sourcing large amounts of instantaneous power. Like batteries, lithium-ion capacitors may suffer from similar lifetime duration issues, and have the same environmental limitations. Ultracapacitors are at the far end of the power density spectrum, but suffer due to lack of raw energy storage. The nature of their operation makes them the most viable for high power, low energy applications, though they are often larger than primary or secondary lithium-ion cells. This is a complication for microgrid applications, where there is often limited physical space for energy storage on the remote platform.

1.2 Typical Modern System Configurations and Loads

There has been emphasis lately on the usage of nodal designs in microgrid power system architecture. This is very well portrayed in the work of Norbert Doerry. Layout of microgrid systems in this manner offers a variety of advantages, mainly concerning survivability when subjected to extreme transient loading or if a portion of the microgrid power system is damaged. The methodology behind a nodal design is that a given power system has multiple different regions that contain local generation and load sources, each interconnected with a small number of links. If one region is damaged, it can be constrained or removed from the system through the control or removal of these links between regions. The result of this is a large increase in overall power system reliability, at the potential cost of a smaller region's operation in fault conditions. This method for power system design is popular in systems like microgrids because they typically do not have a small number of massive generation sources like a typical power grid style system would. Instead, microgrids often have many smaller generation sources that are mainly intended to service the local requirements only under typical operation. In conjunction with localized, smaller-scale generation, it is common to place energy storage elements within a microgrid system for system reliability and robustness. These energy storage elements can vary, but are commonly a form of battery storage. A modern and common choice for battery storage systems is the usage of lithium-ion cells.

1.3 Types of Lithium-Ion Cell Chemistries and Parameters

There are many different types of lithium ion cells that are commercially available, with a large number of different chemistries and form factors on the market. A lithium ion cell is constituted by, typically speaking, a graphite anode, a cathode

that is made up of the lithium chemistry of the cell, a membranous separator between the two electrodes, and a liquid electrolyte medium. The purpose of the separator is to electrically isolate the two electrodes from one another, while still facilitating the migration of ionic lithium from one electrode to the other during a charge or discharge process. These lithium ions carry with them the positive ions that are necessary for the source or sink of charge from the cell. Essentially, the separator is insulative electrically, but not ionically. The electrolyte medium is what is responsible for carrying the lithium ion across the separation boundaries between the two electrodes.

This collection of separators and electrodes can be assembled in a variety of physical layouts. The two most common ways to create a lithium ion cell is through the usage of strips of electrodes and separators folded up in a serpentine pattern, resulting in a stacked up formation that can be wrapped in a flexible or stiff outer covering. This is what is known as a prismatic cell. The other common way of assembling a lithium ion cell is through the usage of a long strip of electrodes and separators, which is rolled around a central core. This roll is then placed into an aluminum cylinder of desired height and diameter. This type of cell is referred to as a cylindrical cell, and is most commonly available in two different sizes at this time - either 18650 or 26650 format. This means that the cell has a cylindrical height of 65 mm for either format, and a diameter of 18 mm or 26 mm, respectively. Cells are not limited to these smaller sizes, however. More modern lithium ion batteries are being designed and manufactured in larger physical packaging, allowing for higher rate operation and increased capacity over the smaller conventional sizes. These are typically known as large-format lithium ion cells. These types of cells are of particular interest for application in microgrid systems due to their ability to provide system-level power while minimizing total cell count requirements.

Lithium ion cells have a few parameters that must be outlined for general usage in an electrical system. These are shown here.

Maximum Voltage (V) - This is the maximum voltage that the cell can be charged to or operated at without damaging the cell or degrading its capability to store charge. Exceeding this parameter can potentially result in permanent damage to the cell or catastrophic cell failure. This parameter depends on the cell chemistry.

Minimum Voltage (V) - This is the minimum voltage that the cell can be discharged to or operated at without damaging the cell or degrading its capability to store charge. Exceeding this parameter can potentially result in permanent damage to the cell or inhibit the cell's ability to accept charge. This parameter depends on the cell chemistry.

Capacity (Ah) - This is the rated energy storage capacity of the cell. While typically expressed in amp-hours (Ah), this parameter is another way of expressing charge, and is equivalent to 3600 coulombs. This parameter is typically used to define the maximum operating charge and discharge rates for the cell by dividing those amperage values by this parameter, resulting in 'C-rate'. This parameter will degrade after repeated cycling of the cell, or if the cell is abused through exceeding other parametrical values. Temperature can have an effect on the usable capacity of the cell, and prolonged exposure to extreme temperatures can permanently decrease a cell's capacity.

C-Rate - This value describes the rate of charge or discharge of a cell by normalizing the amperage to the nominal capacity of the cell. This is a useful way to determine the operational time capability of the cell given a constant C-Rate load. It is also a way of estimating the amount of stress placed on the cell at the given rate.

Effective Series Resistance (ESR, Ω) - This parameter is the internal resistance of the cell that is expressed during conduction. There is a variety of ways to measure this parameter. ESR varies widely based on factors such as physical construction, cell chemistry, cell age, etc. This parameter increases as the cell is aged through cycling or temperature exposure.

CHAPTER 2

1000 VDC LITHIUM ION BATTERY

2.1 Overview

Lithium ion batteries are becoming more widely considered for use as prime power supplies in high power systems, especially when they contain transient electrical load demands. To meet the power and energy requirements of these unique applications, large quantities of cells must be configured in a combination of series and parallel connections. Given potential safety concerns that come with operating a high voltage battery at high power rates, advanced protection schemes are required to monitor the large number of cells and notify the overarching control system of imminent problems. Batteries are operating at potentials as high as 1000 VDC. Evaluation of batteries at this voltage level has not been widely documented due to the limited applications requiring voltages this high. In the work discussed here, a 1000 VDC battery has been developed, utilizing a commercially available lithium-iron phosphate (LFP) chemistry, and studied at power levels as high as 250 kW. Two unique sensor systems have been installed on the battery. One is a Luna Innovations Inc. fiber optic temperature sensing (FOS) system and the other is a Nexceris LLC. electrolyte leak detection system. Each of these already commercial off the shelf (COTS) available monitoring systems have been previously demonstrated in similar applications independently but this is the first time both have been used simultaneously on a battery like the one being discussed here. The design of the battery, each of the respective sensor systems, and the results collected to date will be discussed.

Many future electrical loads deployed in islanded DC microgrid systems may operate in a transient manner at high DC potential. Some may operate directly from a DC power source while others could rely on some sort of intermediate energy storage system that initially draws energy from either an AC or DC power source. The operational voltages of these loads may range anywhere from a few hundred volts up to hundreds of thousands of volts, making it impossible to implement a one-size fits all power supply. AC/DC and DC/DC power converters will be required throughout the power system to meet each unique load's power requirement. Given these constraints, one possible solution that has emerged involves the utilization of energy storage, possibly lithium-ion batteries (LIBs), assembled with an open circuit potential (OCP) as high as 1 kVDC [1, 2, 3].

LIBs have not been widely studied with OCPs as high as 1 kVDC due to a lack of commercial applications relying upon voltages this high. It does appear that there may be some slow growing interest in utilizing DC potentials as high as 1 kVDC in industrial solar applications, though the literature in this area is limited [4, 5, 6, 7]. Therefore, research is needed to understand the challenges facing the design, reliability, and safe operation of batteries built at these high potentials.

To that end, the University of Texas at Arlington (UTA) has constructed two 1 kVDC batteries – one assembled using valve regulated lead-acid (VRLA) modules and one comprised of lithium ion cells/modules. The VRLA battery was designed, constructed, and experimentally evaluated first due to its safer and better understood chemistry [8]. Using lessons learned from that development, a 30 Ah lithium-ion battery has been designed, constructed, and experimentally evaluated. It has been built utilizing a novel cooling architecture, a novel thermal sensing diagnostic [9, 10, 11], and a novel electrolyte off-gassing sensor system [12, 13]. The details of the battery and each of these critical system components will be discussed in detail here.

The battery built on-site has been constructed utilizing lithium-iron-phosphate (LFP) lithium-ion cells. As already implied, the battery is designed using novel cooling, thermal sensing, and safety diagnostics. An overall system architecture diagram is provided in Figure 2.19.

2.2 Cell-Level Characterization and Lifetime Testing

Before construction of the 1 kVDC lithium-iron-phosphate battery consisting of Saft VL30AFe cells was initialized, the LIB cells were subjected to thorough evaluations. These evaluations consisted of high rate charge and discharge operation, testing at various temperatures, and lifetime testing of the cells when operating at elevated charge and discharge rates. This testing was set up to thoroughly evaluate the cells and determine the viability of their use in a full scale battery system. The testing performed on the individual cells is outlined here.

For the individual cell testing, a single cell was observed. The cell observed is a production cell from Saft, made to their specifications. This cell was evaluated to see if a there would be any meaningful operational degradation and aging over the duration of the high rate, transient load profiles that the final battery assembly would be subjected to.

Tables 2.1 and 2.2 represent measured metrics. All cutoff values, including temperature and voltage limits, were provided from the original manufacturer's (Saft) datasheet suggested values, with the exception of the maximum continuous discharge rate used. These limits, and other characteristics, are shown here.

All testing and evaluations of the cell of interest has been performed personally within the lab. Figure 2.19 shows an example of the test setup, with the cell under investigation placed in a temperature-regulated chamber held at 20°C. Note that two cells are shown, as inital baseline characterization was performed on two cells to show

Table 2.1: Saft VL30AFe Electrical Characteristics

Charateristic	**Rating**
Typical Capacity (C/5 Rate)	32 Ah
Minimum Capacity (C/5 Rate)	30 Ah
Nominal Voltage	3.3 V
Energy	99 Wh
Maximum Continuous Discharge Current	300 A
Maximum Pulsed Discharge Current (2 seconds)	500 A
Typical Continuous Power (100% SOC)	882 W
Typical Pulsed Power (2 seconds, 100% SOC)	1600 W
Maximum Impedance (25°C, 50% SOC, 8C 30 second pulse)	1.5 mΩ
Typical Impedance (25°C, 50% SOC, 8C 30 second pulse)	1.2 mΩ

Table 2.2: Saft VL30AFe Physical Characteristics

Characteristic	**Value**
Diameter	54 mm
Height (including terminals)	222 mm
Mass	1.06 kg
Volume	0.508 L

any variances that might be expected between cells. Ambient cooling is only utilized for baseline characterization of the cells. During lifetime cycle testing, the cell is placed within a water-cooled aluminum block, with coolant held at a temperature of 20°C and flow rate of 5 liters per minute (LPM).

The high-rate, transient profiles used are given with the notation of an 'on time' during which a DC programmable load is discharging the cell, and an 'off time' in which no charge or discharge is taking place. An example of this is '30-on / 5-off,' meaning a 30 second discharge pulse at a constant current value, followed by a 5 second rest period. After the rest period, the profile is repeated until the cell reaches either a maximum temperature cutoff (60°C) or a minimum conduction voltage (2.5V). Note that the cell did not reach the maximum temperature cutoffs

Table 2.3: Saft VL30AFe Cell Operating Conditions

Condition	**Value**
Typical Cut-off Voltage	2.5 V
Charging Method	Constant Current/Constant Voltage
Charging Voltage	$3.8V(\pm 0.04V)$
Recommended Continuous Charge Current	30 A
Maximum Continuous Charge Current	120 A
Operating Temperatures	-40°C to +60°C
Recommended Storage/Transport Temperature	+10°C to +30°C
Allowable Storage/Transport Temperature	-40°C to +70°C

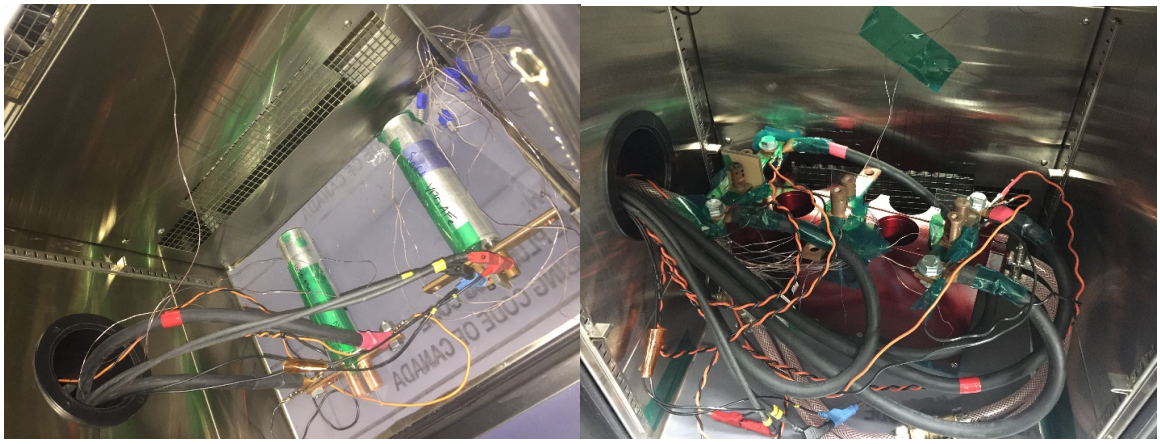

(a) (b)

Figure 2.1: The experimental setup of the VL30AFe cell under investigation. Ambient cooling (left) is used during the baseline procedure, and forced liquid cooling (right) is used during the lifetime cycle testing.

during the testing performed here, so all of the following test profiles were performed until a minimum conduction voltage was observed.

A listing of the 'C-rates' used in the testing is given in Table 2.4. Note that during charge, current is limited to the maximum continuous charge current recommended by Saft in the VL30AFe datasheet (120 A) whenever the equivalent discharge C-rate exceeded this value.

Table 2.4: C-Rate Reference

C-Rate Label	**Discharge Current (A)**	**Charge Current (A)**
0.5C	15	15
1C	30	30
5C	150	120 (4C)
10C	300	120 (4C)
13.33C (Max Rate)	400	120 (4C)

2.2.1 Initial Baseline Characterization Procedure

Before being subjected to the lifetime cycle testing, the Saft production cell was put through a characterization study involving various discharge rates and transient discharge profiles. This has been done to get an understanding of any initial characteristics of the cell performance across a range of requirements, and to offer a snapshot of the initial performance of the cell before the lifetime cycling has commenced. The procedure for this baseline characterization is outlined below. Note that the C-rates are defined in Table 2.4.

Step 1. CC discharges at 0.5C, 1C, 5C, 10C, and 13.33C (max discharge rate from Saft datasheet), until 2.5V is achieved.

Step 2. CC-CV recharge between CC discharges at 0.5C, 1C, 4C (max recharge rate from Saft datasheet), 4C, and 4C, respectively, until 3.8V, then CV charge with C/10 cutoff.

Step 3. Repeat of Step 1 in a 5 second on/1 second off transient discharge profile at variable C rates with CC-CV charge outlined in Step 2.

Step 4. Repeat of Step 1 in a 5 second on/5 second off transient discharge profile at variable C rates with CC-CV charge outlined in Step 2.

Step 5. Repeat of Step 1 in a 30 second on/5 second off transient discharge profile at

variable C rates with CC-CV charge outlined in Step 2.

The results of this initial baseline are summarized below. A more comprehensive summary covering the full evaluation of the performance of the cell during this baseline characterization is shown later in this chapter.

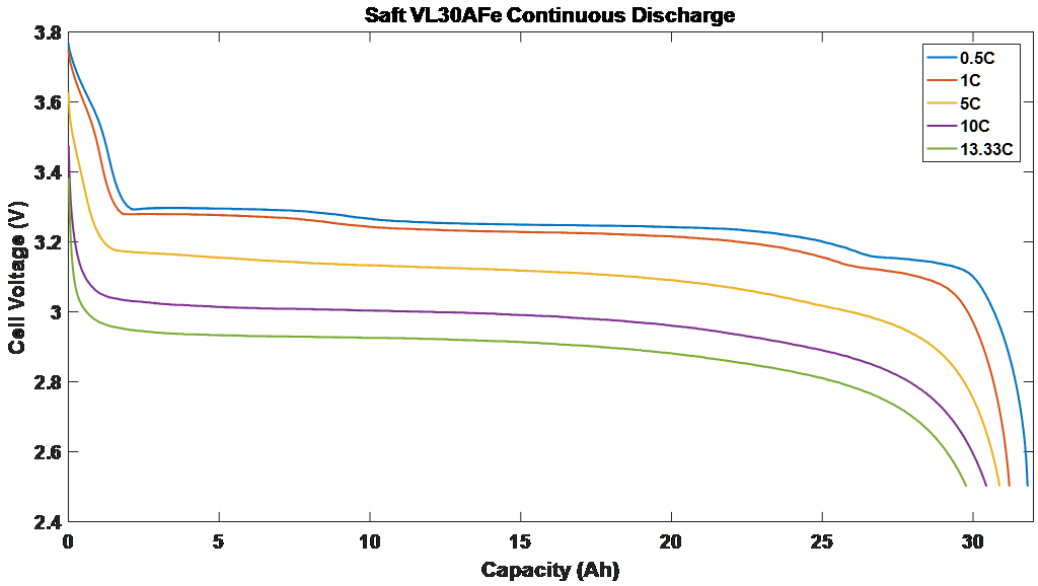

Figure 2.2: Experimental data of the cell performance at various continuous constant current discharge rates.

The following plot shows the calculated ESR of the cell as a function of the depth of discharge of the battery. This was accomplished by taking the voltage drop between the 0.5C and higher rate discharges and dividing it by the difference in current drawn from the cell. This is shown in Equation 2.1.

$$ESR(Ah, C) = \frac{(V_{0.5C}(Ah) - V_C(Ah))}{(30C - 15)} \tag{2.1}$$

where

$ESR(AH)$ is the estimated DC ESR of the cell at the desired capacity (Ω)

Ah is the desired amount of removed capacity from a full charge (Ah)

$V_{0.5C}(Ah)$ is the cell conduction voltage at the desired capacity at a rate of 0.5C (V)

C is the desired C-rate for comparison against 0.5C (A)

$V_{0.5C}(Ah)$ is the cell conduction voltage at the desired capacity at the comparison rate C (V)

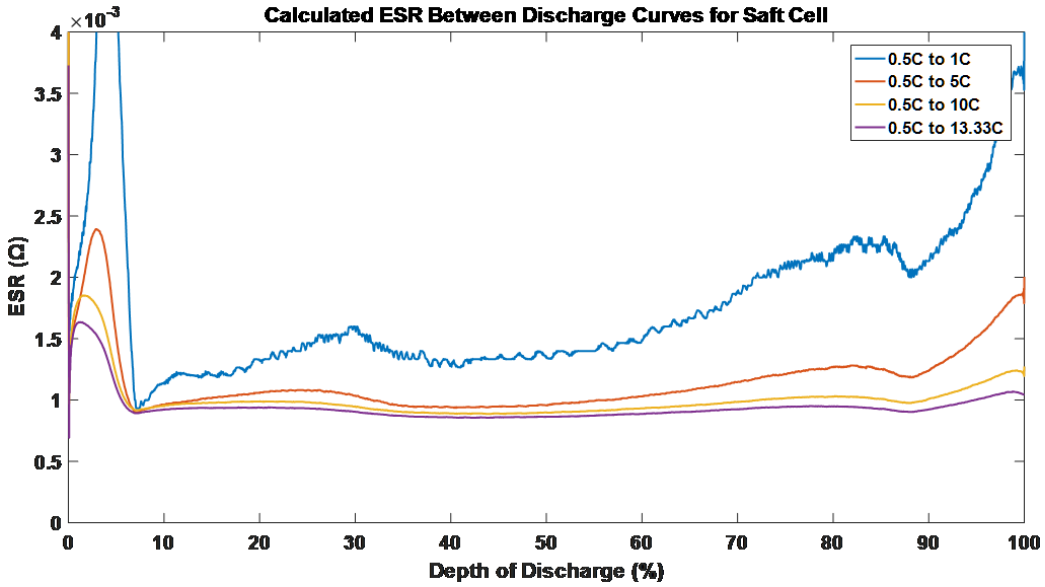

Figure 2.3: Calculated DC ESR for the cell, derived from the constant current baselines shown previously.

This DC ESR calculation is performed by comparing the voltage curve observed at 0.5C, and comparing it to the cell voltage curve observed at other higher rates of continuous current discharge. While it is not a very effective calculation at the endpoints of capacity where large changes in voltage are seen, it is a useful measure in between approximately 10% and 90% SOC of the cell. This is represented by the largely uniform region in the curves between the two points. Disregarding

the observed difference between 0.5C and 1C, the cell's ESR calculations across the various rates are relatively uniform in the middle SOC window, and are roughly the same between baseline rates, at approximately 1 mΩ. The large variation seen when comparing the 0.5C and 1C rates is due to measurement noise and the low level of difference between conduction voltages at an amperage differential of 15 A across the 1 mΩ ESR.

This baseline characterization procedure is performed again after the completion of the 1000 cycle lifetime testing, to determine how the cell has aged, and how the performance of this cell has been impacted by the large amount of high rate cycles that have been performed. The results of this characterization will be discussed after the lifetime testing.

2.2.2 Lifetime Cycling Evaluation - Cycles 1 to 1000

The VL30AFe cell has been evaluated for performance and aging characteristics when subjected to high rate, repetitive, transient load testing. Results of the different facets of performance metrics of this cell is presented here, with data obtained after completing 1000 charge/discharge cycles on the cell.

The cell has been cycled under the following high rate procedure:

1. 10 cycles at 5 seconds on/ 5 seconds off at 1.1 kW CP until V = 2.5V
2. Recharge between each cycle is at 4C – CC until V = 3.8 V
3. Last recharge is at 4C – CC/CV until V = 3.8 V and I = 0.3 A
4. 10 cycles at 5 seconds on/ 1 second off at 1.1 kW CP until V = 2.5V
5. Recharge between each cycle is at 4C – CC until V = 3.8 V
6. Last recharge is at 4C – CC/CV until V = 3.8 V and I = 0.3 A
7. 10 cycles at 5 seconds on/ 5 seconds off at 1.1 kW CP until V = 2.5V

8. Recharge between each cycle is at 4C – CC until V = 3.8 V
9. Last recharge is at 4C – CC/CV until V = 3.8 V and I = 0.3 A
10. 10 cycles at 30 seconds on/ 5 seconds off at 1.1 kW CP until V = 2.5V
11. Recharge between each cycle is at 4C – CC until V = 3.8 V
12. Last recharge is at 4C – CC/CV until V = 3.8 V and I = 0.3 A
13. 10 cycles at 5 seconds on/ 5 seconds off at 1.1 kW CP until V = 2.5V
14. Recharge between each cycle is at 4C – CC until V = 3.8 V
15. Last recharge is at 4C – CC/CV until V = 3.8 V and I = 0.3 A

Essentially, the cell is cycled at various high transient rates, to give the cell exposure to somewhat representative transient loading at different durations to simulate a characteristic operational scenario. These groups of transient discharges and high rate recharges are broken down into 10 cycle segments, where 10 full discharges are performed at differing transient durations, accompanied by a constant current charge with no constant voltage stage. After the tenth discharge, the cells are then full charged using a traditional constant voltage-constant current charge.

At the completion of every fifty high rate charge/discharge cycles, the cell is evaluated at continuous discharge rates of 0.5C (15A) and 1C (30A) to determine the usable capacity of the cell. The cell's impedance is also measured after every 250 cycles using electrochemical impedance spectroscopy (EIS) across a range of SOCs. That data is presented later.

In order to provide a comprehensive evaluation of the cell, it is thoroughly characterized with the baseline characterization procedure described previously. The results of this initial characterization study is shown in Table 2.5.

Table 2.5: Summary of Baseline Characterization for Saft Cell

Procedure	**Capacity In (Total) (Ah)**	**Capacity Out (Total) (Ah)**	**Energy In (Total) (Wh)**	**Energy Out (Total) (Wh)**	**Energy Lost per Cycle (Wh)**	**Max Charge Temp. (°C)**	**Max Discharge Temp. (°C)**
0.5C Continuous	31.27	31.80	103.99	103.05	0.93	21.86	21.92
0.5C Transient (5s/1s)	31.15	30.92	103.60	100.27	3.33	21.78	21.71
0.5C Transient (5s/5s)	31.21	31.10	103.88	100.99	2.89	21.82	21.60
0.5C Transient (30s/5s)	31.13	31.26	103.55	101.23	2.32	21.81	21.74
1C Continuous	31.19	31.20	104.53	100.21	4.31	24.07	23.72
1C Transient (5s/1s)	31.23	30.82	104.71	99.15	5.56	24.04	23.27
1C Transient (5s/5s)	31.24	30.87	104.75	99.49	5.26	23.99	23.00
1C Transient (30s/5s)	31.24	31.27	104.71	100.58	4.13	23.91	23.30
5C Continuous	31.02	30.88	107.62	95.22	12.39	32.85	35.26
5C Transient (5s/1s)	31.09	30.59	107.86	94.30	13.55	32.78	33.68
5C Transient (5s/5s)	31.17	30.61	108.07	94.70	13.37	32.68	31.06
5C Transient (30s/5s)	31.10	30.98	107.88	95.40	12.49	32.87	33.94
10C Continuous	30.45	30.44	105.77	89.90	15.87	32.99	43.15
10C Transient (5s/1s)	30.64	30.11	106.34	89.15	17.19	33.11	42.39
10C Transient (5s/5s)	30.77	30.25	106.71	89.98	16.72	32.87	39.76
10C Transient (30s/5s)	30.55	30.47	106.07	90.12	15.95	33.05	42.75
13.33C Continuous	29.80	29.77	103.54	85.72	17.82	33.02	47.43
13.33C Transient (5s/1s)	29.89	29.36	103.81	84.81	19.01	32.80	46.05
13.33C Transient (5s/5s)	30.26	29.74	105.02	86.28	18.74	32.79	44.12
13.33C Transient (30s/5s)	29.77	29.66	103.41	85.56	17.85	32.86	46.19

2.2.3 Results from High Rate Lifetime Cycle Testing

After each 50-cycle procedure is performed on the cell, a 0.5C (15A) and 1C (30A) constant current (CC) discharge is performed on the cell, after being charged to maximum state of charge using a constant current-constant voltage (CC-CV) charge profile at 0.5C and 1C to 3.8V, with a C/10 (3A) constant voltage cutoff. During the constant current discharge, the cell is discharged until the minimum voltage level is reached (2.5V). The plots below represent cell voltage versus capacity, as the CC discharge is performed.

With the exception of the initial 50 cycles, the cell has a small, linear decrease in usable capacity as high rate transient discharge cycles are performed. During the discharge, approximately the first 4 Ah have the exact same voltage characteristics, regardless of any total capacity difference. The remainder of the discharge still maintains the same general voltage characteristics as energy is removed from the cell, with a shift based on the capacity loss sustained from the cycling and aging. A large difference in the way that the cell ages is in the voltage characteristics. As mentioned before, the cell maintains almost identical voltage characteristics as capacity fades. Interestingly, the cell loses the largest amount of capacity during the initial 50 cycles, after which the rate of capacity fade remains linear with cycle count.

From the information presented in Figures 2.22, 2.23, and 2.24, the percent loss of cell capacity can be expressed. The final amount of capacity loss, after all 1000 cycles have been completed, is shown in the 2.6. Note that this is calculated by comparing the final 0.5C and 1C baseline capacity measurements performed after cycle 1000 with the baseline measurements made after the initial baseline and characterization procedure.

The calculated DC ESR of the cell is largely consistent between the different rates evaluated. To calculate this curve, the difference in voltage levels between

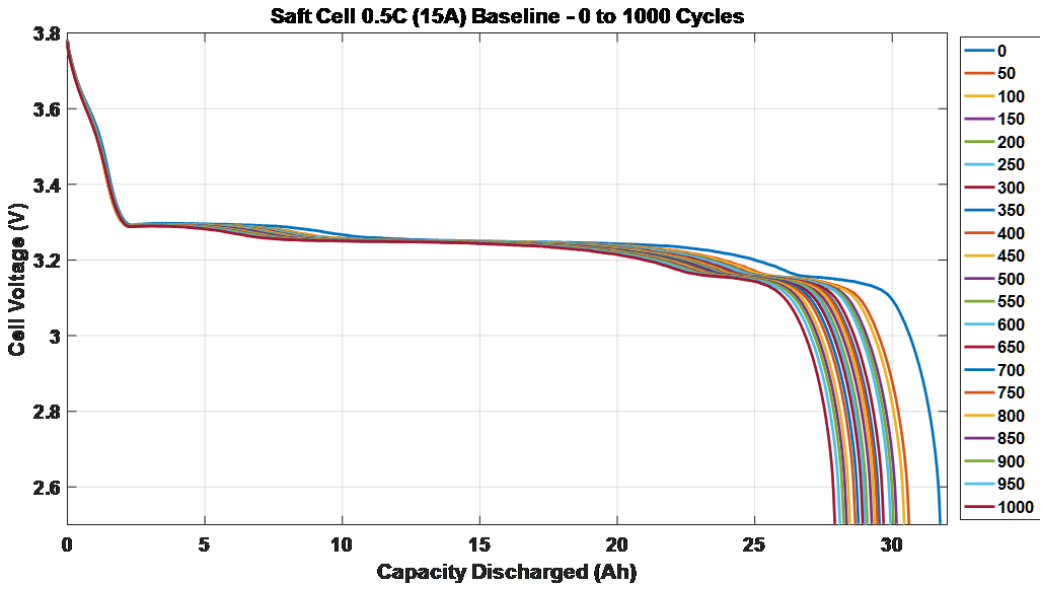

(a)

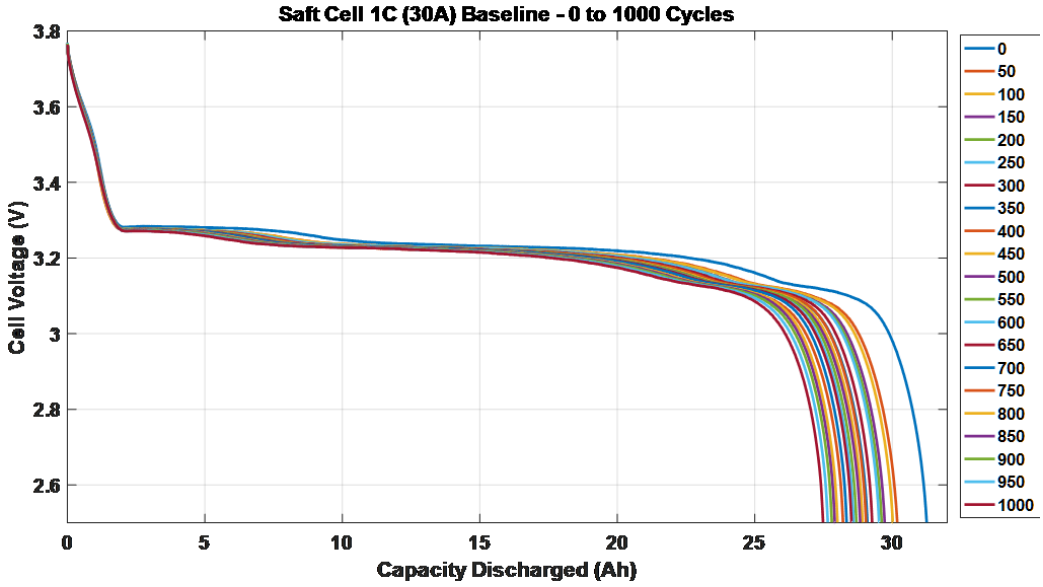

(b)

Figure 2.4: Cell voltage versus the amount of capacity removed from the Saft VL30AFe during 0.5C (15A, (a)) and 1C (30A, (b)) continuous current discharges every 50 cycles during the lifetime cycle testing.

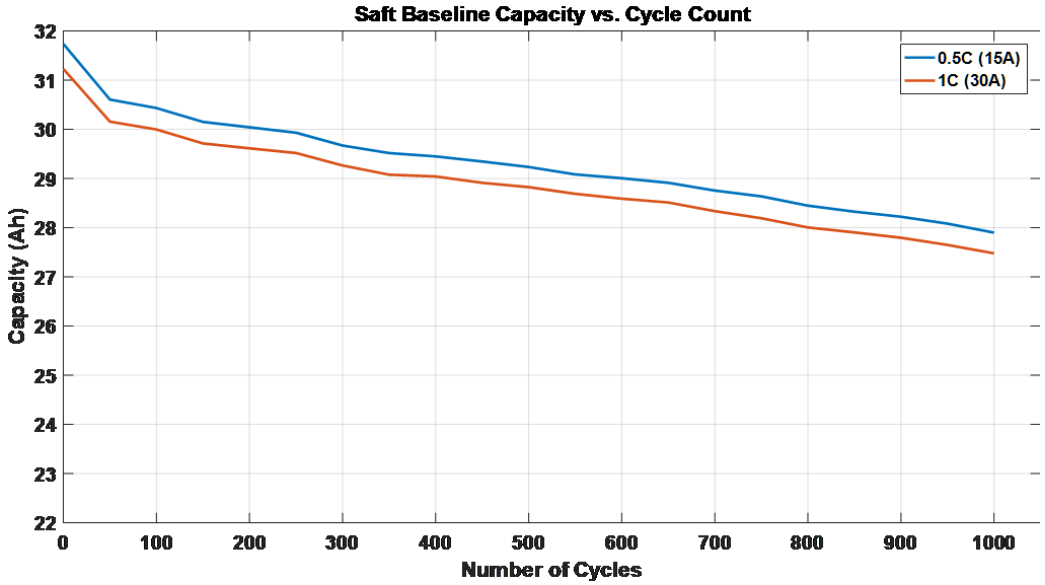

Figure 2.5: The usable capacity measured during the 0.5C and 1C baseline discharges performed every 50 cycles.

Table 2.6: Capacity Fade (% Loss vs. Initial Capacity)

C-Rate	% Difference at Cycle 0 and Cycle 1000
0.5C	12.09
1C	12.01

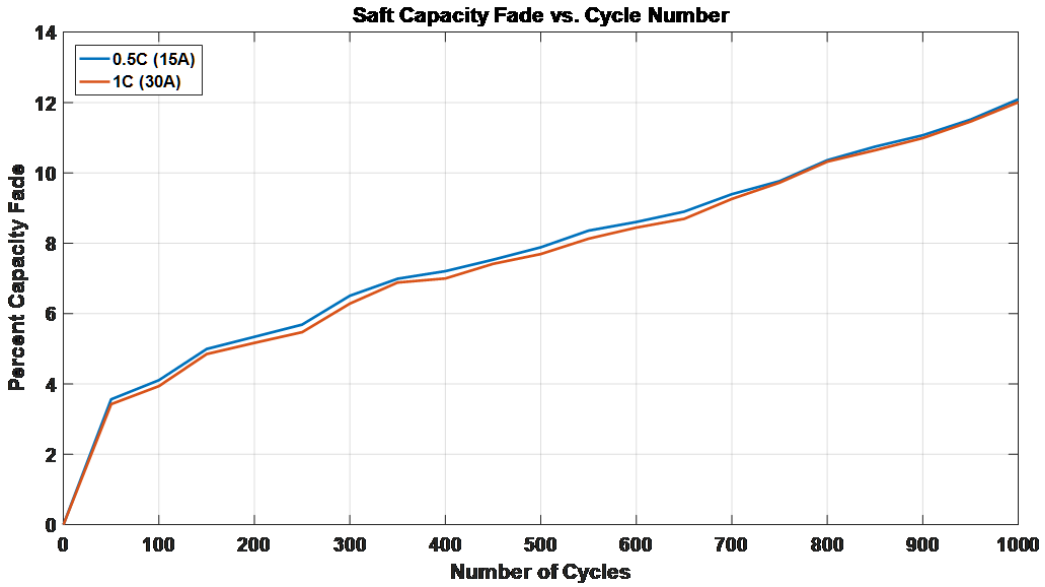

Figure 2.6: The percentage of capacity loss as the lifetime cycling procedure is performed.

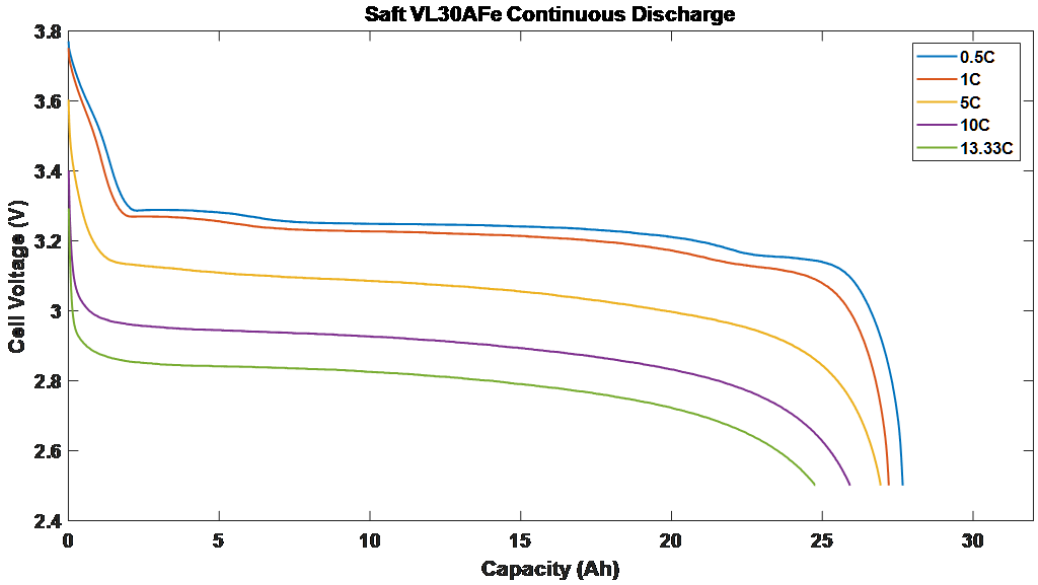

Figure 2.7: Comparison of the discharge curves at various continuous constant current discharge rates after 1000 high rate transient cycles have been performed.

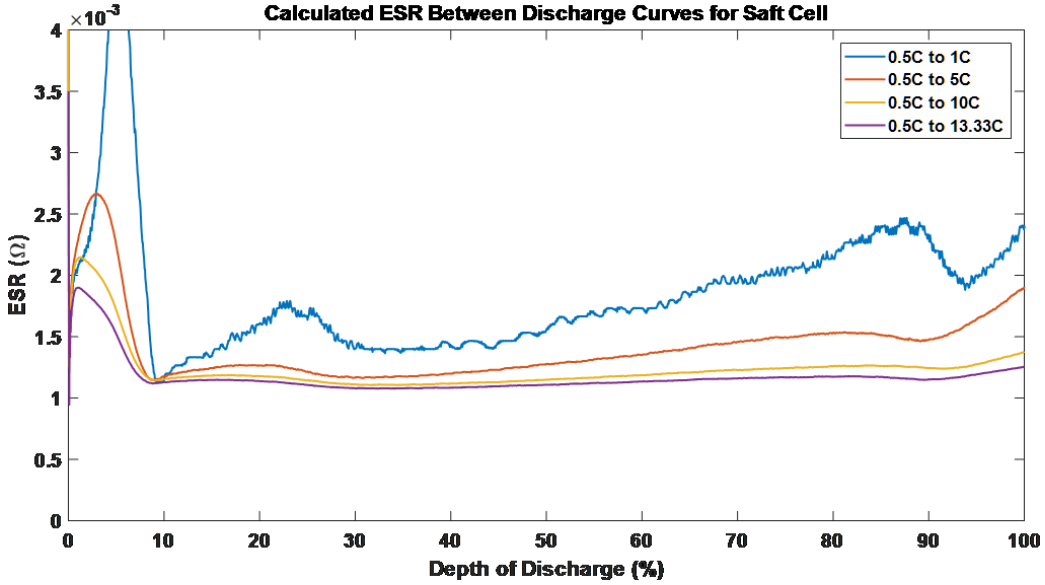

Figure 2.8: Calculated DC ESR for the cells after 1000 cycles, derived from the constant current baselines shown previously.

the 0.5C baseline and another higher rate (shown in the legend) is taken, and then divided by the difference in current between the two baseline curves to provide a measure of internal resistance. It consistent between all of the rates higher than 1C. When compared to the same evaluation performed before the lifetime high rate cycle testing, a DC ESR value of approximately 1.2 mΩ is calculated, which shows an an approximate increase of 200 $\mu\Omega$ due to the high rate lifetime cycling that has been performed.

2.2.4 Electrochemical Impedance Spectroscopy (EIS)

The tested cell is also analyzed through the usage of electrochemical impedance spectroscopy (EIS) at strategic points during the 1000 cycle evaluation. At each of these points, capacity information from the previous 0.5C baselines are used to determine the cell's overall capacity at that point in the cycle life testing. Using this capacity number, the cell is fully charged using a CC-CV charge with C/10 cutoff, like before. Galvanostatic EIS is performed across a logarithmic frequency range from 10kHz to 10mHz, with a sinusoidal current peak of 15A. The cell is then discharged by 10% of the last determined capacity, and the EIS evaluation is repeated, until the EIS procedure is performed at 20%. This is done for the cell at seven different points during the evaluation.

A comparison is shown below for the cell, emphasizing the EIS measurements performed at 50% state-of-charge (SOC) across the range of cycles performed. The impedance measurement Z' is normalized to the point at which the EIS measurements cross over the real axis to account for any shifts and changes in real impedance, so that the characteristics of the internal complex impedance structure can be compared directly. There isn't much notable change in the general shape or vertical scale of the EIS measurements performed on the cell over the cycle life, indicating that there has

not been much internal structural change within the cell. The only notable conclusion to be drawn from the EIS measurements is the increase in cell resistance.

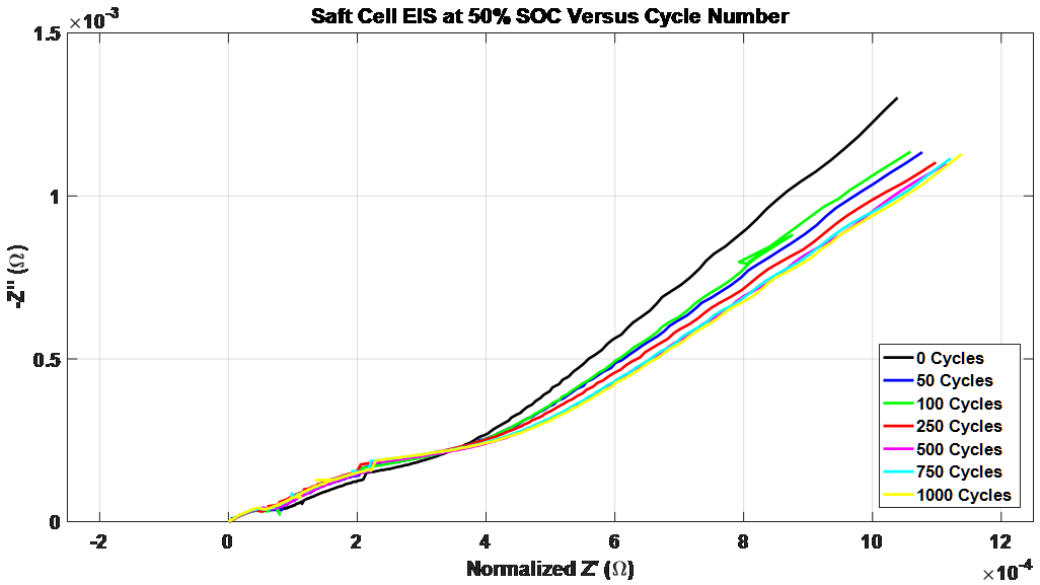

Figure 2.9: Normalized EIS curves for the Saft cell. Real impedance (Z') is normalized to the point at which the real axis is cross to show trends in complex impedance.

In Figure 2.10, plots of the EIS versus SOC can be seen for the cell tested here, before cycling and after the completion of 1000 cycles. The cell exhibits a shift to the right after the cycle testing, representing an increase in the internal resistance of the cell.

2.2.5 Cell Transient Load Performance

Shown here is a comparison of the first and last transient load performance profiles performed at 1.1 kW constant power during the high rate transient discharge life cycle testing. The comparisons below include the very first and very last transient discharge at the 5 second on/5 second off, 5 second on/1 second off, and 30 second

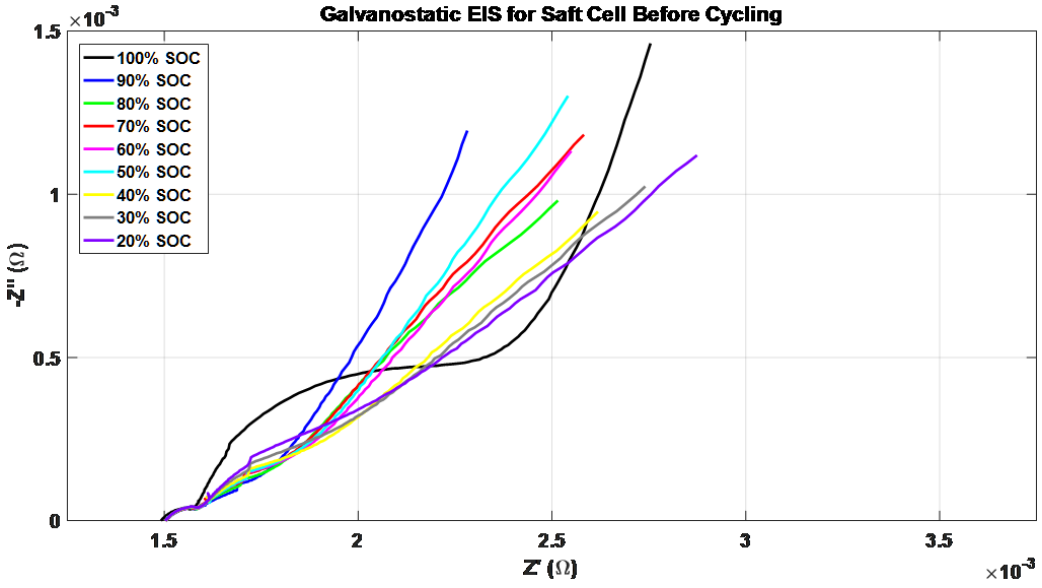

(a)

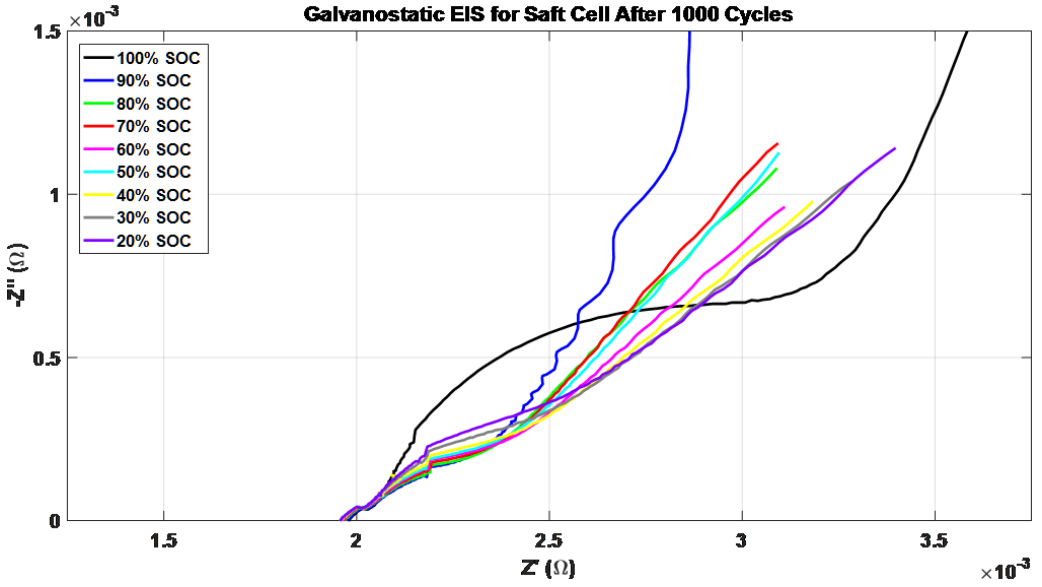

(b)

Figure 2.10: Galvanostatic EIS measurements taken every 10% SOC before (a) and after (b) the 1000 cycle lifetime testing on the cell.

on/5 second off transient profiles. This comparison is made to distinguish the changes internal to the cell and the capabilities of the cell when subjected to large amounts of high rate, transient loading. The main point of comparison here is to see the performance of the cell when practically brand new (after zero cycles) and after it has been aged and subjected to 1000 cycles at high, transient rates.

2.3 Module-Level Evaluation and Viability Study

After the conclusion of the cell-level evaluations and the confirmation of the viability of these particular cells for the intended purpose, a module was constructed to demonstrate the enhancements that could be made to cell performance and lifetime through the implementation of liquid cooling and thermal management. This module, constructed out of aluminum with cooling passages machined in the center, was also constructed to facilitate the assembly of ten singular cells into a larger format battery for the construction of the full-scale battery planned for the final application. These cooling blocks, made by ThermAvant LLC., were constructed with custom machined copper buswork between cells and instrumented with T-type thermocouples for full thermal evaluations. High rate operation was observed, and the findings and analysis will be shown here.

In these experiments, a liquid-cooled aluminum cold block was implemented. This aluminum block was dielectrically coated using a polyimide coating, specifically the Jaro 650 series of coatings, to facilitate the safe placement of 10 cells in series within the module. Detailed photographs of the aluminum cooling block block are shown in Figure 2.12. In these experiments, many T-type thermocouples were placed throughout the module and on the cells and interconnecting buswork to provide a full analysis of the thermal information seen during high rate operation. All cells placed within the module were first wrapped with Mylar heatshrink and then graphite TIM.

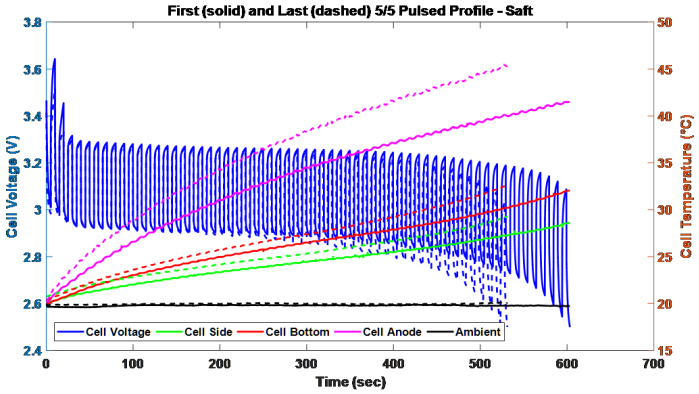

(a)

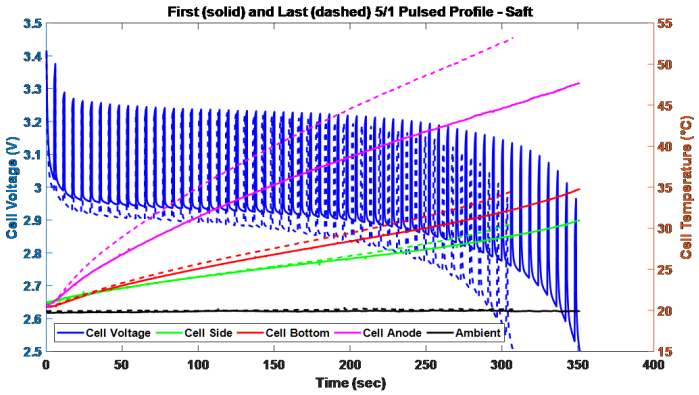

(b)

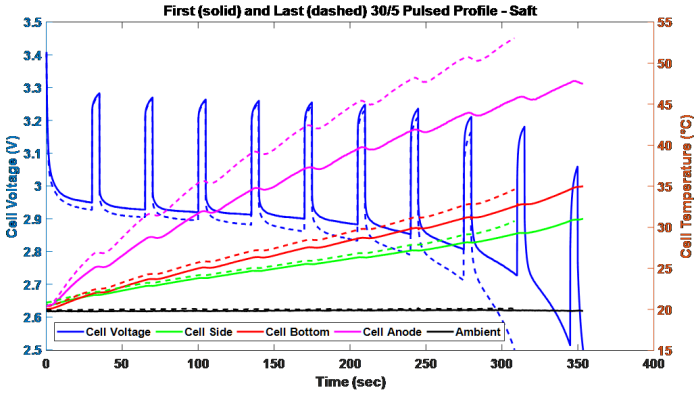

(c)

Figure 2.11: Electrical and thermal data for the first and last transient discharges performed during the 1000 cycle lifetime testing on the cell, shown for all three transient profiles tested.

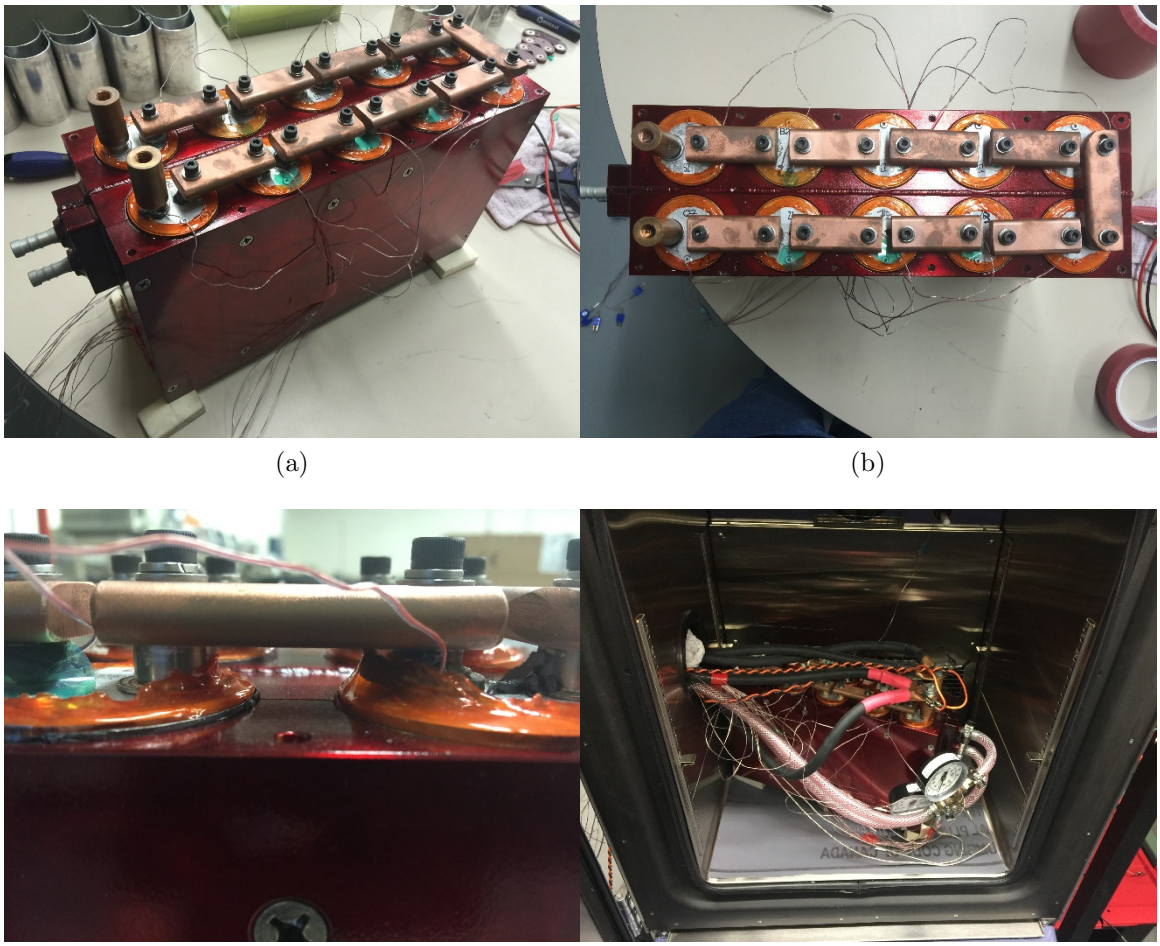

(a) (b)

(c) (d)

Figure 2.12: Photographs of the 10S/1P Saft module constructed inside the liquid cooled, aluminum cold plate. The upper left figure presents the various components of the block, including the aluminum center block and aluminum outer shells. The lower left and upper right photographs show the bus bar arrangement of this module. The lower right photo shows the block ready for testing in the environmental chamber.

Evaluation of the module took place on-site utilizing Chroma 63209, 80V/1000A/15.6kW programmable loads and Ametek SGA 80V / 188A / 15kW programmable power supplies. Custom National Instrument (NI) Virtual Instrument (VI) panels are created to interface with the programmable loads and the programmable power supplies. Thermal data acquisition is performed using NI 9213, 16 channel thermocouple mea-

surement cards. Hall Effect sensors, monitored using NI 9205 data acquisition cards, are utilized for accurate current measurement and capacity calculation. An Espec BTX-433 environmental chamber is used to control the environmental around the module and finally a 5 kW Polyscience recirculating chiller is used to control the water flow and temperature through the center block. Photographs of the experimental setup are shown in Figure 2.13.

The test plan utilized has been defined to illustrate the performance of the module at close to the highest operational rate. One experimental charge/discharge current profile has been utilized. In this profile, the charge and discharge current were each set to 290 A. The procedure is as described below:

1. Soak module in the chamber for a minimum of two hours with 50% water/ 50% polyglycol coolant flowing at 5 LPM
2. Cutoff if any cell sidewall reaches 70°C
3. 1C (30A) CC-CV Charge
4. C/10 (3A) Cutoff
5. 5 Minute Rest
6. 1C (30A) Discharge
7. Cutoff after 6 Ah removed
8. 5 Minute Rest
9. 290 A Repetitive Cycling
10. 5 second charge / 5 second discharge profile
11. Repeat until cell temperatures change less than 1°C/hour
12. Repeat procedure on each module with
13. 20°C water in 20°C environmental chamber
14. 40°C water in 40°C environmental chamber

(a) (b)

(c) (d)

Figure 2.13: Photographs of the Espec BTX-433 environmental chamber (a), thermal data acquisition and control system (b), programmable power supplies and loads (c), and 5 kW chiller (d).

In order to evaluate the effectiveness of the cooling modules in this application, testing is performed with an all-aluminum block that contains 10 cells in series. Custom copper buswork has been machined for the interconnections between cells. The cells were placed within the cooling block with thermocouples on all of the negative cell terminals, cell bottoms (face opposite to terminals), bus bars, and on strategic locations on the outside of the block. Every cell is wrapped in graphite thermal interface material (TIM). This is shown in Figure 2.14. Thermal testing was performed on the module through the usage of high rate, repeated discharges and recharges with fixed ambient and coolant temperatures. This was done by charging the module fully, then removing approximately 20% of the module's capacity to allow for high rate charge and discharge without exceeding the upper and lower voltage limits on the cells. After removing 20% of the module's capacity, it was loaded with a 5 second discharge, followed by a 5 second recharge. This discharge/recharge cycling was repeated for two hours to allow the module to get to thermal equilibrium with the surroundings. Two operational scenarios were evaluated – a charge/discharge rate of 290 A (9.67C) at coolant and ambient temperatures of 20°C and 40°C. Ideally, the usage scenario for the final battery assembly will be with 20°C coolant and close to that (approximately 23-25°C ambient temperature), but the combination of coolant and ambient at 40°C was explored as a representation of a worst-case scenario. All temperature plots are scaled to the same values seen in the previous series to allow for a more direct comparison between the different test cases.

The temperatures measured in this testing of the all-aluminum cooling block are consistent from cell to cell. In other words, the temperatures have very little spread. The highest anode temperature seen in this test is the anode of cell 8, measuring at 38°C. The highest bottom temperature seen in this test is the bottom of cell 8, measuring just over 30°C.

Figure 2.14: Photographs showing the bare cell (left), the cell wrapped in mylar heatshrink (middle), and the mylar wrapped cell covered in graphite thermal interface material (right).

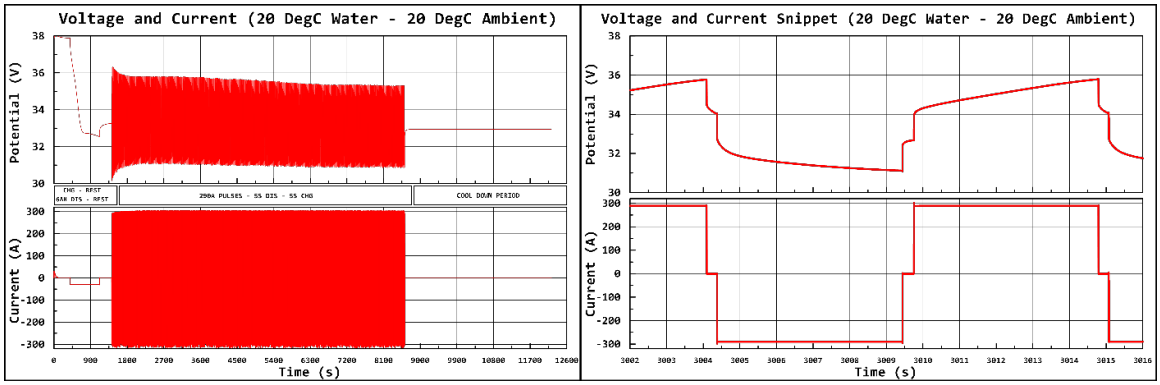

(a) (b)

Figure 2.15: Voltage and current data measured from the 10S/1P Saft VL30AFe module when it was experimentally cycled at 290 A (9.6C) with 20°C water/20°C environmental chamber. The leftmost plot presents an overview of the full experiment while the rightmost plot presents a zoomed in view of a few 5s/5s discharges.

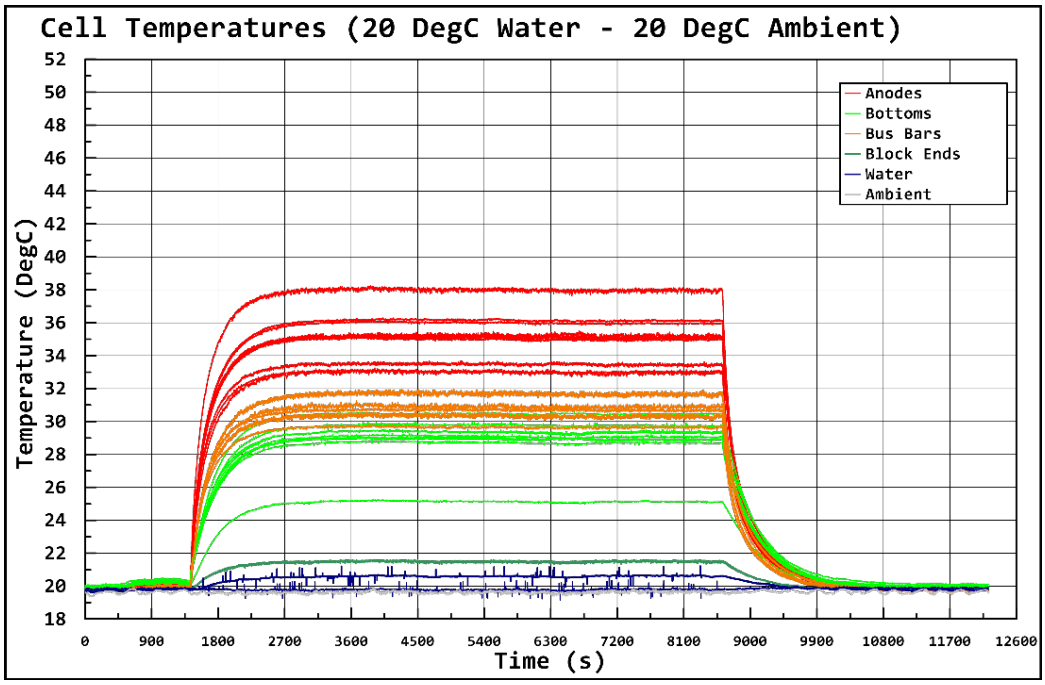

Figure 2.16: Thermal data measured from the 10S/1P Saft VL30AFe module when it was experimentally cycled at 290 A (9.6C) with 20°C water in a 20°C environmental chamber.

After the completion of the 20 degree test, the 40 degree test was performed. As seen in the previous test in this series, the temperatures are consistent between cells. The highest anode temperature seen in this test is the anode of cell 6, measuring at 57°C. The highest bottom temperature seen in this test is the bottom of cell 2, measuring just over 48°C.

The testing performed on the cooling block module has showcased exceptional thermal performance for the cells during sustained high rate operation, and have been suitably vetted for usage in a full-scale battery assembly. Even at this continuous, near-maximum rate of operation for a sustained period of time at elevated coolant and ambient temperatures, no thermal measurement performed exceeded the maximum allowable temperature as put forth in the manufacturer's recommendations. Through

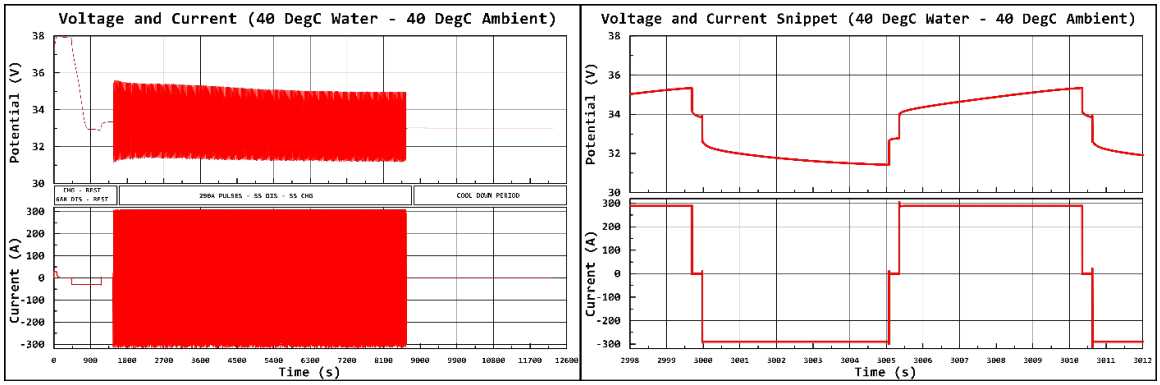

(a) (b)

Figure 2.17: Voltage and current data measured from the 10S/1P Saft VL30AFe module when it was experimentally cycled at 290 A (9.6C) with 40°C water/40°C environmental chamber. The leftmost plot presents an overview of the full experiment while the rightmost plot presents a zoomed in view of a few 5s/5s discharges.

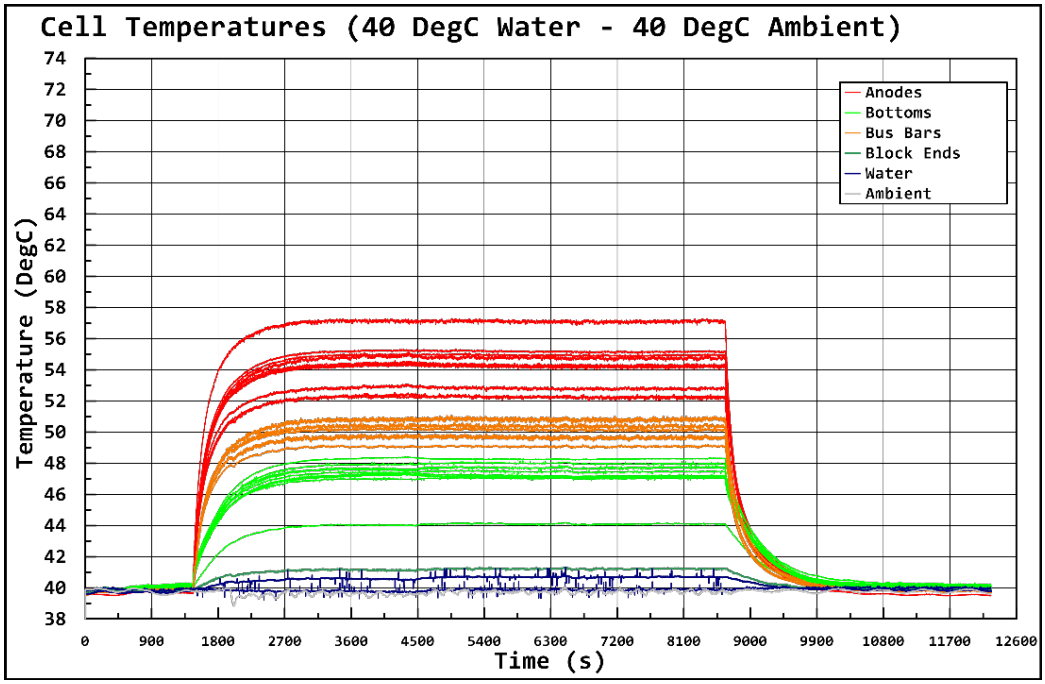

Figure 2.18: Thermal data measured from the 10S/1P Saft VL30AFe module when it was experimentally cycled at 290 A (9.6C) with 40°C water in a 40°C environmental chamber.

the testing performed on the module, it has been shown that this is a safe and viable method of modular construction for a larger-scale assembly.

2.3.1 1 kVDC Lithium-Iron-Phosphate (LFP) Lithium-Ion (LI) Battery

The 1 kVDC LFP-LI battery shares many common assembly features as the 1 kVDC VRLA battery documented previously [14, 15]. It has been assembled through the connection of twenty-eight 10S/1P modules in series. This means that when erected, 280 lithium-ion cells are connected in series to obtain the desired output voltage. The cells utilized are 30 Ah Saft VL30AFe cells that are fabricated using Saft's lithium-iron-phosphate chemistry [16]. UTA has previously presented electrical and thermal data measured at the cell level under both continuous and transient discharge profiles, respectively, across a host of discharge rates as high as 13C (400 A) [17]. Assuming a conduction voltage of roughly 3 V per cell at a 400 A conduction current, the battery is designed to supply roughly 336 kW of power so long as all thermal and voltage limitations are maintained.

Each of the twenty-eight 10S/1P modules are assembled using a liquid-cooled cold block designed and sold by ThermAvant LLC. [18]. A photograph of a single module is presented in Figure 2.20. The cold blocks are fabricated from aluminum that is machined to fit the VL30's cylindrical profile. The center portion of the cold block is fabricated from two welded sections, inside of which is a machined liquid cooling loop. Two outer aluminum clam shells are bolted to the center block to fully encapsulate the cells. A fully assembled module in this cooling block is shown in Figure 2.20. Each block is coated with a polyimide 650 series coating produced by JARO that has a dielectric hold off strength of 3100 V/mil [19]. A 40 kW Polyscience recirculating chiller is used to dissipate the roughly 25 kW of heat generated when the

battery is cycled at 400 A. This heat generation figure is derived assuming roughly 0.5 mΩ per cell as documented from the previous characterizations of the batteries.

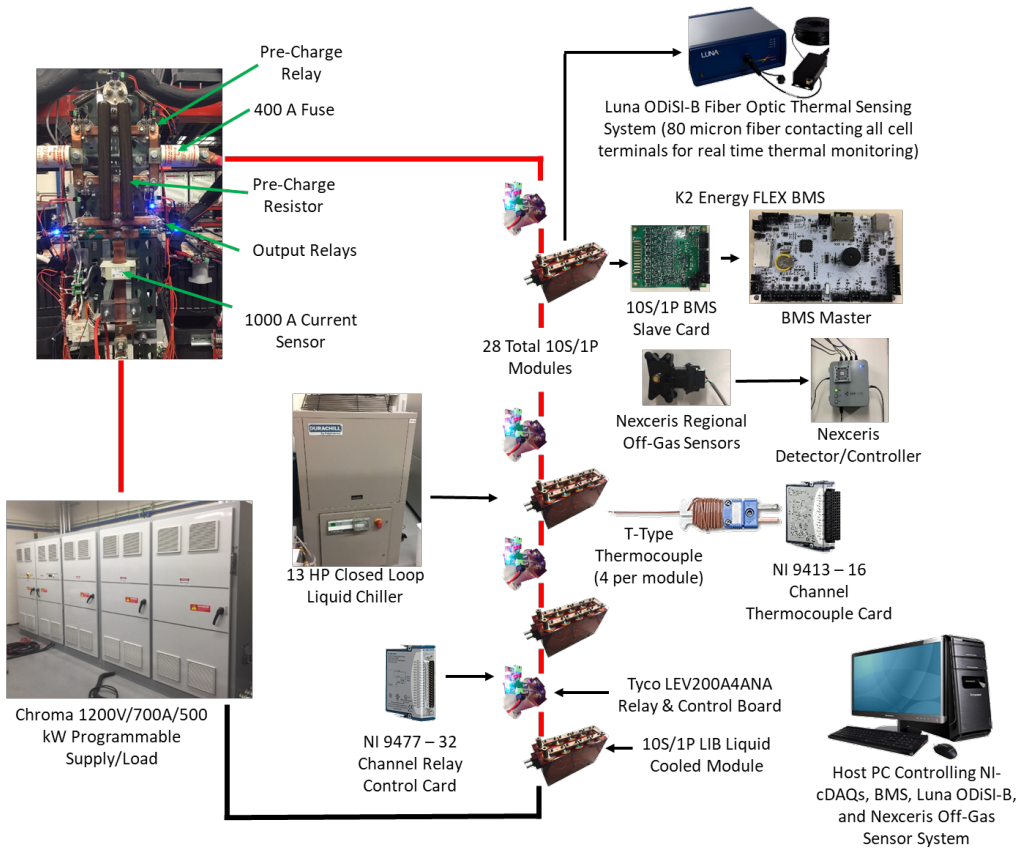

Figure 2.19: Simplified block diagram of UTA's 1000 V lithium-ion battery as it is assembled for evaluation utilizing a Luna ODiSI-B fiber optic thermal sensing system and Nexceris regional electrolyte off-gas sensors.

Each 10S/1P module is electrically isolated from the next using Tyco LEV200A-5NAA mechanical contactor relays. While not erected, each module sits at a safe 33 VDC OCP. During operation, the relays are able to be opened remotely using the control system to isolate modules if an unexpected event were to occur. Each relay is instrumented with a custom designed driver card, seen in Figure 2.21, that visually alerts the user if its input coil is energized by the control system, as well as if the

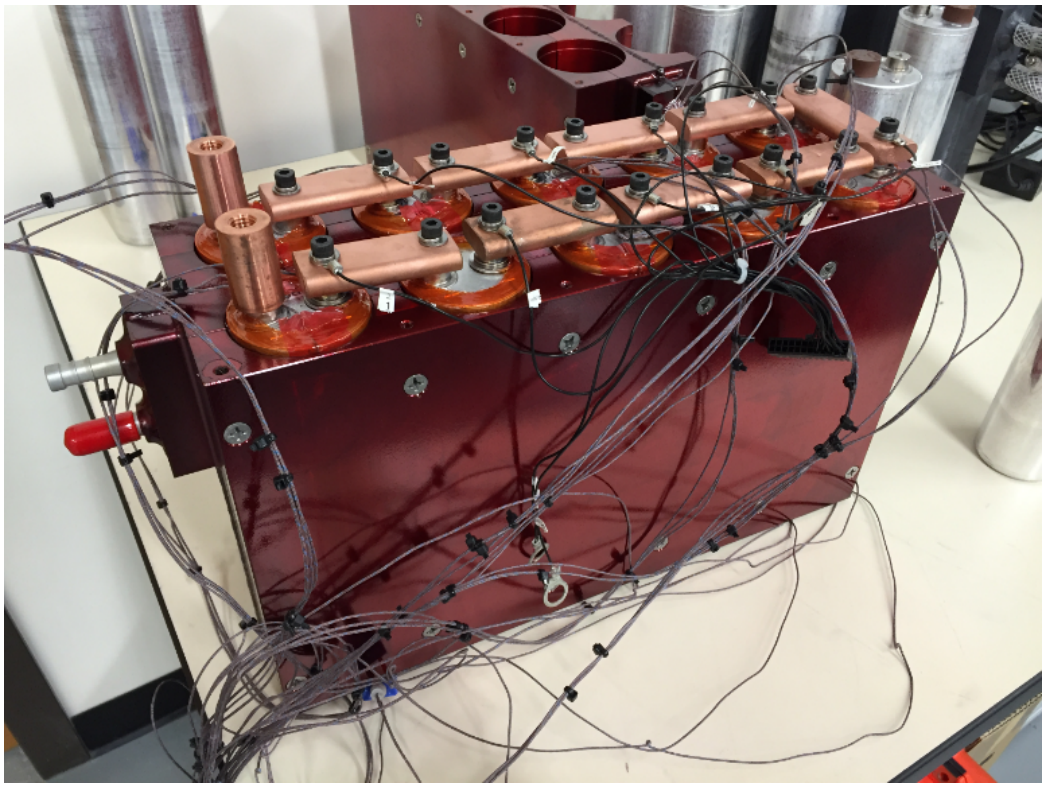

Figure 2.20: Photograph of a single 10S/1P LI module. This particular module was used for thermal evaluation before full scale assembly of the battery, and therefore it has larger number of thermal measurements installed.

main contactor is physically closed, independent of the primary coil's input current [14, 15].

A National Instruments (NI) 9477 solid state relay card, that is installed in a NI CompactDAQ chassis and controlled using a NI virtual instrument (VI) panel, is utilized to connect each relay to a 24 V power source. When 24 V is applied to the primary coil, 5 mA flows through the blue 'Relay CMD' LED, visually indicating that a command to close the relay is present. Once the main contactor is closed, current flows into the base of a transistor, and 5 mA flows through each of the four red 'Relay Active' LEDs causing them to flash, visually indicating that the physical contactor inside of the relay has closed.

Each cell within the battery is monitored and managed using a K2FLEXBMS battery management system (BMS) designed and sold by K2 Energy [20]. The BMS operates like most BMSs do, with active management of cell voltages and protection built in for over-charge and over-discharge of cells. The balancing of the 280 cells is performed with a slave board on each of the twenty-eight 10S/1P modules. The slave boards monitor the local individual cell voltages, and discharge the cells at a fixed current whenever the cell exceeds a value of 3.5 VDC. The cell is discharged until it reaches a value of 3.45 VDC, after which the balance current is stopped. This ensures that all of the cells will ideally settle at a value of 3.45 V, assuming that they are all charged above the 3.5 V balance threshold. The hysteresis band of 50 mV is added to stop the slave boards from oscillating between balance and rest states.

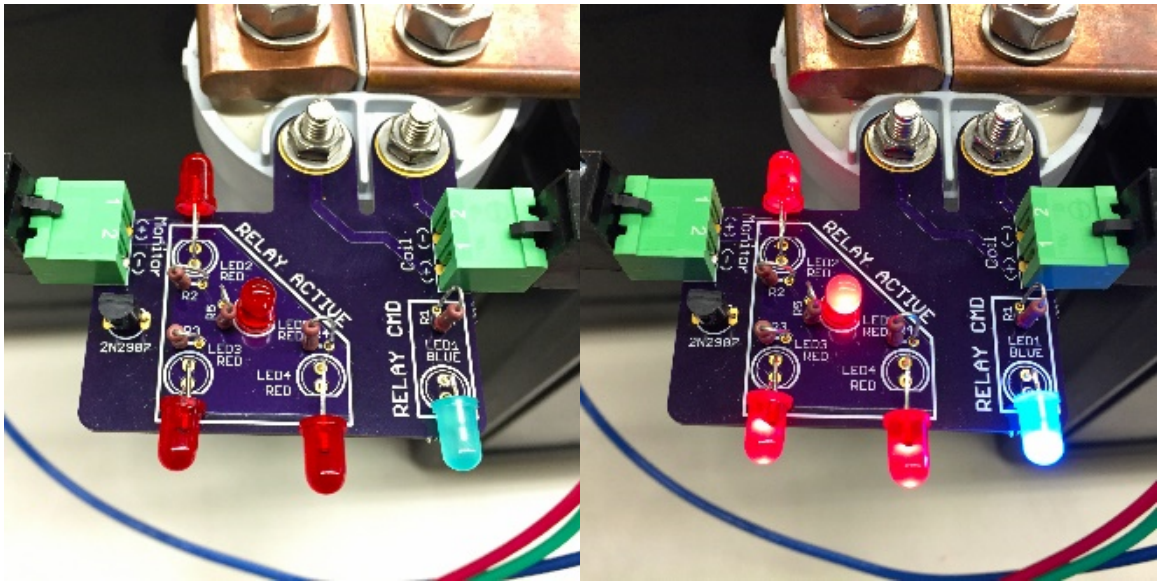

(a) (b)

Figure 2.21: Photograph of the relay visual indicator printed circuit board. The left image shows the PCB when not illuminated and the right image shows the PCB when it is illuminated. Note: Red LEDs flash when relay main contactor is closed.

The BMS master communicates with a host PC using electrically isolated fiber optics and the same host NI VI panel is used to read in and process each individual cells' voltage from the BMS. The VI is programmed to autonomously operate each of the twenty-eight Tyco relays such that it can safely isolate individual modules and open the conduction path of the battery, in the event of any individual cell falling outside of an acceptable voltage range of 2.5 VDC to 3.8 VDC.

In addition to controlling the relays and monitoring/recording cell voltages, the host NI VI also monitors and records thermal data from the 130 T-type thermocouples that are distributed throughout the battery. The thermocouples are all monitored in real time using NI 9213 thermal sensing cards installed in their own dedicated NI CompactDAQ chassis. Initially, it was intended that each of the twenty-eight 10S/1P modules would be instrumented with four thermocouples, three attached on random negative terminals, dielectrically isolated using thermal epoxy, and one positioned down the axial length of a random cell such that a cell's center body temperature is recorded. Though a great deal of care was taken to protect the thermocouples during installation, once assembled, several were found to be electrically contacting their respective negative terminal and several others were found to have been pinched and broken by the cooling block, despite clearances being uniquely placed, causing them to become open circuits. The high number of thermocouples introduces a large number of wires that are difficult to manage and, even with careful management, can be visually unappealing. Though some of these challenges can be easily overcome with additional care and better engineering practices, this highlights the challenges introduced with high thermocouple count and these challenges should be considered later when a novel thermal sensing system is discussed.

Figure 2.22 presents a photographic image of the assembled 1 kVDC LFP-LI battery. As shown, it is assembled on two standard size plastic pallets that are roughly

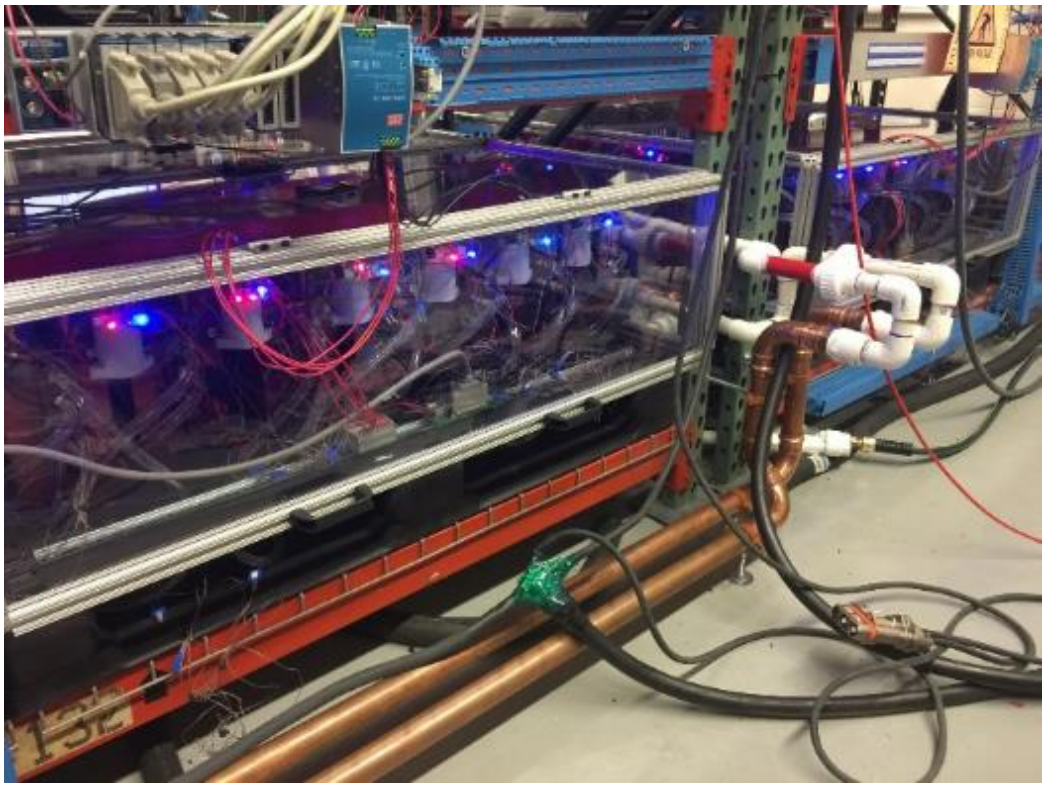

Figure 2.22: Photograph of the 1 kVDC LFP-LI battery during operation as indicated by the illumination of the many respective blue and red relay control board LEDs.

1 m square. Each pallet has fourteen 10S/1P modules installed on it. Each pallet is enclosed by a polycarbonate enclosure 'cap' that is structurally held together using aluminum frames. The 'caps' prevent the battery from being exposed to contact by a user and also contain the novel electrolyte off-gas leak sensors that will be discussed later. 4/0 AWG copper welding cable is used to interconnect the two pallets and also connect the points of highest and lowest potential to the output bus.

The battery's output is fed into a relay-controlled output bus. Using selective relays, it is possible to either connect the battery directly to the load or through a 1000 Ω pre-charge power resistor. A 1000 A hall effect current sensor is installed on the output bus to monitor the battery's output current, which is reported back to the

host VI and utilized as an additional control variable. It should be noted that this output bus is the same one utilized by UTA's two VRLA batteries. When used with the LIB, both VRLA batteries are disconnected from the bus and the LIB replaces one of those batteries as the input. The output bus is shown photographically and schematically in Figure 2.23.

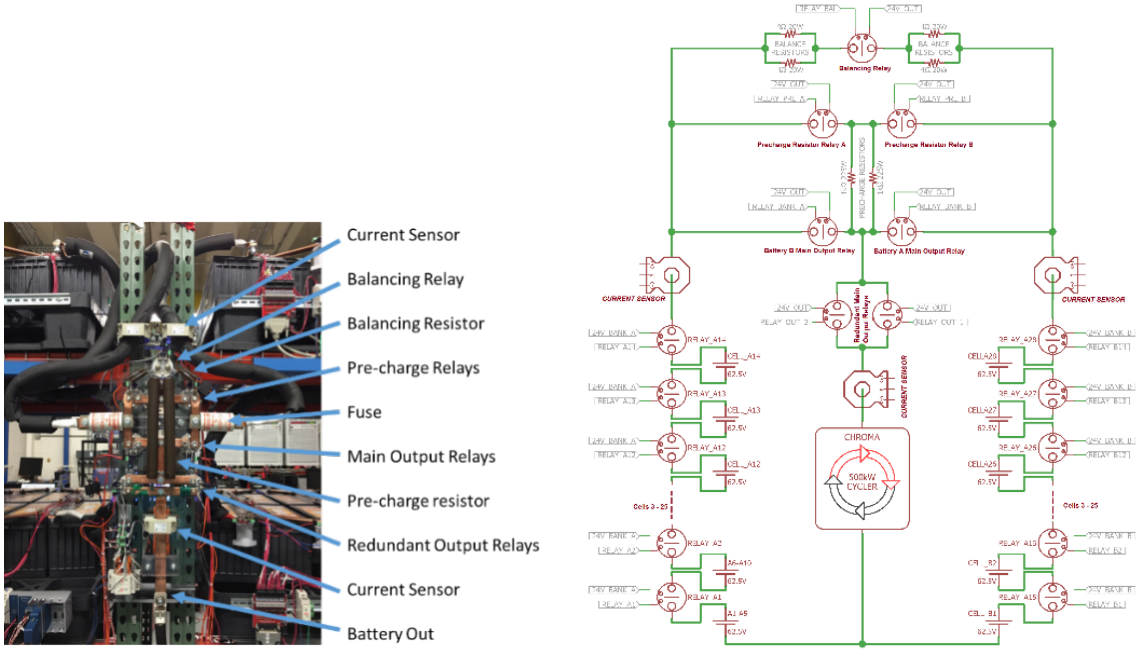

(a) (b)

Figure 2.23: Switched relay output bus, shown photographically (a.) and schematically (b.), capable of connecting either the two UTA 1 kVDC VRLA batteries [14-15], or the one UTA LFP-LI battery through a 1000 Ωresistor prior to directly connection to a load.

2.3.2 Programmable Cycler for 1 KVDC Lithium Ion Battery

In order to load and also recharge the battery, UTA utilizes a Chroma 17030 programmable cycler with ratings of 1200VDC / 700ADC / 500kW. These ratings

mean that the equipment can cycle batteries with potentials as high as 1200 VDC at current rates, both charge and discharge, as high as 700 ADC with a power limit of 500 kW. The 280S/1P LFP - LI battery is only able to supply roughly 330 kW at 400 ADC, well within the limitations of the Chroma 17030. The cycler is controlled using Chroma's proprietary control system that enables it to operate in constant current (CC), constant voltage (CV), constant resistance (CR), and constant power (CP) modes of operation. The system has a slew rate of roughly 10 ms from idle operation to either full charge or full discharge modes. The system is regenerative, meaning that during discharge, the energy extracted from the battery is inverted and placed back on the 480 V - 3Ø utility grid. A photograph of the cycler is shown in Figure 2.24.

Figure 2.24: Photograph of UTA's 1200V/700A/500kW Chroma 17030 battery cycler.

2.4 Novel Measurement and Monitoring Systems

2.4.1 LUNA Fiber Interrogation System

C. Luna ODiSI-B Fiber Optic Temperature Sensing System

A Luna Optical Distributed Sensor Interrogator (ODiSI-B) [9, 10, 11], shown in Figure 2.25, is a single channel data acquisition system that is able to simultaneously measure the temperature and strain at discrete locations down the length of a very thin (165 micron diameter) fiber optic sensor. The ODiSI-B weighs 13.1 kg and has a volumetric footprint of 0.017 cubic meters, not including the PC required to manage the system. The fiber optic sensor that pairs with the system is manufactured using standard off-the-shelf optical telecommunications fiber and consists of a fused silica core, cladding, and a protective polyimide coating. With its ability to provide high spatial density temperature measurement with points spaced every millimeter or so along a continuous sensor, the primary advantage of the ODiSI-B is its ability to replace tens of thousands of thermocouples. This reduces the complexity and challenges that thermocouples introduce, some of which were already highlighted earlier. Due to its small form factor, the fiber optic sensor can in most cases be easily situated within the test setup. Additionally, its non-conductive silica composition ensures that the sensor is well-suited for high voltage applications such as this one.

The fiber optic sensor length ranges from 1 m to 20 m, while the interrogator's sample rate ranges from 50 Hz to 250 Hz. The sensors' thermal resolution is less than 0.1°C with discrete gage spacings of either 0.65 mm or 2.5 mm. At the maximum spatial resolution, this translates to 1563 measurement points along a 1 m sensor. While this prospect is easily managed with a single fiber optic sensor, this is in stark contrast with single point thermocouples, where this measurement density is simply not possible, considering the logistical complexity and associated cost.

The ODiSI-B's measurement method employs the use of optical frequency domain reflectometry (OFDR) technology to measure the spectrum (amplitude and phase) of the Rayleigh backscatter profile of the optical fiber sensor. This scatter spectrum is random but unique to each length of optical fiber, and its frequency content shifts with temperature change and strain. Therefore, the temperature change at each location along an optical sensor is measured by carrying out a cross-correlation of the backscatter spectrum of that location relative to its reference scatter spectrum taken at a known starting condition. The shift of this correlation peak can be converted to the temperature change experienced at that location, through a calibration coefficient. Sensors procured from Luna are delivered with a thumb-drive that contains the appropriate scale factors for the sensor and can be automatically utilized by the software to display the sensor's temperature as part of the graphical interface.

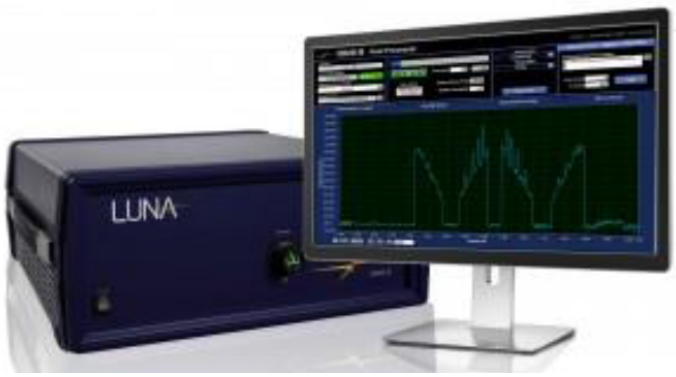

Figure 2.25: Luna ODiSI-B fiber optic interrogation system.

Luna's distributed sensing technology is capable of measuring temperature changes over a range of -268°C to 900°C and strain over a range of $\pm$12000 $\mu\epsilon$. This wide measurement range, combined with small diameter optical fiber sensors, provide a high performance sensing solution. While the main feature of the system being used and discussed here is its ability to measure discrete temperatures, the system is also

able to simultaneously measure strain, something that may also be useful in future battery monitoring applications.

Two 20 m long fiber optic sensors were utilized to measure the entire LFP-LI battery assembly. A single 20 m sensor would have been sufficient but this alternative layout was selected due to the assembly process of the battery pack. The sensors were installed such that the temperature of every single one of the 280 cells' terminals can be measured simultaneously. The fiber was wound in a 'u-shape' serpentine pattern around each module and in a similar 'u-shape' between modules. A few different photographs of the fiber installed on the battery are shown in Figure 2.26, where the outline of the fiber is highlighted in blue in some cases for ease of visual understanding.

The fiber is mechanically held against each terminal by putty that is simply pressed against the terminal with the fiber embedded between the contact surfaces. Unlike thermocouples, the fiber is made of a dielectrically insulated material and therefore contact with the terminal is not of concern, but rather encouraged. It is also worth noting that the fiber has less thermal mass than thermocouples and therefore the response time of the measurement is quicker due to its lesser dependency on thermal mass. Earlier it was mentioned that three type-T thermocouples are randomly placed against negative terminals within each of the twenty-eight 10S/1P modules. The data collected by those thermocouples are being used to validate the data recorded by the ODiSI-B. Thus far, there has been very consistent agreement between the thermocouples and the ODiSI-B, as will be shown later in the experimental results section. However, there are also exceptions as will be shown.

2.4.2 Nexceris Li-Ion Tamer Electrolyte Sensor System

D. Nexceris Li-Ion Tamer® Electrolyte Leak Detection System

(a)

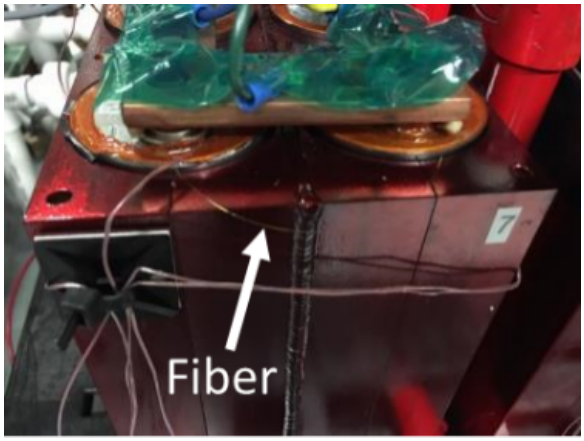

(b)

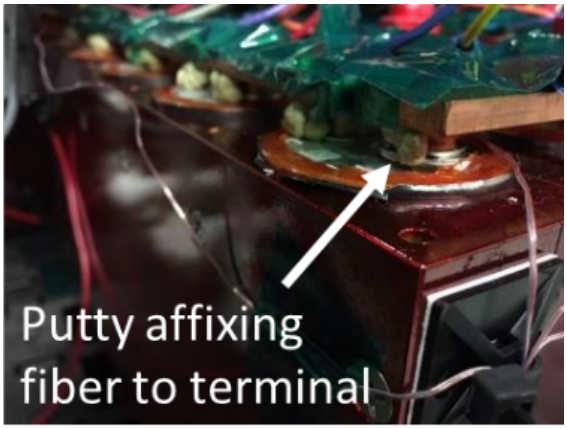

(c)

Figure 2.26: Photographs presenting installation of the Luna fiber optic sensor onto one of the 10S/1P modules. Above is a visual representation of the 'u-shape' of the fiber around each of the ten respective cells. In the lower left is a photo of the fiber wrapping from one row of a module to the next. In the lower right is a photograph highlighting the use of putty to hold the fiber in contact with each respective cell terminal.

Another sensor system installed on the 1000 V lithium-ion battery is a Li-ion Tamer® battery safety monitor developed by Nexceris, LLC. [12, 13]. The monitoring system is based on Nexceris' off-gas detection technology that is capable of providing early warning of lithium ion battery failures by continuously monitoring the atmosphere for off-gas events from the batteries. The sensing system consists of a number of strategically placed off-gas sensors, shown in Figure 2.27, that communicate with a host data acquisition system that runs a monitoring software. A set of

algorithms has been developed to interpret an array of gas sensor signals and provide reliable state of health monitoring. The monitoring system is not in contact with of the cells and is able to detect leaks from any lithium-ion chemistry. During early evaluation of the Li-on Tamer® sensor technology, Nexceris found that their sensor could detect a battery off-gassing event up to 20 minutes before catastrophic battery failure [21]. Through continuous improvement in their sensing technology, they have been able to integrate event detection algorithms and system designs for various types of battery systems.

Through their own developmental evaluations on both pouch and cylindrical format cells exposed to thermal and electrical abuse, Nexceris has shown that their monitoring approach provides sufficient time to apply mitigating actions to prevent thermal runaway from occurring. Figure 2.28 presents data collected by Nexceris LLC. when an 18650 cell at 100% state of charge (SoC) was thermally abused while the Nexceris sensor was used to monitor the off-gas signature. During the test, an off-gas event was detected but no mitigating actions were taken. The cell eventually entered thermal runaway approximately 4.5 minutes after the off-gas was detected.

Figure 2.29 presents data collected from an identical cell under the same abuse conditions. In this test, the source of external heating was de-energized when the monitor detected an off-gas event from the cell. The abused cell then safely cooled without entering into thermal runaway. The monitoring system is able to provide indication of pending failure of a battery, but it may also provide an opportunity to stop the cell from going into thermal runaway if a mitigating action such as active cooling or isolation from charge or load can be initiated.

As mentioned earlier, each half of the UTA lithium-ion battery is assembled on top of a plastic pallet with just over 1 m square dimensions. Each half has a polycarbonate case has been placed over the top of it. The case is not sealed in any

way but it does serve as somewhat of a containment around the battery. As shown in Figure 2.30, several Nexceris sensors are strategically placed around the battery to capture both reference and 'near battery' air samples. Each sensor is bolted to either the polycarbonate case or the pallet, depending upon its respective position.

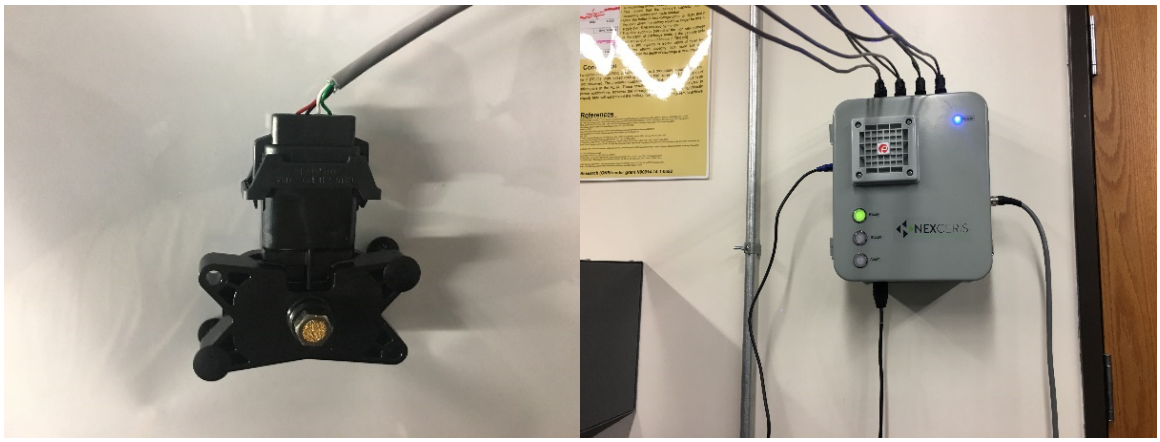

(a) (b)

Figure 2.27: Photograph of a Nexceris Li-Ion Tamer® off-gas sensor (a) and the data acquisition system installed at UTA (b).

The sensor has been installed on the UTA LIB for a little over one year and to date there have been no false positives reported by the sensor. There have been no cell failures, and therefore there is no additional information about the sensing system that can be reported as of this writing. It is not expected to observe any measurement of cell off-gassing outside of any extreme abuse conditions or failures of the cells.

2.4.3 Experimental Results

The lithium-ion battery has been experimentally evaluated under continuous and transient load conditions at power levels as high as 250 kW. At lower power

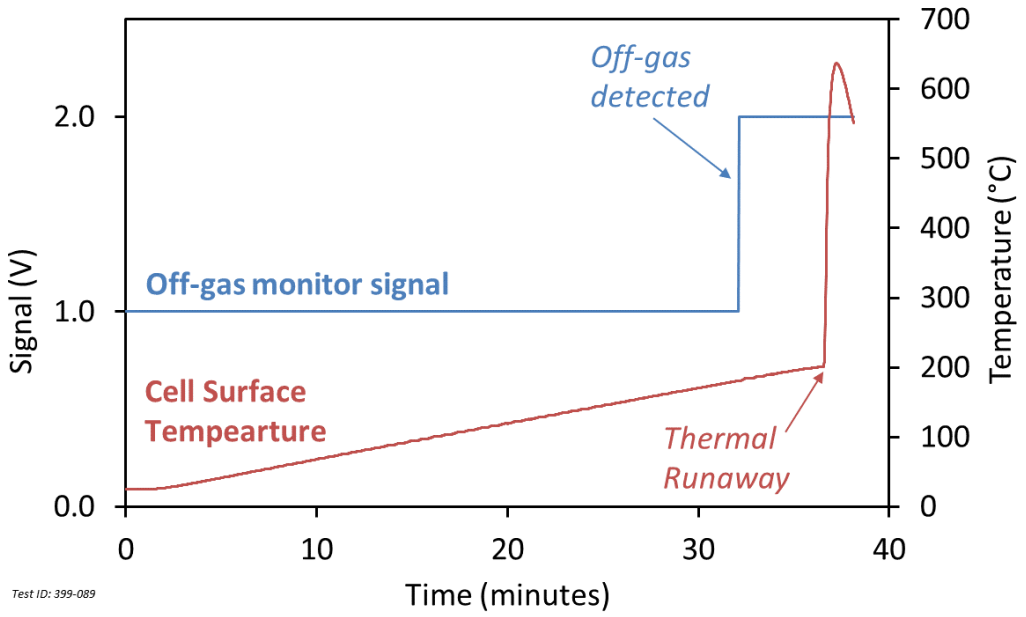

Figure 2.28: Thermal abuse of 18560 cell. Nexceris' Li-ion Tamer® monitor provided 4.5 minutes of early warning prior to thermal runaway.

levels, the battery performs as expected and there is little elevation in temperature due to the adequate cooling that is utilized. At the higher power levels, there is significant thermal elevation and therefore it is a sample of these results that will be discussed here. Figure 2.31 presents voltage and current plots measured during an experiment. The battery was loaded for 5 seconds, drawing a constant power of 250 kW, then allowed to rest for 1 second before being laoded again. This process was repeated until fifty 5 second discharges has been performed, for a total runtime of 300 seconds. As shown in the plots, the average current drawn from the battery is roughly 285 A, with current increasing as the test progresses due to the decreasing battery voltage, a consequence of increasing depth of discharge (DoD). Assuming a cell impedance of roughly 0.5 mΩ, each cell dissipates roughly 40 W of heat when 285 A is being conducted.

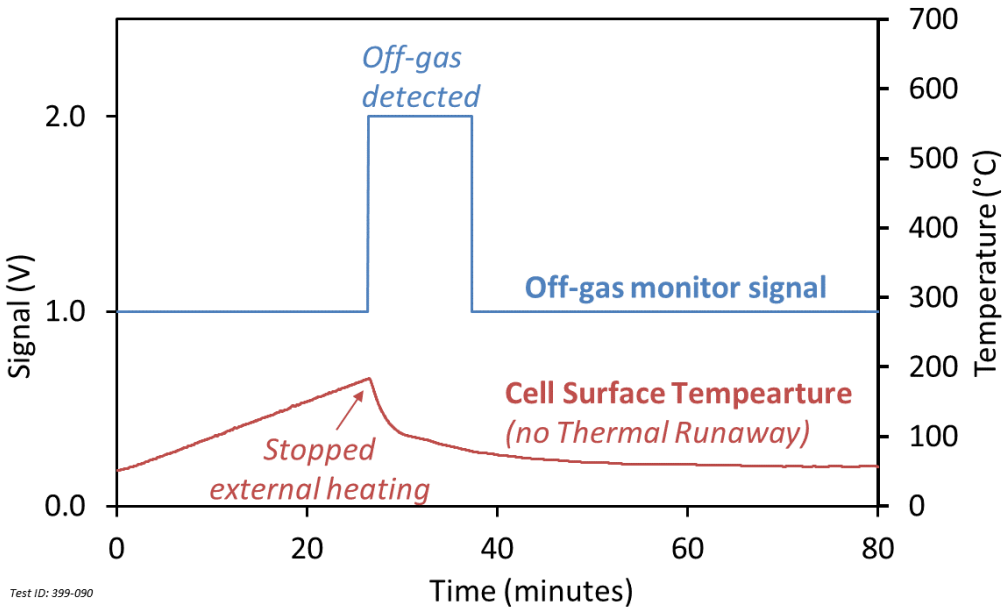

Figure 2.29: Repeat of test shown in Figure 10 except the cell abuse was stopped when off-gas is detected. This demonstrates off-gas monitoring can provide early warning sufficient to prevent thermal runaway if mitigating actions are taken.

The Luna ODiSI-B data acquisition software allows the user to pinpoint and save select points along the fiber sensor as locations of interest. During installation of the sensor on the lithium-ion battery, the location of each terminal throughout the 280S/1P battery was saved as a location of interest. Thermal elevations throughout the battery are measured using the ODiSI-B and they can be plotted in many different ways. Figure 2.32 presents surface plots of the thermal data measured at each of the ten respective negative terminals throughout the discharge of three of the twenty-eight modules, modules 8, 13, and 14, respectively.

In all of the plots, the data shows how the temperature of each module increases throughout the discharge, as expected, and then decays once the experiment completes. While each of the cells' thermal elevation is very similar in overall shape, there are variations measured. The data from module 8 is quite consistent, however

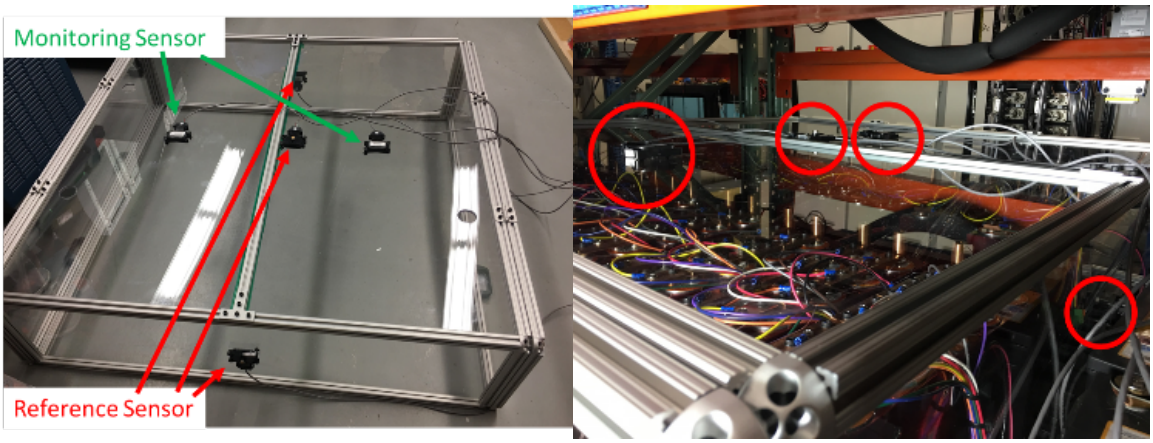

(a) (b)

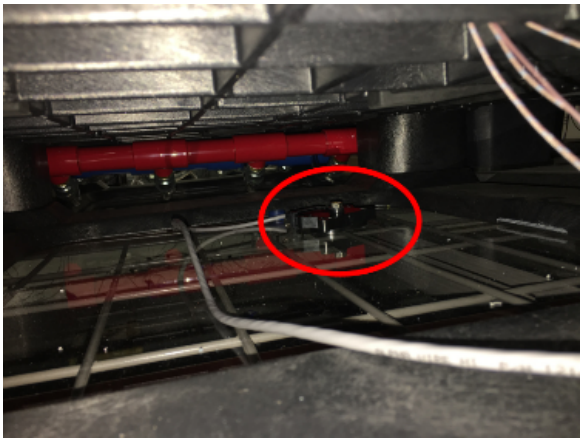

(c)

Figure 2.30: Photographs of (upper left) the polycarbonate case on which three reference and two monitoring sensors are mounted, (upper right) photograph of the case installed over its respective half of the LFP-LI battery, and (lower left) a photograph of a reference sensor positioned beneath the battery, within the plastic pallet.

there are a few temperatures measured that are as much as 10°C hotter than the average temperature of 45°C. The data from module 13 shows much more significant variation. Temperatures as high as 75°C are recorded on this module while others are as low as 45°C, similar to what was recorded on module 8. Note that measurements of temperatures this high indicate cell conditions that exceed the manufacturer's rec-

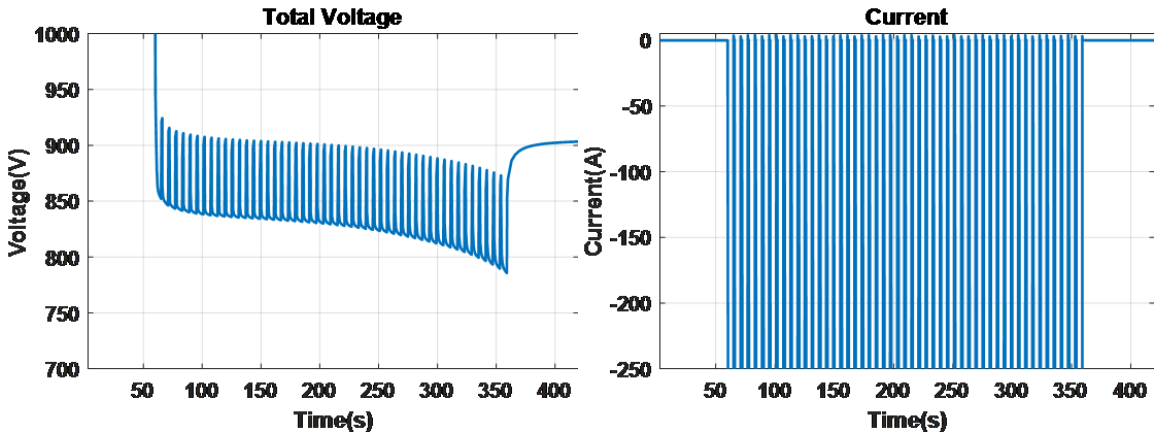

(a) (b)

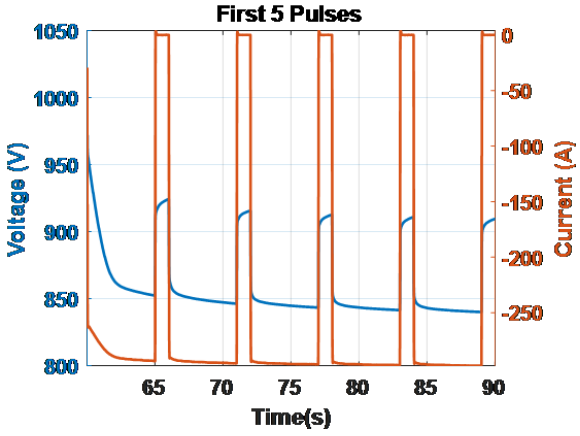

(c)

Figure 2.31: Current and voltage measurements made during the 250 kW discharge of the battery. The battery was discharged in a 5 second on / 1 second off transient profile for 300 seconds.

ommendation for safe operation, and were only allowed under the close supervision of the experienced researcher. This type of operation is not recommended in a typical battery system. These elevated temperatures are likely from lossy, imperfect highly-ohmic connections with the cell terminals at the elevated rates in which the battery has been operated. In most cases, thermal resolution this high is not measured and therefore this data highlights the benefits of the ODiSI-B. If there is in fact a higher ohmic loss, this tool has identified the potential weakness as a location that needs to

be investigated. When this type of thermal resolution is not captured, these potential issues of concern are never identified and only the select locations that are monitored by thermocouples or thermistors are used to monitor the entire battery. The data from module 14 is the most consistent with nearly all of the cells measuring a peak temperature between 45°C and 50°C.

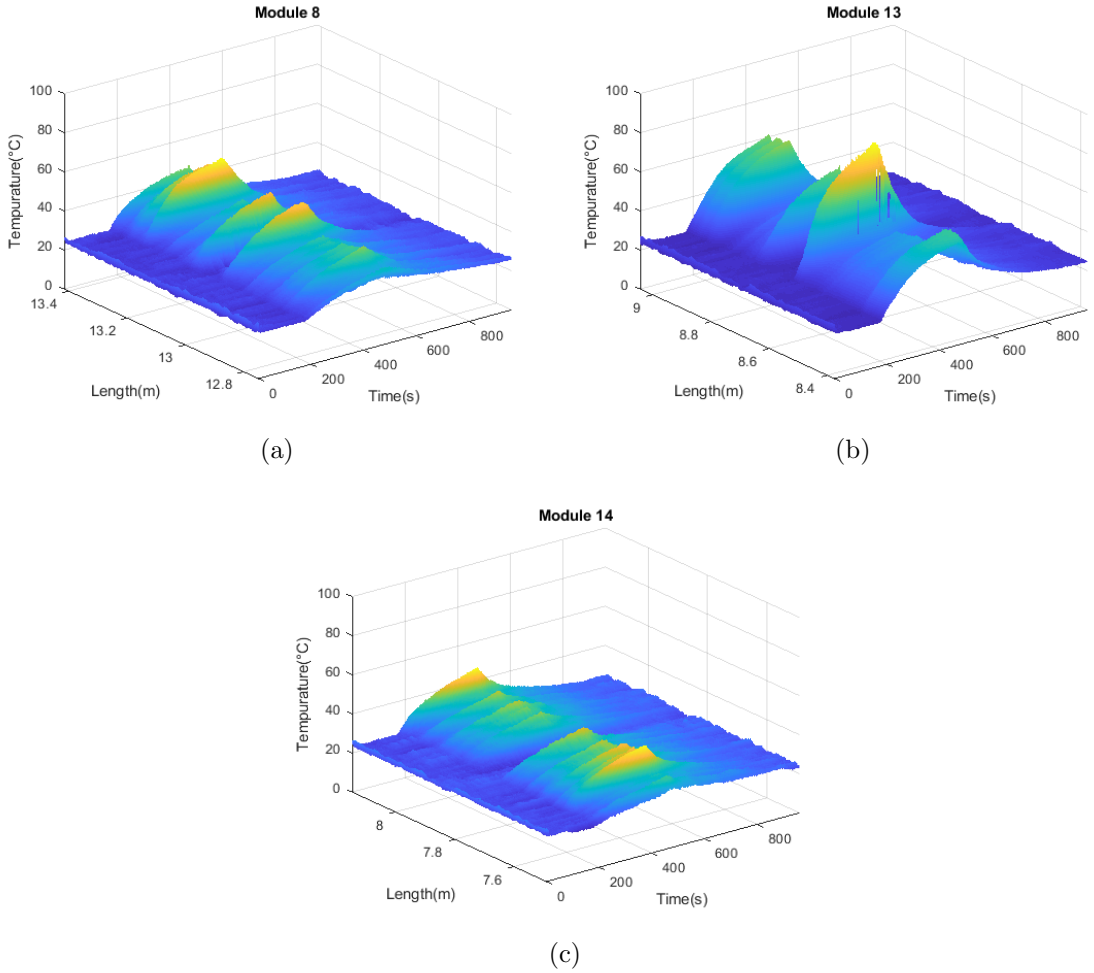

Figure 2.32: Surface contour plots from the ODiSI-B, each of which presents the thermal data measured on each of the ten respective negative terminals of its respective 10S/1P module.

Figure 2.33 plots the thermocouple measurements made on each of the twenty-eight respective modules. Note that initially four thermocouples were installed on each of the twenty-eight modules. Three of those were thermally epoxied to the negative terminal of random cells within the modules. The fourth was fed axially down the length of the cell and taped to the side of the cell using polyimide tape. Some of those were found to be either broken or electrically connected to the battery. The thermal data presented in Figure 2.33 is that off all the working thermocouples within the battery. As shown, the temperatures measured throughout the battery vary significantly. On average, temperatures ranging between 40°C and 50°C are measured, though temperatures as low as 25°C and as high as 88°C are also recorded. The significantly lower temperatures are those measured on the sides of the cells. Keep in mind that the sides of the cells are in thermal contact with the cooling block and therefore it is expected that those will not significantly rise.

Finally, some comparisons were made between data measured by thermocouples and the Luna ODiSI-B at the same location within the battery. Comparisons of terminal temperatures measured on modules 1, 8, and 6 are shown respectively in Figure 2.34. These three plots are representative of the many comparisons made of all the thermocouple and ODiSI-B data recorded. In the comparison made on module 1, there is some discrepancy between the measurements but it is minor, only a few degrees Celsius, and the thermal response of the fiber is shown to be slightly faster than that of the thermocouple, as expected, due to the fiber's reduced thermal mass.

In the comparison made on module 8, the agreement is remarkably good with little variation in the thermal response. The slower response in this case is likely a result of a small thickness of putty being between the fiber and the terminal, or the presence of mounting putty increasing the thermal mass of the fiber at that point higher than that of the thermocouple. The comparison made of module 6 shows the

most deviation, with a variation between the two amplitudes and also the shape of the curves. This could be due to the marked location being slightly off the cell terminal, the presence of strain added locally to the fiber as the cell terminals expand while heating, or possibly the presence of minor vibrations caused from air movement, etc., during the experiment.

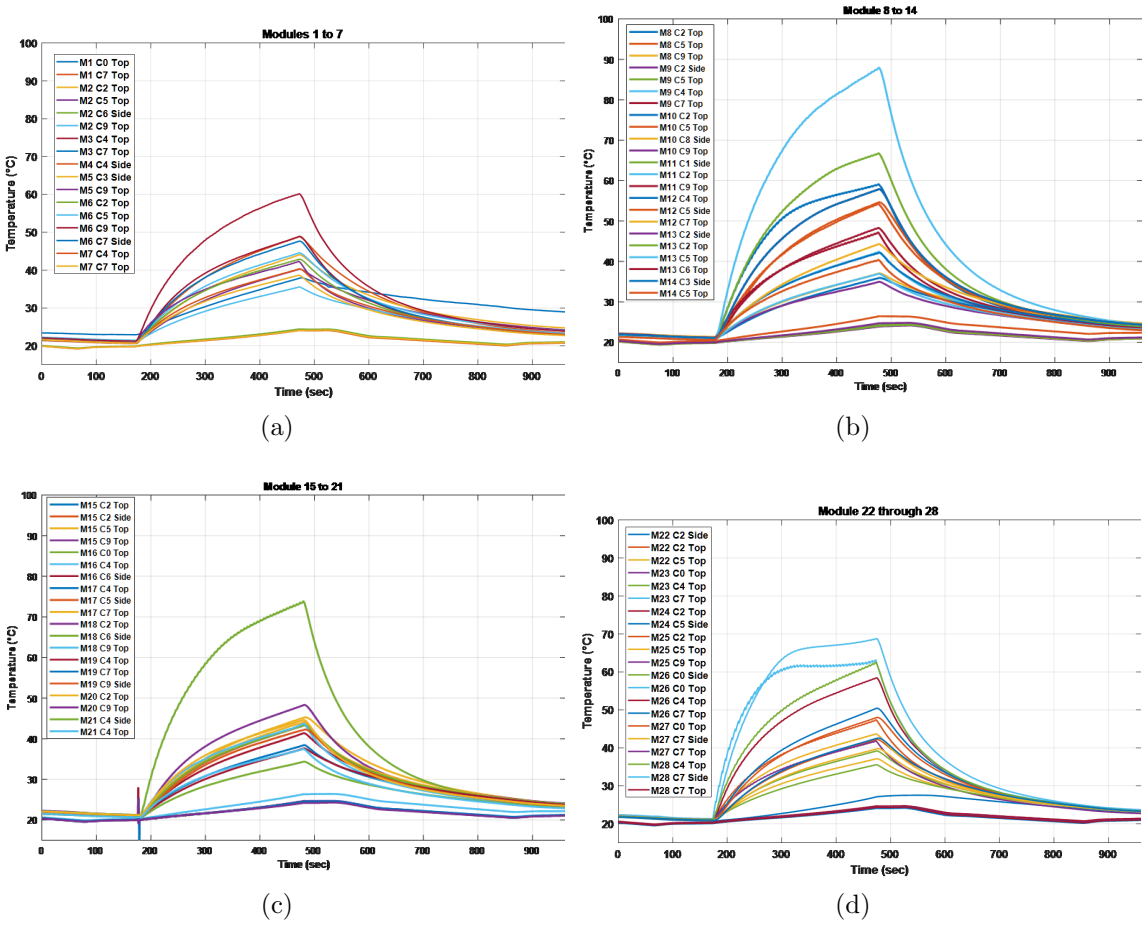

Figure 2.33: Plots of the thermocouple measurements recorded on each of the twenty-eight respective 10S/1P modules. Labels are M C Thermocouple Location, where M is module number and C is cell number, respectively.

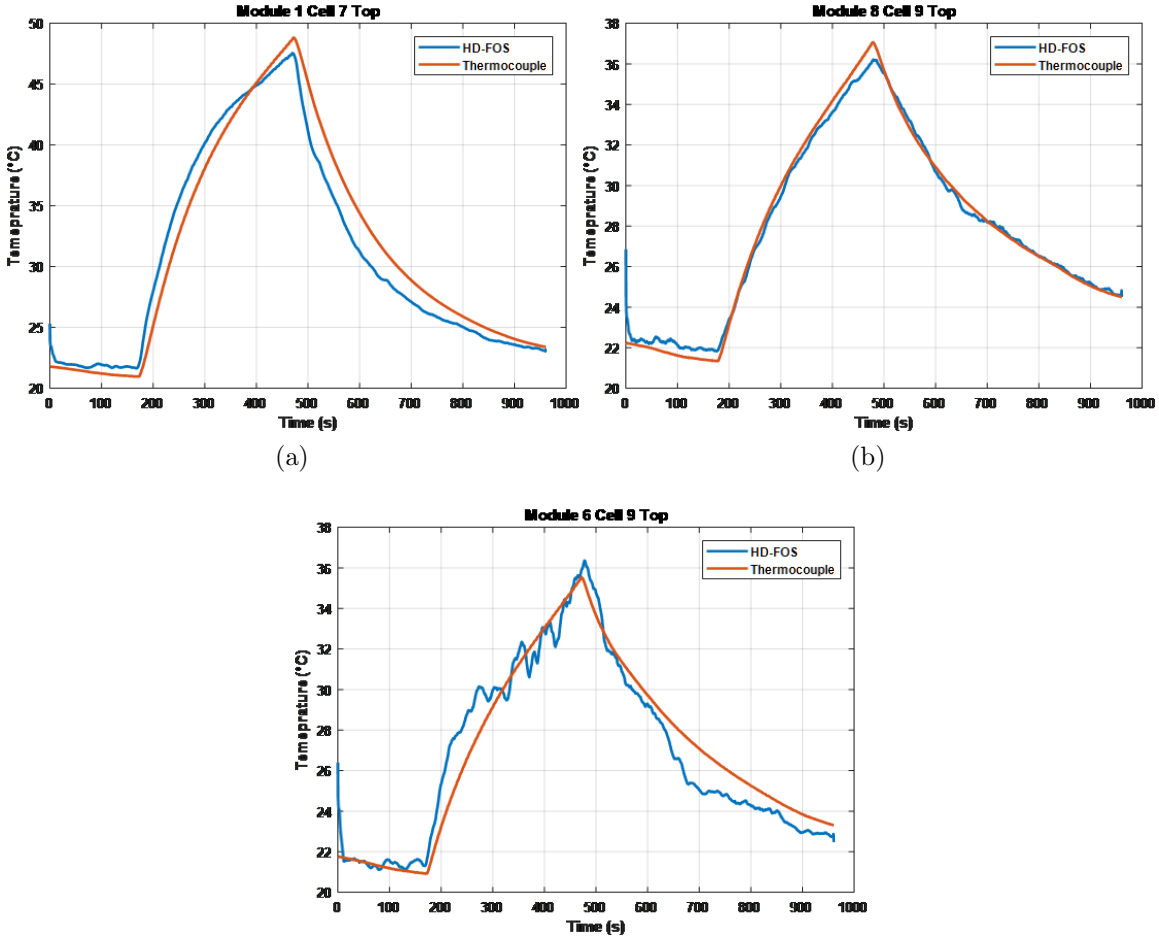

Figure 2.34: Comparisons of the thermal measurements made between a few select thermocouples and the ODiSI-B fiber optic sensor at each of the same respective locations.

In the chapter presented here, the design of a unique 1000 VDC battery has been presented. The battery is assembled using Saft VL30AFe lithium-iron-phosphate lithium-ion (LFP-LI) cells, a robust battery management system, novel cell cooling, novel thermal diagnostics, and a novel battery off-gas sensing technology. This section has highlighted the challenges faced when designing and commissioning such a system and the capabilities each of the unique diagnostic tools brings to a battery like this one. It has been shown that a fiber optic temperature sensing system can be

used to measure significantly more locations within a high cell count battery than is likely feasible using conventional thermocouples or thermistors. There is quite good agreement between the thermocouples installed on the battery and the data recorded by the fiber optic sensor. This battery will now be used as a testbed on which to continue to study these types of advanced diagnostics and work has only begun to identify the cause of the few variations presented. The next steps will involve integration of the ODiSI-B and the Nexceris sensing system with the BMS so that all three monitoring tools are able to communicate seamlessly. This system is also to be included in the MVDC testbed described in Chapter 4.

CHAPTER 3

MODELING AND SIMULATION OF BATTERY SYSTEM

3.1 Individual Cell Model

Using the information that has been gathered in Chapter 2 regarding the electrical, thermal, and lifetime testing of the Saft VL30AFe lithium iron phosphate cell, a cell model has been proposed that will accurately represent the cell in a simulation scenario. This model combines the voltage curve characteristics, the thermal properties of heat generation due to ohmic losses during conduction, and the capacity fade experienced by the cell during operation. The intention of this model is to create a full-scale model of the 1 kV lithium ion battery that is comprised of 280 individual cell models, along with a BMS model for the implemented system.

The model is made within the MATLAB/Simulink environment to make it compatible with the model of the full scale battery and proposed testbed. Using data obtained from the single-cell testing discussed previously, a model has been generated that accurately reflects the operational characteristics of the cell. An example of the performance of the modeled cell is shown in Figure 3.1.

The base model used is shown in Figure 3.2 [22]. This model is a comprehensive representation of the operational characteristics of a single cell lithium ion battery. It contains parametrical information on charge and discharge characteristics, thermal effects on the cell, and aging effects. The governing electrical equations for the referenced model shown in Figure 3.2 are given in Equation 3.1 [22].

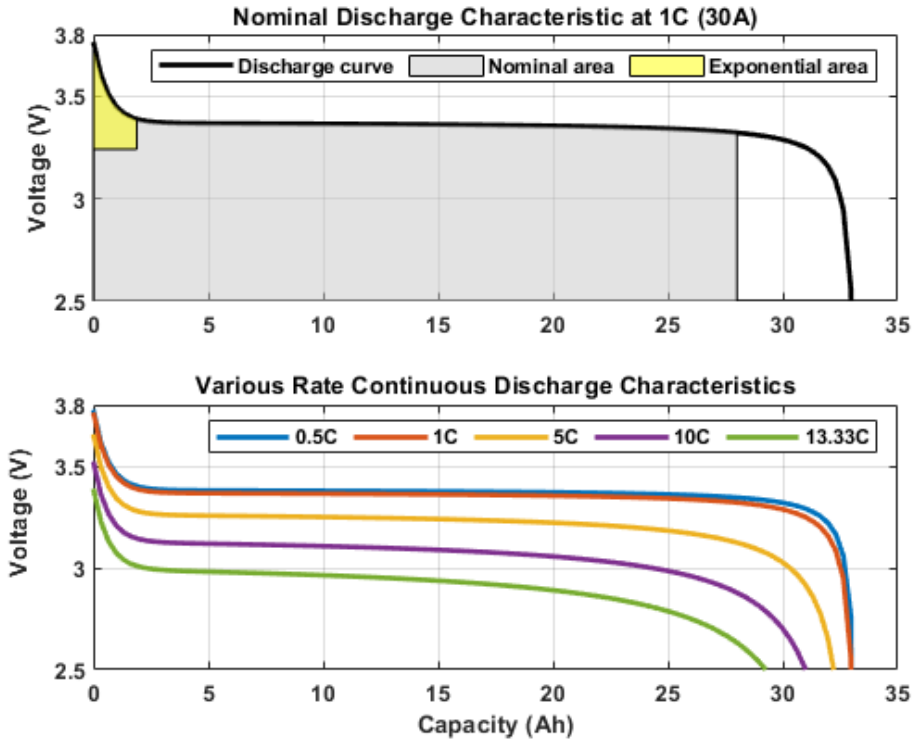

Figure 3.1: Discharge characteristics of the modeled lithium ion cell at various continuous rates. The voltage curve characteristics are shown in in the top plot and the discharge curves for the range of rates performed during the baseline procedure in Figure 2.2 are shown in bottom plot.

$$
\begin{aligned}
f_1(i_t, i^*, i) &= E_0 - K \cdot \frac{Q}{Q - i_t} \cdot i^* - K \cdot \frac{Q}{Q - i_t} \cdot i_t + A \cdot exp(-B * i_t) \\
f_2(i_t, i^*, i) &= E_0 - K \cdot \frac{Q}{i_t + 0.1 * Q} \cdot i^* - K \cdot \frac{Q}{Q - i_t} \cdot i_t + A \cdot exp(-B * i_t)
\end{aligned}
\tag{3.1}
$$

where

E_0 is the constant voltage (V)

K is the polarization constant (V/Ah) or polarization resistance (Ω)

i_* is the low frequency current dynamics (A)

i is the battery current (A)

i_t is the extracted current (Ah)

Q is the maximum battery capacity (Ah)

A is the exponential voltage (V)

B is the exponential capacity (Ah^{-1})

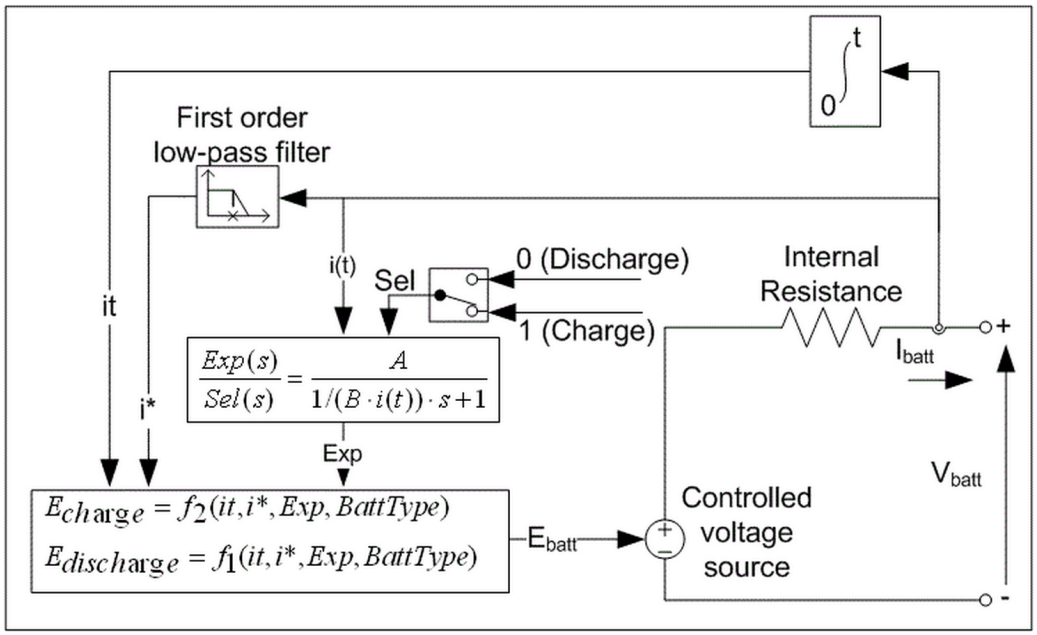

Figure 3.2: Diagram of the equivalent circuit representing the battery model.

3.1.1 Electrical Characteristics and Nonidealities

Characteristics of the battery outside of standard operational electrical characteristics have also been considered during the modeling of the cell. The first of these non-idealities is the thermal properties of the cell and the impact that this has on cell performance. The thermal characteristics of the battery model are governed by Equation 3.2.

$$
\begin{aligned}
f_1(i_t, i^*, i, T, T_a) &= E_0(T) - K(T) \cdot \frac{Q(T_a)}{Q(T_a) - i_t} \cdot (i^* + i_t) + A \cdot exp(-B \cdot i_t) - C \cdot i_t \\
V_{batt}(T) &= f_1(i_t, i^*, i, T, T_a) - R(T) \cdot i \\
f_2(i_t, i^*, i, T, T_a) &= E_0(T) - K(T) \cdot \frac{Q(T_a)}{i_t + 0.1 \cdot Q(T_a)} \cdot i^* - K(T) \cdot \frac{Q(T_a}{Q(T_A) - i_t} \\
&\quad + A \cdot exp(-B \cdot i_t) - C \cdot i_t \\
V_{batt}(T) &= f_1(i_t, i^*, i, T, T_a) - R(T) \cdot i \\
&\text{with} \\
E_0 &= E_0|_{T_{ref}} + \frac{\delta E}{\delta T}(T - T_{ref}) \\
K(T) &= K|_{T_{ref}} \cdot exp\left(\alpha \left(\frac{1}{T} - \frac{1}{T_{ref}}\right)\right) \\
Q(T_a) &= Q|_{T_a} + \frac{\Delta Q}{\Delta T} \cdot (T_a - T_{ref}) \\
R(T) &= R|_{T_{ref}} \cdot exp\left(\beta \left(\frac{1}{T} - \frac{1}{T_{ref}}\right)\right)
\end{aligned}
\tag{3.2}
$$

where

T_{ref} is the nominal ambient temperature (K)

T is the cell temperature or internal temperature (K)

T_a is the ambient temperature (K)

$E|T$ is the reversible voltage temperature coefficient (V/K)

α is the Arrhenius rate constant for the polarization resistance

β is the Arrhenius rate constant for the internal resistance

$\Delta Q/\Delta T$ is the maximum capacity temperature coefficient (Ah/K)

C is the nominal discharge curve slope (V/Ah)

3.1.2 Cell Aging Considerations

The second non-ideality to be considered when modeling the cell is the impact of aging on the cell's capacity and electrical performance. Cell aging characteristics incorporated within the battery model are expressed in Equation 3.3.

$$Q(n) = \begin{cases} Q_{BOL} - \epsilon(n) \cdot (Q_{BOL} - Q_{EOL}) & \text{if } k/2 \neq 0 \\ Q(n-1) & \text{otherwise} \end{cases}$$
$$R(n) = \begin{cases} R_{BOL} - \epsilon(n) \cdot (R_{EOL} - R_{BOL}) & \text{if } k/2 \neq 0 \\ R(n-1) & \text{otherwise} \end{cases} \tag{3.3}$$

with

$$n = kT_h \qquad (k = 1, 2, 3, ...\infty)$$

where

T_h is the half-cycle duration (sec)

Q_{BOL} is the battery maximum capacity at the beginning of life (Ah)

Q_{EOL} is the battery maximum capacity at the end of life (Ah)

R_{BOL} is the battery internal resistance at the beginning of life (Ω)

R_{EOL} is the battery internal resistance at the end of life (Ω)

ϵ is the aging factor (% aged)

The aging factor is expressed in Equation 3.4.

$$\epsilon = \begin{cases} \epsilon(n-1) + \frac{0.5}{N(n-1)} \left(2 - \frac{DOD(n-2)+DOD(n)}{DOD(n-1)}\right) & \text{if } k/2 \neq 0 \\ \epsilon(n-1) & \text{otherwise} \end{cases}$$

$$N = H \left(\frac{DOD(n)}{100}\right)^{-\xi} \cdot exp\left(-\psi\left(\frac{1}{T_{ref}} - \frac{1}{T_a(n)}\right)\right) \cdot (\bar{I}_{dis}(n))^{-\lambda_1} \cdot (\bar{I}_{ch}(n))^{-\lambda_2} \tag{3.4}$$

where

DOD is the battery depth of discharge (%)

N is the maximum number of cycles (cycles)

H is the cycle number constant (cycles)

ξ is the exponent factor for the DOD

ψ is the Arrhenius rate constant for the cycle number

$\bar{I}_{dis}$ is the average discharge current (A)

$\bar{I}_{ch}$ is the average charge current (A)

λ_1 is the exponent factor for the discharge current

λ_2 is the exponent factor for the charge current

With these non-idealities taken into consideration, the battery cell model has been expanded to be comprehensive enough for usage in a detailed full-scale battery model. This full-scale model is described in the next section.

3.2 Full-Scale Battery System Model

This comprehensive single cell model has been extrapolated for usage in a model that will encompass the full 1000 VDC lithium ion battery that has been assembled for the testbed. Using small perturbations in the determined model parameters,

280 individual cell models have been combined to create a full-scale battery model. Slight variations have been made in cell capacity, ESR, and state of charge to allow for reasonable representation of the real, physical system. The Simulink model that has been made is shown in Figure 3.3.

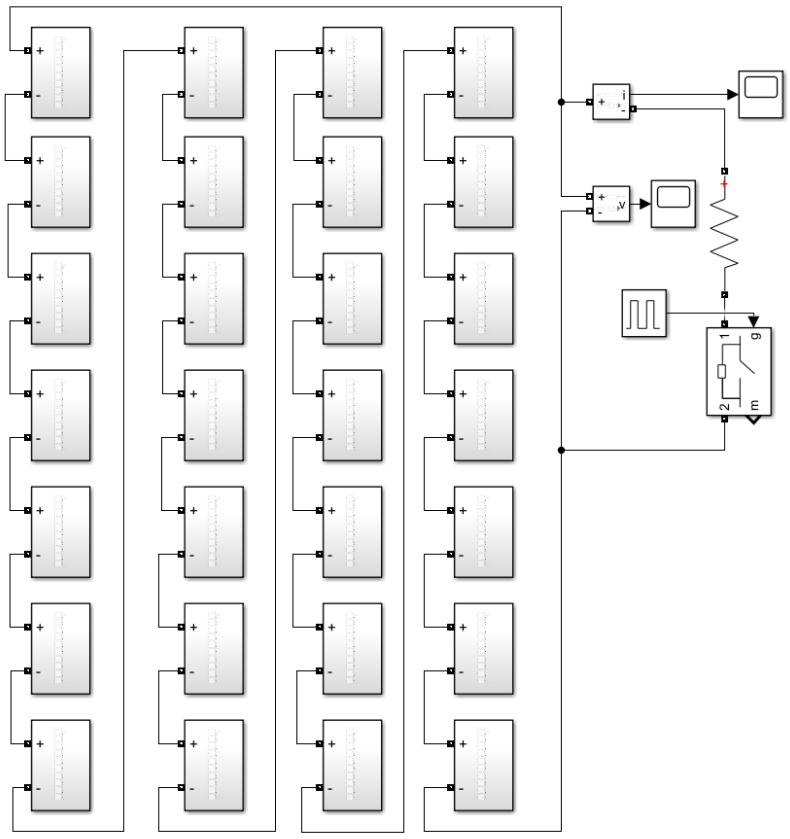

Figure 3.3: Simulink diagram of the full-scale 1000 V lithium ion battery model.

This model is comprised of 28 subsystems - each representing a single liquid-cooled module of ten individual cells. Each individual cell model has been given slight deviations to the nominal setpoints on state of charge, capacity, and ESR to add a level of realism and viability to the analysis done with the model.

A simple resistive transient load is shown in the diagram. This load is set to discharge the battery at period of 10 seconds with a duty cycle of 50% to demonstrate the transient performance of the battery model, as well as show how the model behaves as the cells are discharged.

3.2.1 Battery Management System

The battery management system for the fully assembled battery has also been modeled. This model is accurate to the actual operation of the installed BMS. The BMS works by monitoring each individual cell voltage. When the cell voltage exceeds the absolute maximum or minimum voltages (3.8 V and 2.5 V, respectively), then the BMS generates an alarm signal for usage in the control system. The BMS is also responsible for balancing the cells to the same state of charge. Due to the extremely flat nature of the voltage curves of the cell chemistry chosen, balancing is performed in the upper 10 to 15 percent of the state of charge range. This system uses a passive balance system that burns off excess energy in cells with higher SOCs in the form of heat dissipated in a resistive element. The BMS monitors the cell voltages, and enables balancing by connecting the resistive element across the cell's terminals when the cell reaches a terminal voltage of 3.5 V. This balance current of approximately 300 mA is maintained until the cell reaches a terminal voltage of 3.45 V. This hysteresis is placed on the cell voltage requirements for balancing to make sure that there is no unstable oscillations in the balancing system. Due to the somewhat simple logic that is used here for the balancing scheme, a simple model of the BMS has been created and implemented on the 1000 V. Although simple, this model accurately describes the operation of the BMS. The governing equations for the BMS are shown in Equation 3.5.

$$Alarm = \begin{cases} True & \text{if } V_{OC} < 2.5 \text{ or } V_{OC} > 3.8 \\ False & \text{otherwise} \end{cases}$$

$$I_{bal} = \begin{cases} V_{OC}/R_{bal} & \text{if } V_{OC} \geqslant 3.5 \\ 0 & \text{otherwise} \end{cases} \tag{3.5}$$

If balance is active:

$$I_{bal} = \begin{cases} V_{OC}/R_{bal} & \text{until } V_{OC} \leqslant 3.45 \end{cases}$$

where

I_{bal} is the BMS balance current for the cell (A)

V_{OC} is the measured terminal voltage of the cell (V)

R_{bal} is the BMS balance resistance (Ω)

$Alarm$ is the fault signal generated by the BMS during undesired operational conditions

Using the operational characteristics outlined in Equation 3.5, a BMS model can be implemented with a simple script within the MATLAB/Simulink environment to load the cell models with a balance resistance in the appropriate usage scenarios.

With all of the battery systems outlined and described in the Simulink environment, a full model has been presented that can be implemented within other systems to investigate integration and control of the battery system within that larger system. The motivation for the creation of the model is for integration into an inclusive system model of the MVDC testbed proposed within the following chapter.

CHAPTER 4

MVDC ENERGY CONVERSION TESTBED

4.1 Scope of Work and Motivation

A large-scale, one-of-a-kind medium voltage (MV) AC/DC testbed testbed has been designed and constructed to simulate and emulate the complex operation of microgrid system consisting of many different busses and loads. The main goal of this infrastructure is to simulate and model distributed generation in an islanded microgrid system with complex base and transient loads, as well as to study the impact of mixing more conventional generation sources with energy storage sources in the form of medium voltage battery systems. Many current microgrid systems rely upon electrical generation from several interconnected sources that may include diesel and gas turbine driven generators, flywheels, and electrochemical batteries, among others. Integration and control of the AC/DC sources within a single power system is not an easy task and is the basis for the installation performed here. In the testbed constructed, AC/DC generation sources are interconnected onto multiple MVDC buses operating at 1 kVDC, 6 kVDC, and 12 kVDC, respectively. Since fossil-fuel driven generation is not practical alone for driving extreme high-power transient loads, either mechanically or electrically, high power electrochemical batteries are being used as a buffer. Uniquely designed high voltage DC and AC loads are being utilized to emulate conventional and advanced, modern microgrid loads that are controlled remotely by the operator. An OPAL-RT hardware in the loop (HIL) platform is being deployed to expand the hardware and simulate its interaction with hardware not physically possessed in the lab. Previous work shown here has shown focus on studying the

performance, reliability, and aging of electrochemical cells when cycled at high rates at the material, cell, module, and even 1000 VDC level. At lower scale, there has also been work done previously studying power system architectures integrating AC/DC sources for driving transient loads.

In future microgrid systems, there could be several unique high power loads which will be operated in both continuous and transient modes of operation [23, 24]. When high demand transient loads are sourced, they drag down their source's DC or AC bus voltage considerably, heavily impacting the power quality. While generators alone can likely be sized properly to account for large transient loads, they will be much larger than necessary for most of the system's operations and will take up valuable space and resources that is desperately needed for other things. With this in mind, DC and AC sources must be integrated into unique power system architectures that employ energy generation and storage and these sources must be capable of working together to supply the intermittent loads that exceed a more moderately sized generator's capacity while also minimizing variations in its output power [25, 26, 27, 28]. Power system architectures that combine electrochemical batteries and capacitors with standard diesel or gas turbine power generation are optimal [27, 28]. This leads to both DC and AC buses existing in the architecture, requiring active power conversion between DC and AC sources. This is not a new challenge, as it is one faced every day as power systems engineers try to integrate batteries, solar panels, and wind turbines onto the already existing electrical grid, either in homes or in the distribution network, but the loads being sourced in those applications could potentially be vastly different than those being sourced by a complex microgrid and therefore special attention and research is needed to understand how to overcome these challenges.

The scope of the work presented here is to scale up research to voltage and power levels that are more relevant to future microgrid applications. A testbed has been designed and installed on which busses conducting 1 kVDC, 6 kVDC, 12 kVDC, 480 VAC, and 4160 VAC are present. Grid tied and rotating machine sources are installed. The testbed leverages the 1 kVDC batteries designed and commissioned through the previously shown efforts, as well as the OPAL-RT HIL platform. The testbed is designed to study the design and control of these multiple AC/DC sources, their power quality when they are transiently loaded, and the interconnection challenges that will be faced. The hardware procured and the testbed that was installed will be discussed in the section that follows.

4.2 Design of MVDC Testbed

Integration of multiple distributed generation sources and loads into a single electrical power system architecture is incredibly difficult and requires a high degree of control for reliable autonomous operation. Though many of the various sources and loads proposed for deployment in future systems have been independently researched, modeled, and experimentally validated in laboratory settings, interconnection of multiple types of sources and loads within a single integrated power system is one that has not been widely demonstrated. With this in mind, the objective of this research is to design and construct a system of hardware that is all interconnected into a single testbed deploying multiple distributed generation sources and loads for emulated operation. A simple photographic one-line diagram of the hardware as it is assembled is shown in Figure 4.1. An electrical one-line diagram is shown in Figure 4.2.

Figures 4.1 and 4.2 show how the testbed was assembled to condition AC power to DC to drive MVDC loads and how the 1 kV energy storage module can be used to supply its own load or buffer the AC generation. The primary source of power is

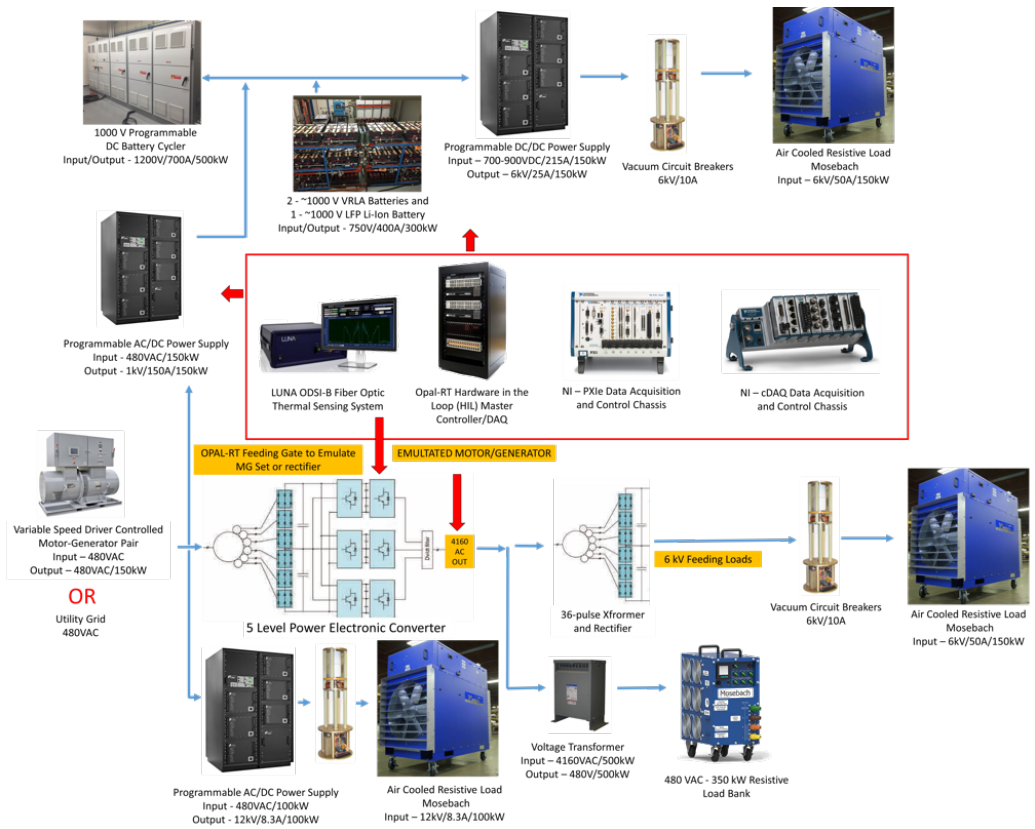

Figure 4.1: Pictorial one-line diagram of the distributed generation source testbed assembled for this effort. The items highlighted in green are the most recent additions. The remaining parts were either previously procured or were already possessed by the lab.

the 150 kW electrical motor-generator set, though it was also configured such that the electrical grid can be used to power all or some of the testbed as needed. Each individual component of the testbed will be discussed in the subsections that follow along with some justification for why they were chosen and how they will be used to support the effort to study the reliability, control, and operational challenges facing the integration of a high voltage, 1 kVDC, electrochemical energy storage device with a rotating generator's three-phase, 480 VAC bus while supplying transient MVDC loads.

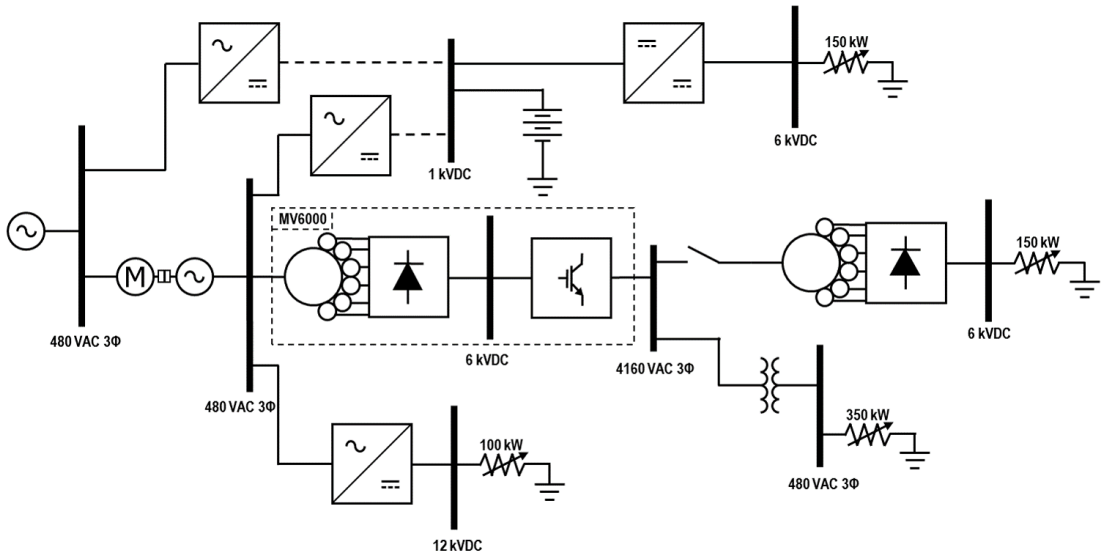

Figure 4.2: Electrical one-line diagram of the distributed generation source testbed assembled. Dashed interconnections represent bus connections that have specific usage scenarios.

4.2.1 150 kW KATO Electrical Motor – Generator Set

In the lower left hand corner of 4.1, a variable frequency drive (VFD) controlled electrical motor – generator (MG) set is shown. This 150 kW generator was procured from KATO Engineering. Its output supplies three phase, 480 VAC to the testbed and acts as the primary source of power under normal operation. The MG set utilizes a 300 HP four-pole induction motor to spin the four-pole synchronous generator to 1500 – 2000 RPM. The generator is excited using a brushless exciter. The motor is energized using a variable frequency drive, as mentioned before, through a 400 A electrical feed supplied at 480 VAC. Photographs of the generator shortly after they were installed in the lab are shown in Figure 4.3. Dimensioned drawings of the MG set are shown in Figure 4.4.

The generator was designed by KATO to allow for the amplitude of its output voltage as well as its output frequency to be adjusted remotely by the user through

(a) (b)

(c)

Figure 4.3: Photographs showing the MG set (a), internals of the control and VFD cabinets (b), respectively, and the front control section of the controls cabinet (c).

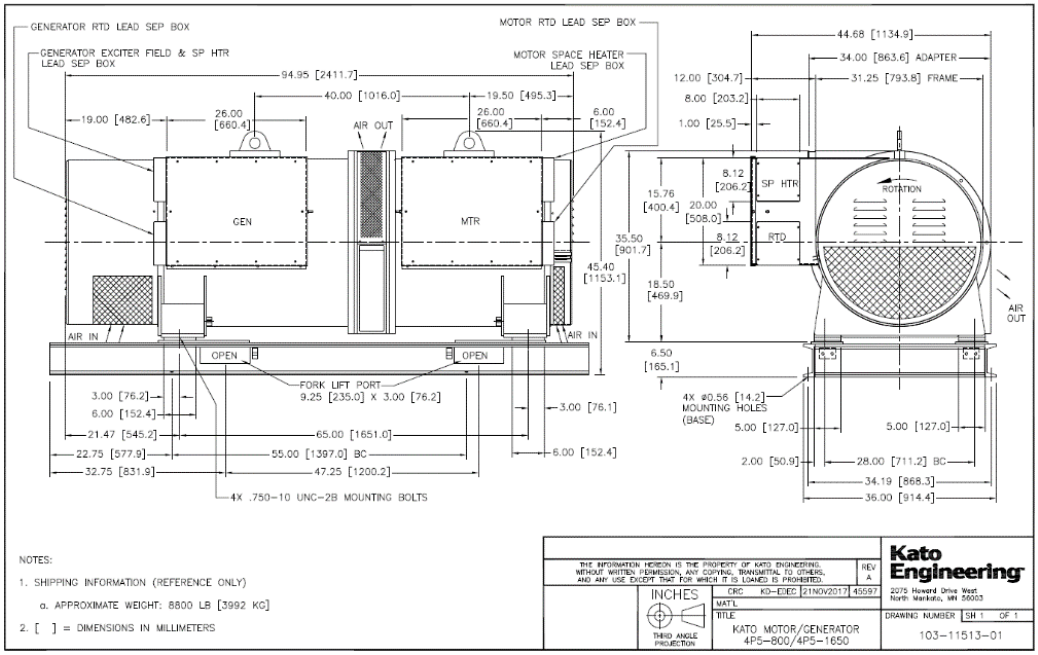

Figure 4.4: Dimensioned drawing of the KATO MG set as fabricated.

analog signal control. The voltage is variable from -20% (384 V) to +20% (576 V) of the nominal 480 VAC using a 0 V to 10 V analog voltage. The output frequency is adjustable from -17% (50 Hz) to +11% (67 Hz) of the nominal 60 Hz using similar 0 V to 10 V analog control. This feature was added so that the generator's output could be modulated using an OPAL-RT hardware in the loop (HIL) platform. This is desirable since the inherent electrical and mechanical properties of the MG set do not directly match those of a fielded diesel or gas-turbine driven motor-generator set. Through the use of validated Simulink models of a fielded MG set, it is possible to use the OPAL-RT to emulate a fielded generator using the KATO MG set as the amplifier. Since the KATO MG set has its own inherent electrical and mechanical properties that cannot be changed, it is unclear what the response of the analog control will be relative to the way a fielded MG set will behave. This opens up a research task that could be investigated in support of the this emerging technology. Operation of

the MG set is controlled locally on an HMI panel, as well as remotely with a LAN connection. This is shown in Figure 4.5. The output of the MG set is supplied three ways. These include connections into an 80 kW - 480 VAC to 12 kVDC switch mode power supply, a 150 kW – 480 VAC to 1.2 kVDC switch mode power supply, and finally into a 225 kW - 480 VAC to 4160 VAC, five level power electronic motor drive. Each of these will be described in the next few sub-sections.

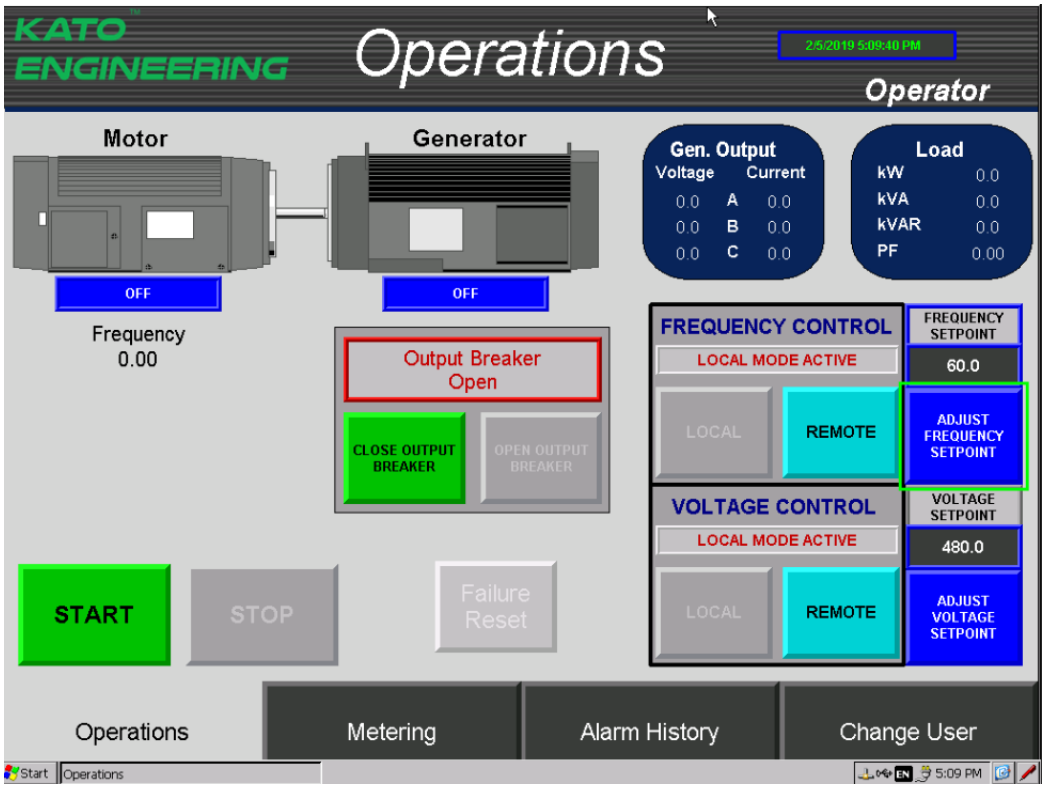

Figure 4.5: The interface used to control the operation of the MG set and output breaker. The voltage output and frequency setpoints can be changed here or through analog voltage control.

4.2.2 80 kW, 480 VAC to 12 kVDC Programmable Power Supply

Working from the bottom to the top of Figure 4.1, the first electrical load connected to the KATO MG set is a 480 VAC to 12 kVDC switch mode power supply that is operable up to 80 kW. These two 40 kW power supplies, which are operable in parallel using a master-slave configuration, are designed by the TDK-Lambda A.L.E group as part of the 303S series of power supplies. While the intent of the testbed is to operate the 12 kV supplies directly from the MG set, it has been configured such that they can be operated from either the MG set or from the utility grid. The input connections to the power supplies are fed using CAM Loks and a distribution box is used to either supply the MG power or grid power after manual selection. The distribution box, shown in Figure 4.6, is designed such that only one of the two connections can be chosen, preventing any possibility of user error. Credit for this design and execution goes to the UTA Electric Shop. The connections on the left side of the box are all fed from the MG set while those on the right side are all fed from dedicated utility grid feeds.

The two 12 kVDC supplies, shown photographically in the upper two slots of the rack seen in Figure 4.7, are manufactured by TDK Lambda and are part of their 303 series of supplies. They were initially designed as capacitor chargers but are capable of being used as DC supplies if loaded with a capacitive buffer filter. To accomplish this, a 20 μF capacitor has been procured. There is still uncertainty about the amplitude of any potential future microgrid MVDC busses. 12 kV has been proposed as one potential option and there are presently studies under way to understand how best to rectify AC to 12 kV DC and how to convert power to such a voltage to any applicable loads. Though the power supplies here are likely not fully representative of how 12 kV may be generated within a future power system, it serves as a platform where power conversion technologies can be deployed and studied. These

Figure 4.6: MG or utility grid power distribution box.

supplies are shown photographically in Figure 4.7. The power supplies are controlled remotely using National Instruments (NI) LabVIEW software, discussed in further detail later.

4.2.3 100 kW, 12 kVDC Mosebach Resistive Load Bank

In order to load the 12 kV MVDC bus, a 12 kV electronic load bank was procured from Mosebach Inc. The load is a purely resistive load and was a custom design by Mosebach particularly for this effort. It is broken up into two 50 kW steps that are connected to the source using single pole vacuum contactors manufactured by Ross Engineering, model hbdc51-no-40-2-0-bd, that are capable of switching up to 10 A at 50 kV. Ross advertises these switches as having electrode life in excess of

(a) (b)

Figure 4.7: Photograph showing the installation of the two – 50 kW TDK Lambda power supplies used to convert 480 VAC to 12 kVDC (upper two supplies are the two 12 kVDC supplies and the lower three are the 1 kVDC supplies that will be discussed later.)

50,000 switching cycles at these levels. The switches were procured and shipped to Mosebach for introduction into the loads. Though the loads are designed to operate as two 50 kW loads, they can be manually reconfigured to operate at a few different power levels by altering the connections of the four independent resistive networks within the loads, shown in Table 4.1. Power levels of 50 kW, 44 kW, 32 kW, 35 kW, and 25 kW are possible with this load bank, but require manual rewiring to change.

The contactors are triggered using 24 V logic from the host controller and internal to the load is conversion of that digital signal to the 120 VAC needed to switch the contactors. A photograph of the engineering drawings as provided to UTA

Table 4.1: Possible Load Power Levels Within the Mosebach 12 kVDC Load

RA #	Resistance (Ω)	Voltage (V)	Power (W)	Amps (A)
1+2	2735	12000	50144	4.18
3+4	2735	12000	50144	4.18
2+3	3126	12000	43872	3.66
1+2+3	4298	12000	31909	2.66
1+2+4	3907	12000	35102	2.93
1+2+3+4	5470	12000	25072	2.09

are shown in Figure 4.8. It has l x w x h dimensions of 72" x 44" x 76" making them quite large. The load is integrated with digital voltage, current, and power sensors that will be transmitted back to the host DAQ and controller. A photograph of the 12 kV load is shown in Figure 4.9.

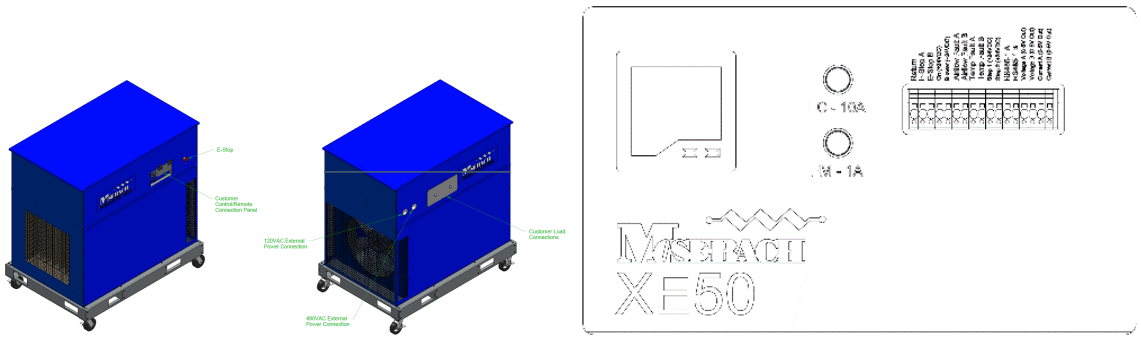

(a) (b)

Figure 4.8: Manufacture drawings of the 12 kV DC resistive load.

4.2.4 210 kW GE MV6000 Power Electronic Drive

Moving up in the diagram in Figure 4.1, the next load on the KATO MG set is a 225 kW MV 6000 power electronic converter. Immediately, the reader should be thinking about the power levels being discussed. The MG set is only capable of supplying 150 kW so the MV6000 alone is able to exceed that, not to mention the 12

Figure 4.9: Photograph of the 12 kVDC – 100 kW resistive load.

kV, 80 kW supply already discussed and the 150 kW, 1.2 kV supplies to be discussed later. Special caution is made in the over arching control system to ensure that the generator's power is never exceeded. Like the 12 kV supplies earlier, it is possible to operate the MV6000 using either power from the MG set or from the utility grid using the distribution box shown in Figure 4.6. As is done with the 12 kV supplies, the input power cables to the MV6000 are fed using manually configured CAM Loks. A photograph of the MV6000 is shown in Figure 4.10.

The GE MV6000 is typically utilized in industry as a variable frequency drive for medium-voltage motors. Though its industrial application use varies, the most dominate is in downhole drilling operations and large mining operations. A simple schematic of its internal operation is shown in Figure 4.11. Its input is a phase

Figure 4.10: Photograph of the GE MV6000 power electronic drive.

shifting transformer that steps up the 480 VAC to 4160 VAC and splits the power into 18 phases which are then fed into a 36 pulse diode rectifier. The diode rectifier rectifies the 4160 VAC to roughly 6 kVDC which is fed into a five-level IGBT inverter that generates a 3 phase 4160 VAC output. Immediately the reader may ask why a simple transformer that steps up the 480 VAC MG output to 4160 VAC wasn't used instead as ideally that would be same thing. The answer is somewhat simple and is due with the desire to emulate typical islanded microgrid diesel and gas-turbine

engine-generator sets. A real time simulator is running a model of the source to be emulated. If the mechanics of the KATO motor-generator are able to be overcome and do not impact the ability of the HIL emulator to adjust the generator's output voltage, then only a transformer would be needed here to create the 4160 VAC bus. If the generator's own dynamics cannot be overcome, then the MV6000 will allow for the source to be better emulated since its output is purely power electronic driven. That of course means that its output has a switching component to it but hopefully most of that can be simply filtered out. In normal operation, the HIL will be used to control the five-level converter such that the output AC source emulates a diesel or gas-turbine driven MG set. A custom LabVIEW-based control setup has been created for the control of the MV6000; this is discussed later. The output of the 4160 VAC emulated source will be split in two directions discussed next.

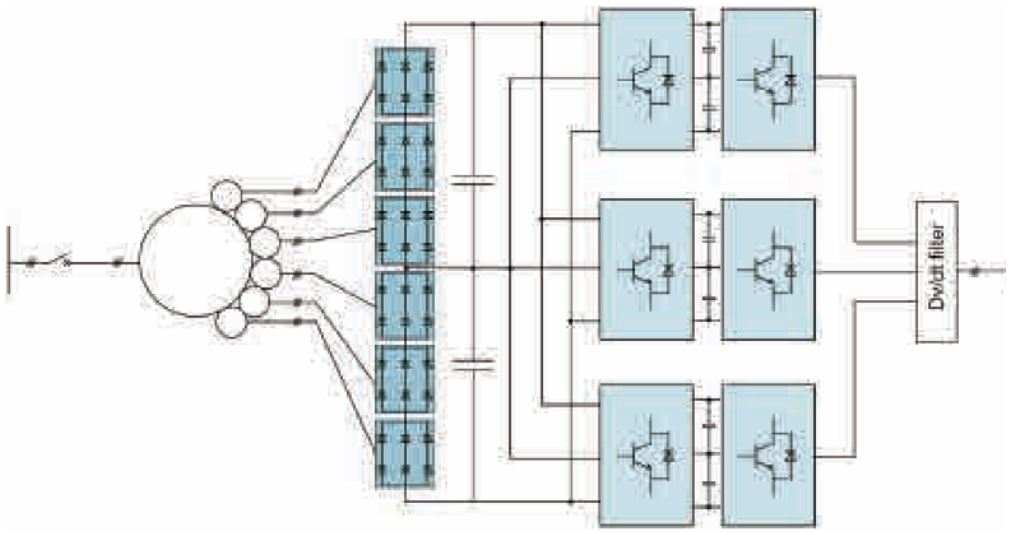

Figure 4.11: Simple schematic showing the internal operation of the MV6000. First is the 18 phase setup transformer, next is the 36 pulse diode rectifier creating a 6 kV DC link, and finally there is a five level IGBT inverter that creates the three phase 4160 VAC output.

4.2.5 4160 VAC Distribution

The MV6000's output is split two ways using a 4160 VAC distribution box. The box is simple but also complex given the high voltage involved. The box was designed collaboratively by UTA's Electric Shop and Lonestar Electric Company. A photograph is shown in Figure 4.12.

Figure 4.12: Photograph of the 4160 VAC distribution box installed in the laboratory. Each of the three blocks of connectors makes up a respective voltage phase. In each of the three blocks is three connectors. One is the input from the MV6000, one is the output to the 4160 VAC to 480 VAC transformer, and the third is the output to the 18 phase transformer/rectifier.

4.2.6 4160 VAC / 480 VAC Step Down Transformer and 350 kW, 480 VAC Mosebach Resistive Load Bank

One path the MV6000's output can take is into a 4160 VAC to 480 VAC step down transformer that feeds a 350 kW - 480 VAC electronic load. This leg is used to base load the generator and emulate many conventional power system loads. The 500 kVA transformer was procured from Maddox transformer. It is shown photographically in Figure 4.13.

The Mosebach 480 VAC load is one that is offered as a standard product. The load is a purely resistive load that is able to be stepped with load resolutions as low as 1 kW through a combination of available steps. The load is shown photographically in Figure 4.14. The load is controlled using a custom developed LabView interface operating a NI CompactDAQ unit. The load steps are controlled using 24 V logic transmitted directly from the CompactDAQ. Further discussion of this custom control setup is given later.

4.2.7 GE 18 Pulse Transformer, GE 36 Pulse Diode Rectifier, and 150kW, 6 kV Mosebach Resistive Load Bank

The second path the GE MV6000's output can take is into a GE 18 phase shifting transformer that is identical the one at the input to the MV6000 with the only difference being that its input rating is 4160 VAC instead of 480 VAC. The output of the 18 phase transformer is fed into a GE 36 pulse diode rectifier that rectifies the 18 800 VAC phases into to 6 kVDC by placing the rectified stages in series. The multi-pulse transformer and rectifier are used in place of a simple 3 phase rectifier in order to reduce the ripple in the rectified DC voltage. The transformer and rectifier were procured from GE as piece parts that had to be integrated into a single package, seen in Figure 4.15. The configuration chosen is nearly identical to

Figure 4.13: Photograph of the 500 kVA - 4160 VAC / 480 VAC step down transformer installed in the laboratory.

the way they are installed in the GE MV6000. A custom steel frame was designed that is on casters so that it can be moved around as needed. The rectifier sits above the transformer on an isolated fiberglass reinforced frame. The rectifier is designed in three blocks by GE and is easily mounted on the frame.

Forced air cooling is needed to ensure the transformer and rectifier stay below their rated thermal limits during electrical operation. An air flow rate of 160 cubic

Figure 4.14: Photograph of the Mosebach 350 kVA - 480 VAC resistive electronic load installed in the laboratory.

meters per minute is recommended to ensure safe operation. To achieve this, a 15 HP blower is used to draw air through the transformer enclosure. The port used to pull air from the enclosure is shown in Figure 4.15 and the 15 HP blower along with its associated variable frequency drive and braking resistor are shown in Figure 4.16. The forced air cooling setup is being repurposed from a previous completed project. The transformer has integrated temperature diagnostics that are monitored by the NI control system to prevent overheating.

Finally, the output of the 6 kV rectifier is fed into a custom 6 kV resistive load bank designed and fabricated by Mosebach. Two of the 6 kV loads were procured,

(a) (b)

Figure 4.15: Photograph of the 225 kW 4160 VAC / 800 VAC GE 18 phase transformer and 36 pulse AC/DC rectifier within the custom enclosure fabricated for safety and for forced air cooling. In both pictures, the transformer is below and the white rectifiers are seen above. In the left picture, the AC input and DC output ports are shown and it was taken before the frame was enclosed with polycarbonate. The rightmost figure shows the other side of the setup and the air flow port where a 4 inch tube is used to either pull or push air into the enclosure.

each of which is made up of three 50 kW load steps. They are fabricated in almost exactly the same way as the 12 kV load discussed earlier and occupy a slightly smaller physical footprint, shown in Figure 4.17. As opposed to the 12 kV load which has two 50 kW load steps, each 6 kV load has three 50 kW load steps. Like the 12 kV loads, they can be internally wired in a few different configurations to reduce their power dissipation if needed, shown in Table 4.2. Each of the three load steps are switched in using the same Ross vacuum contactors as discussed earlier in the 12 kV load. Only one of the two 6 kV loads procured is used to load the 6 kV rectifier while the other is used to load a second 6 kV bus that will be discussed later.

Figure 4.16: Photograph of the 15 HP blower, variable frequency drive, and braking resistor used to apply forced air cooling to the 4160 VAC transformer and 6 kVDC rectifier.

Table 4.2: Possible Load Power Levels Within the Mosebach 6 kVDC Load

RA #	**Resistance (Ω)**	**Voltage (V)**	**Power (W)**	**Amps (A)**
1	684	6000	50125	8.35
2	684	6000	50125	8.35
3	684	6000	50125	8.35
1+2	1368	6000	25063	4.18
1+2+3	2052	6000	16708	2.78

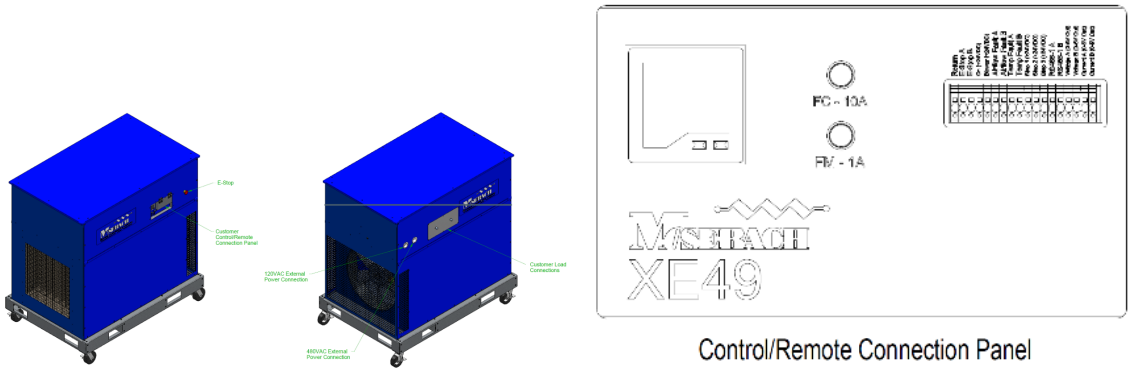

(a) (b)

Figure 4.17: Manufacture drawings of the 6 kV DC electronic load.

Figure 4.18: Photograph of the two 6 kVDC – 150 kW resistive loads.

4.2.8 150 kW, 480 VAC to 1.2 kVDC Programmable Power Supply

The final load to the KATO MG set, which is found at the upper output leg, is a 150 kW AC/DC power supply manufactured by TDK Lambda. The input to the supply is 480 VAC and its DC output is variable from 30 V to 1200 V. The power supply is of their A.L.E. 303S series and is configured in three 50 kW building blocks that operate in a master/slave assembly mode. The supplies are switch mode power supplies that utilize solid state switches, which is considerably different from the transformer rectifier method discussed above. These supplies are able to be remotely controlled using the overarching LabVIEW or OPAL-RT controller and can be used to emulate the transformer/rectifier topologies described above. UTA has previously shown that with accurate models, HIL emulation is able to very accurately replicate experimental hardware that is not present in the lab. The supplies are liquid cooled using a 14 HP closed loop water chiller and loaded using a second identical 150 kW, 6 kV DC Mosebach load that loads the 6 kV multi-pulse rectifier.

The output of the 1.2 kV power supply sources power onto a 1 kV DC bus. In order to demonstrate a battery's ability to buffer transient loads, a high power lithium-ion battery has been assembled and connected onto the 1 kVDC bus. The battery was assembled as mentioned in Chapter 2. The battery is assembled using Saft VL30AFE cells and is capable of loading roughly 96 kW continuously and sourcing 250 kW continuously. In place of the li-ion battery, UTA also possesses two 1000 VDC lead acid batteries that were assembled previously. Both lead acid batteries are able to be used in parallel but it is not possible to connect both the lead acid and the li-ion batteries onto the bus simultaneously. The intent of the battery is to either source power onto the 1 kVDC bus or to sink power from the rotating machine. In the event that transient loads are sourced, the battery can act as a base load to the rotating machine allowing it to supply continuous power, even during short periods of load

(a) (b)

Figure 4.19: Photograph showing the installation of the three – 50 kW TDK Lambda power supplies used to convert 480 VAC to 1.2 kVDC (upper two supplies are the two 12 kVDC supplies and the lower three are the 1 kVDC supplies.

inactivity, allowing acceptable power quality to be maintained within the islanded microgrid power system. A primary intention of the whole testbed is to demonstrate the ability to maintain power quality in this type of scenario and to both develop and validate the overarching system controller that is needed to achieve this goal. The 1 kV battery bus has two additional components connected to it that will be discussed next.

The first load on the 1 kVDC bus is a Chroma 17030 battery cycler. The cycler is capable of sourcing 30 VDC to 1200 VDC and 1 ADC to 700 ADC with an overall source or sink power limit of 500 kW. The system is regeneratively sinked to the

electric grid enabling its footprint to be quite small considering the power level. This unit was procured in 2014 and used as part of previous projects at UTA. In this testbed, the Chroma 17030 can either be used as a source or as a programmable load on the 1 kVDC bus. It is intended that both base loads and transient loads will be emulated using the 17030. A photograph of the Chroma 17030 is shown below in Figure 4.20.

Figure 4.20: Photograph of UTA's 1200V/700A/500kW Chroma 17030 battery cycler.

4.2.9 80kW, 1 kVDC to 6 kVDC Programmable Power Supply

The second load on the 1 kVDC bus is a programmable DC power supply manufactured that is commercially available. There is little information available about this power supply unit. In summary, the power supply is a switch mode power supply designed to accept a 700 VDC to 1000 VDC input voltage and it converts

that source voltage up to 6 kVDC at power levels as high as 80 kW continuously. This supply is used to emulate the manner in which power may be converted off the 1 kVDC bus to supply high voltage transient loads. The 6 kVDC supply is loaded with an identical resistive load bank to the one shown in Figure 4.18, discussed earlier.

4.3 Data Acquisition, Hardware in the Loop (HIL), Overarching Control

Though not explicitly part of the power conversion in the testbed, it is worth briefly discussing how the overarching control and data acquisition (DAQ) of the testbed is being achieved. There are four main COTS hardware systems being used to achieve these two tasks.

4.3.1 Thermal Monitoring

In an effort to make many simultaneous thermal measurements, a four channel Luna ODiSI Fiber Optic Sensing (FOS) system is being used. In short, the system is able to measure temperature at discrete points down the length of a dielectrically insulated fiber optic cable. Resolutions as low as 1 mm can be achieved using short fibers, less than a few meters, and resolutions as good as 5 mm can be achieved using longer fibers, as long as 50 m. In additional to temperature, the system is able to measure stress/strain of the device under test though temperature and stress/strain are not able to be independently quantified using simultaneous measurements and a device that undergoes both stress/strain and temperature changes simultaneously is not able to be accurately measured. Measurement is achieve using a laser source propagated at varying beat frequencies and reflection of the light from the fiber's own Bragg gratings is used to translate temperature into discernable data. Using the four channels, it is possible to measure every terminal of the lithium-ion battery and a few

other electronic components as well. In the future, temperatures within the MV6000, DC power supplies, load banks, and MG set will be measured using this instrument.

In addition to the Luna ODiSI FOS, thermal measurements are made using National Instrument (NI) 9213 compactDAQ (cDAQ) cards installed in NI cDAQ chassis. Each card is able to measure sixteen simultaneous thermocouple measurements at sample rates as high as 75 Hz. Type T thermocouples are distributed throughout the testbed, including on the bodies and terminals of the battery, within the loads, inside power supplies, etc.

4.3.2 Voltage and Current Instrumentation

Voltage and current monitoring is achieved using a few different DAQ systems, including NI cDAQ cards mounted in NI cDAQ chassis, NI PXI-e cards mounted in a NI PXI chassis, and the OPAL-RT HIL system. Since the cDAQ and OPAL-RT systems are used to provide real-time control of the hardware, each monitors the voltage and current waveforms it needs to make its real time decisions. The sample rate varies across systems to optimize processing speed as well as resolution needed for testbed performance analysis. Nearly all current measurements are made using closed loop Hall Effect current sensors. The primary sensors used are Harting 100 A and 300 A current sensors, each with a bandwidth of 50 kHz. Voltage measurements are made using a few different types of differential voltage probes. The first is a 1400 V, 25 MHz differential voltage probe manufactured by Pico Technology (model TA057). The second is a 7000 V, 70 MHz differential voltage probe also manufactured by Pico Technologies (model TA044).

4.3.3 Data Aquisition, Monitoring, and Control

A custom National Instruments based data acquisition and control system has been created utilizing five cDAQ chassis and one PXIe chassis. A photograph of the five cDAQs connected to their respective hardware is shown in Figured 4.21. Notice that most of the cards are connected to hardware via DSUB connectors and DSUB breakout boards.

The custom LabVIEW VIs that have been written for the cDAQs and equipment to communicate are shown below. There are five main VIs that have been created. The first, shown in Figure 4.22, is for controlling the Mosebach 480 VAC load unit, 12 kVDC load unit, both 6 kVDC load units, and the GE MV6 unit. This VI utilizes three of the five cDAQ chassis to achieve these functions. Notice from the VI front panel that the VI provides the user with feedback with respect to performance and any possible faults that are sent out by the hardware.

The second of the five VIs has been created to control the TDK-Lambda power supplies. This VI is responsible for the 1.2 kVDC supply control, the 12 kVDC supply control, and the 6 kVDC supply control. This VI is shown in Figure 4.23. Two cDAQ chassis, one chassis for the TDK-Lambda 303 series supplies in the rack (1.2 kVDC and 12 kVDC) and one chassis for the 6 kVDC power supply, are utilized to control these supplies.

The third and fourth VIs are used to operate and monitor the 1 kVDC battery systems that have been created at UTA. The first of these was supplied by NSWC Dahlgren and mildly modified for the purpose of communicating with the battery management system implemented on the lithium-ion battery. With minor modifications, this has been adapted for usage with the custom lithium ion battery's BMS at UTA. This is shown in Figure 4.24. The VI reports back all of the individual 280 cell voltages and any faults the BMS reports. The VI shown in Figure 4.25 is used to

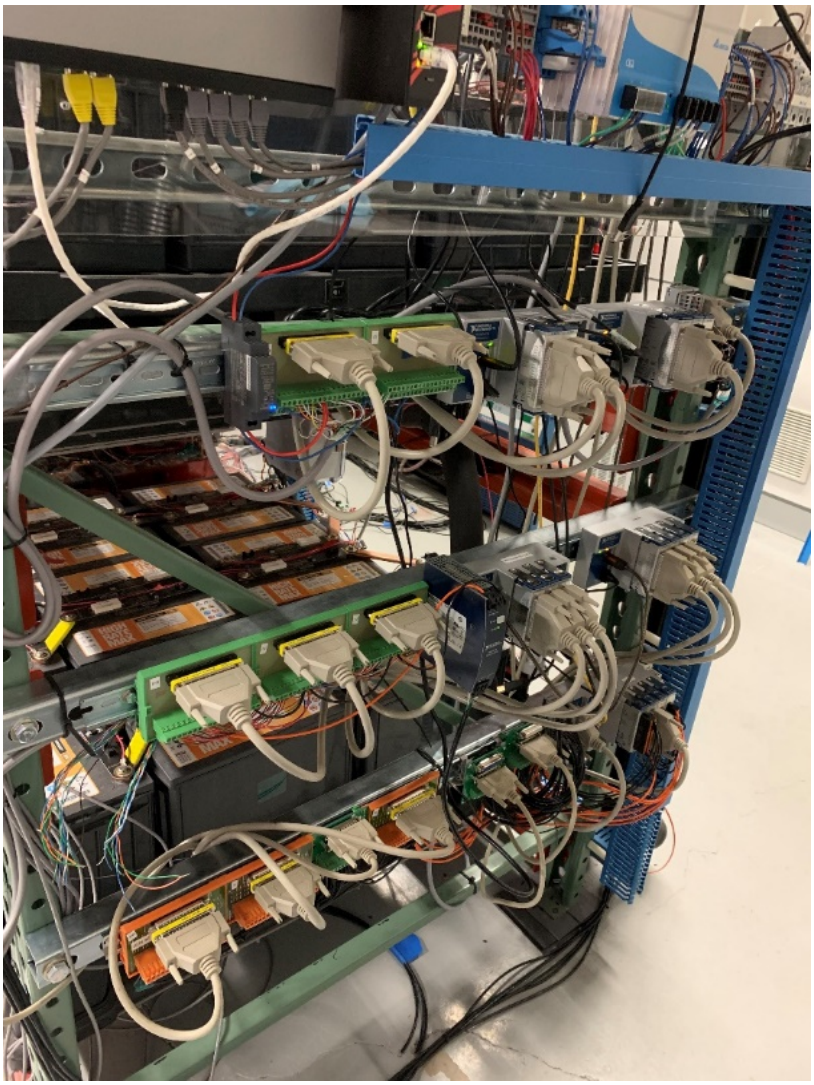

Figure 4.21: Photograph of the five NI cDAQ chassis used to provide overarching control of the three different TDK power supplies, Mosebach loads, MV6000, and M-G set.

control and monitor the battery further. It is used to actuate the individual relays within either the lithium-ion or lead acid battery, depending on which is used. The VI monitors the battery's current and individual cell voltages and provides control to open the battery in the event of a problem.

The last of the five VIs is a data acquisition VI that interfaces with the PXIe chassis to record all external voltage and current measurements for further analysis.

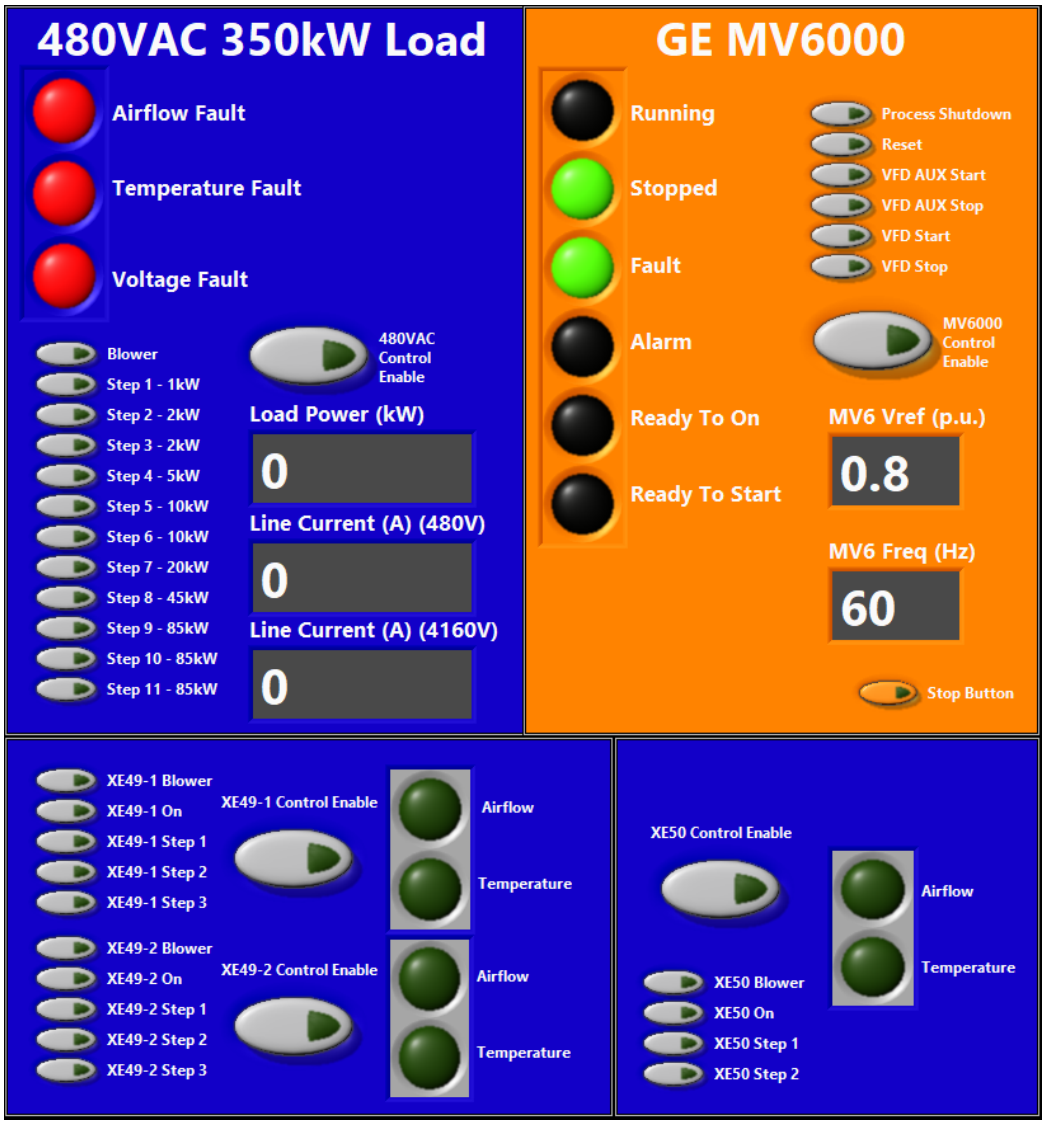

Figure 4.22: The VI used for controlling the Mosebach load units and the MV6. This VI is split into four quandrants – one for the 480 VAC load bank, one for the two 6 kVDC load banks, one for the 12 kVDC load banks, and one for the MV6 unit.

As of now, this system is set up to sample twenty-four different current or voltage measurements taken from various points in testbed at rates in excess of 20 kHz so that studies can be performed on the operation of the testbed. Graphical signals are shown as well for the operator to observe in real time. A window size of two cycles

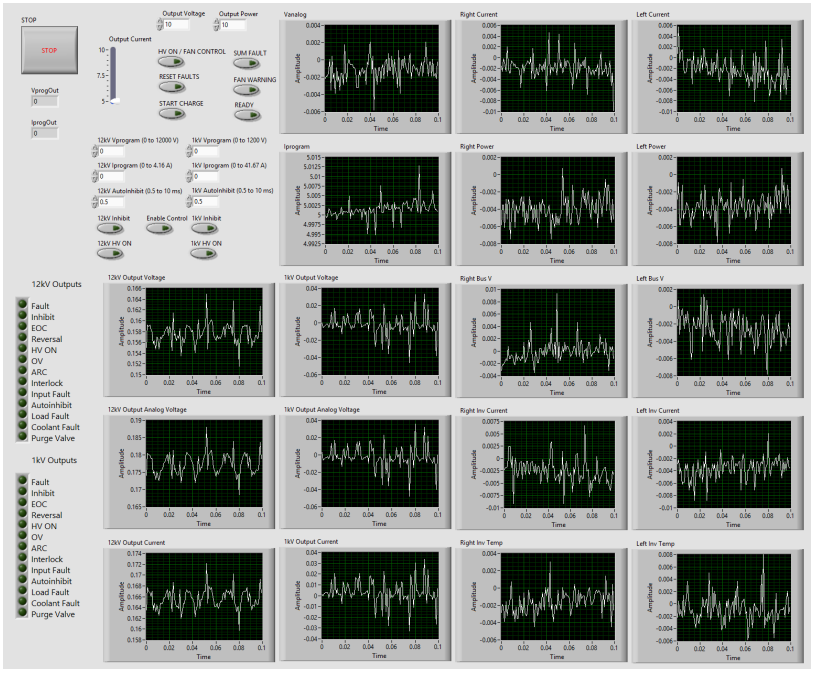

Figure 4.23: The VI created for controlling all three of the TDK-Lambda units – the 1.2 kVDC, 6 kVDC, and 12 kVDC power supplies. This VI allows for the user to monitor the analog outputs from these supplies, provide analog signals to control output current and voltage, and provides the necessary digital and analog outputs for proper operation and monitoring of the supplies.

at 60 Hz is chosen for readability. This VI is show in Figure 4.26. The data is also written to a TDMS file that analyzed later in greater detail.

4.3.4 Control Center

The testbed is controlled from a central user control panel that is separated on the other side of a wall from the testbed for user safety. Seven large panel monitors are used to provide real time display and control to the operator. A photograph of the control center is shown in Figure 4.27.

The scope of work presented here has required the procurement of a number of different electrical sources and loads that have been configured together in a testbed on which distributed generation sources and loads can studied. There is potential that

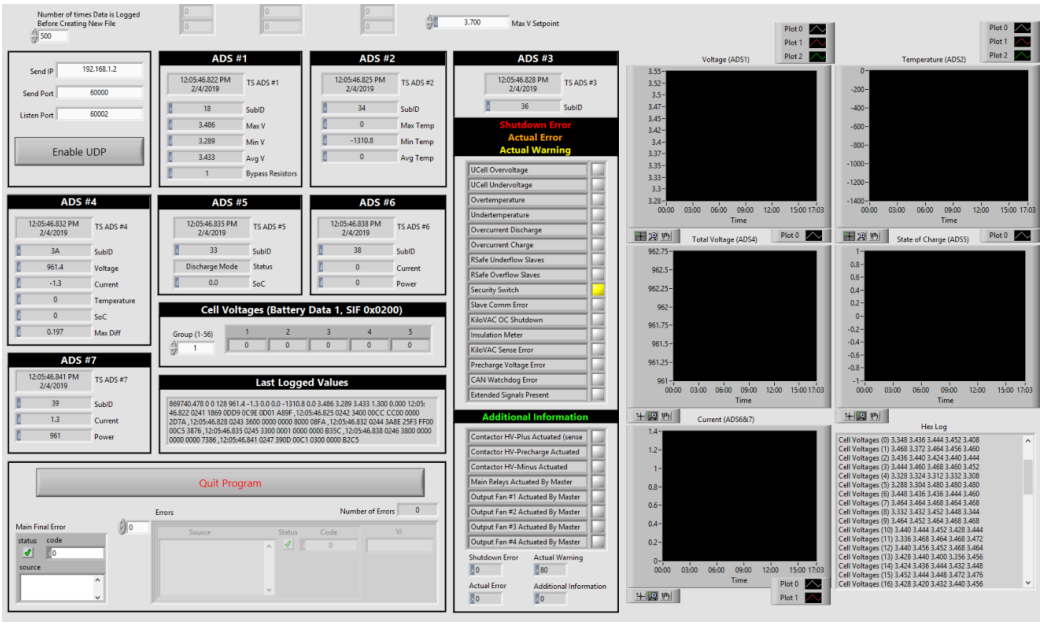

Figure 4.24: LabVIEW VI used to access and record information provided by the battery management system utilized with the 1 kVDC lithium ion battery.

future islanded microgrid systems could deploy distributed generation sources within a future architecture to meet the needs of many unique loads that will be operated transiently and simultaneously. There are many ways to configure distributed sources and loads, leaving the designers with several choices that must be made if that route is ever chosen. To adequately simulate such an environment, UTA has procured a 480 VAC electric motor – generator set from KATO, a 150 kW – 480 VAC to 1.2 kV DC programmable power supply, two 150 kW – 6 kV DC resistive load banks, one 100 kW – 12 kV resistive load bank, a 480 VAC to 4160 VAC power electronic converter, and 4160 VAC to 6 kV DC multi-pulse rectifier. Additional electronic sources and loads have been procured that were not mentioned here. Upon full operation of the energy conversion testbed, it can be utilized to demonstrate novel control architectures and to validate the utilization of hardware in the loop (HIL) for hardware emulation.

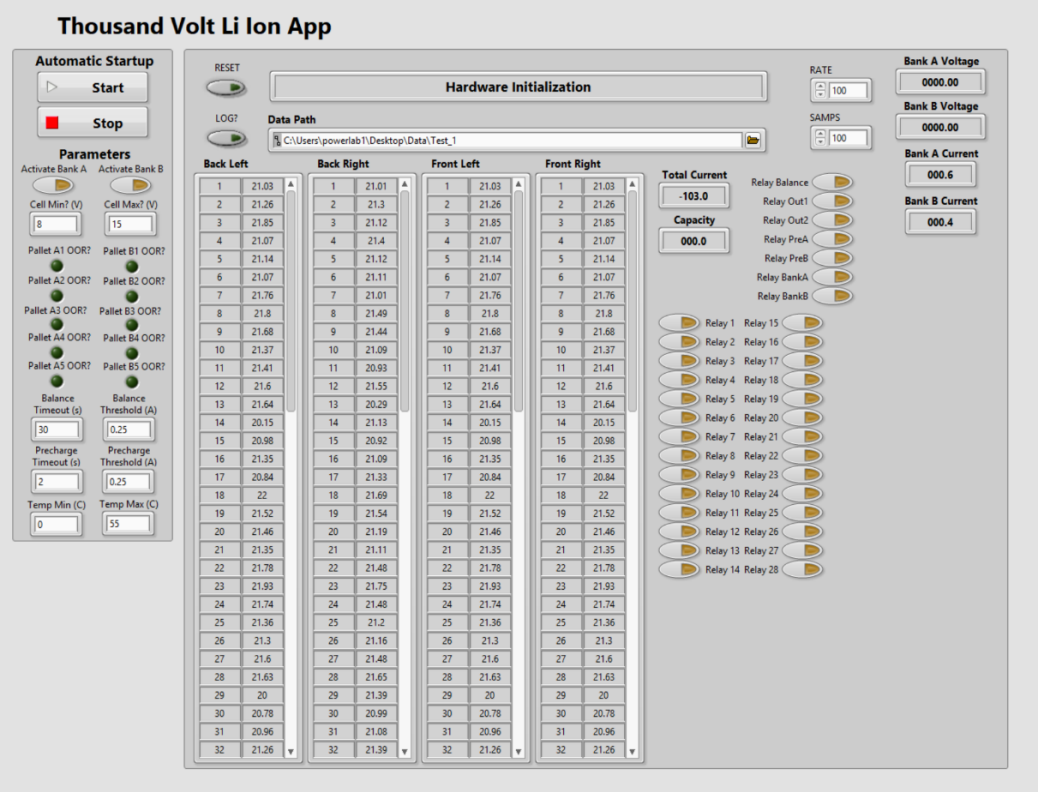

Figure 4.25: The VI used for monitoring lead acid battery voltages, output current of either battery chemistry, and for controlling the relays located between batteries/modules.

4.4 Testbed Verification and Characteristics

While various single-unit performance testing and commissioning has been performed, what follows here is a specific usage scenario that illustrates the capabilities of multiple systems and their interactions within the testbed. For the testing performed, the motor-generator is used to power the MV6000 variable frequency drive unit, as well as the 1.2 kV power supply. The MV6000 is fed into the 4160 VAC / 480 VAC transformer to step it down such that the 480 VAC load bank can be used, as well as into the multipulse transformer/rectifier setup that is connected to one of the 6 kVDC resistive load banks. The 1.2 kV supply is loaded into a 4.8 mF capacitive load. The setpoints and timing for the various pieces of equipment are as follows.

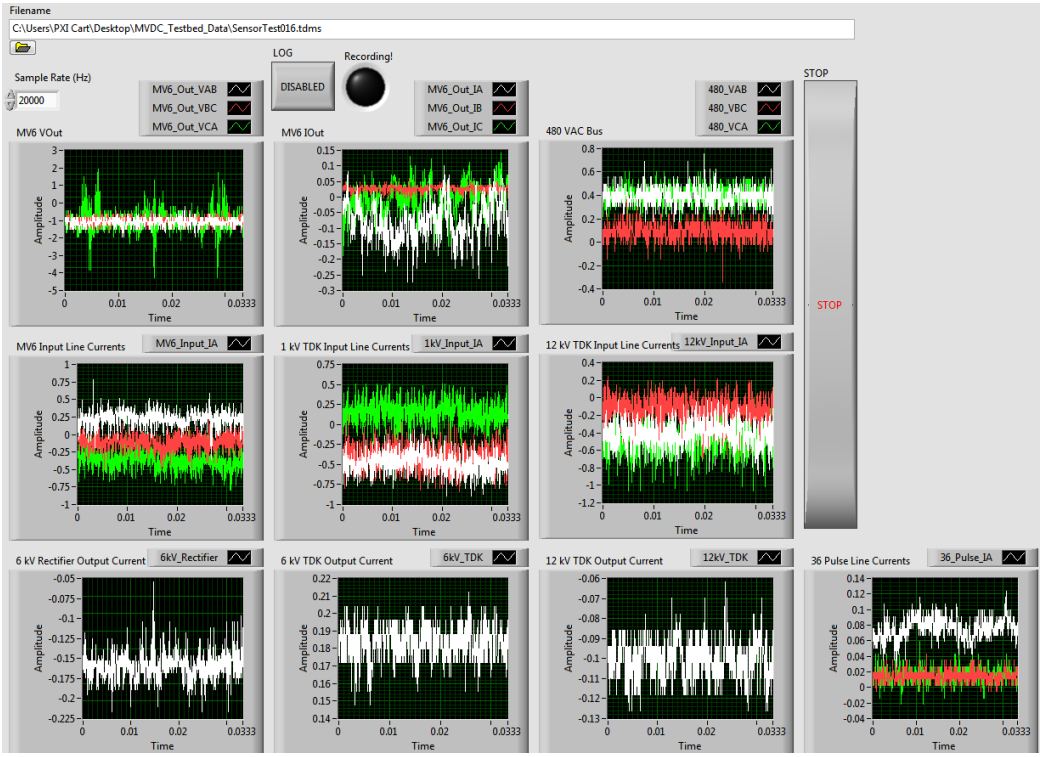

Figure 4.26: The VI created for the operation of the PXIe chassis, utilized for high rate data collection and monitoring of various signals from throughout the testbed.

KATO MG set: 480 V, 60 Hz.

MV6000: 0.8 p.u. output voltage, 60 Hz. Enabled at 8 seconds, disabled at 60 seconds.

Mosebach 480 VAC Load bank: 50 kW, unloaded to 20 kW at 30 seconds.

Mosebach 6 kV Load Bank: 0 kW, stepped to 50 kW at 19 seconds.

TDK-Lambda 1.2 kV Supply: 900 V, 45 A. Enabled at 43 seconds, disabled at 50 seconds.

4.8 mF Capacitive Load: Discharged at 54 seconds.

The data collected is shown in Figures 4.28 through 4.35. Equipment is erected in a manner to allow for various transient magnetization and start-up effects to be

Figure 4.27: Photograph of the operator control center used to control the MVDC testbed.

mitigated. Overall waveforms and transient waveforms are shown to illustrate the operational characteristics of the various equipment at steady-state and transient time scales.

4.5 Full-Scale Overarching Model

The various components in the MVDC testbed have been modeled or estimated in such a way that an overarching model of the testbed can be implemented in a MATLAB/Simulink environment. This overall model consists of a detailed model of the MV6 unit, as well as models of the 480 VAC load bank, 6kV and 12kV load banks, and KATO motor-generator set. Approximations have been made for models that are representative of the general characteristics of the TDK-Lambda power supplies.

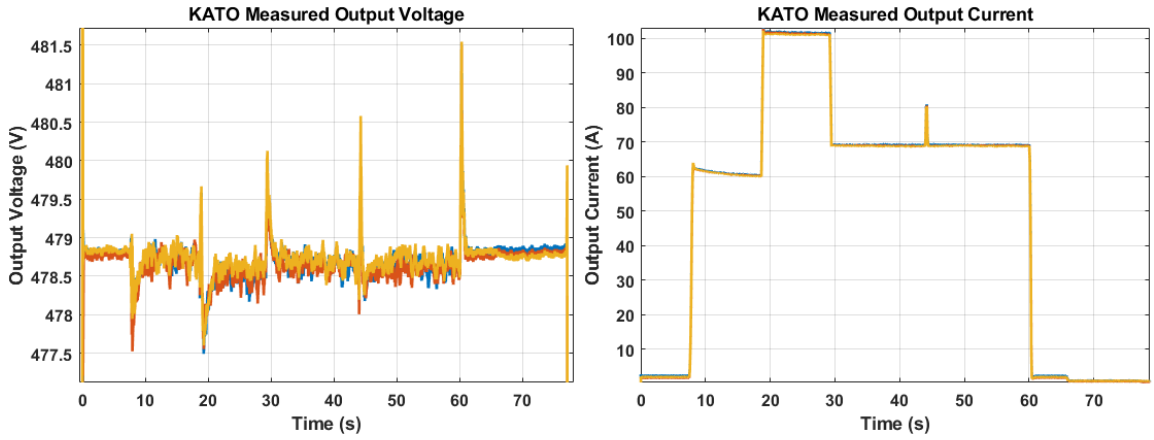

(a) (b)

Figure 4.28: Output voltage and current measured from the output of the KATO motor-generator during the test scenario.

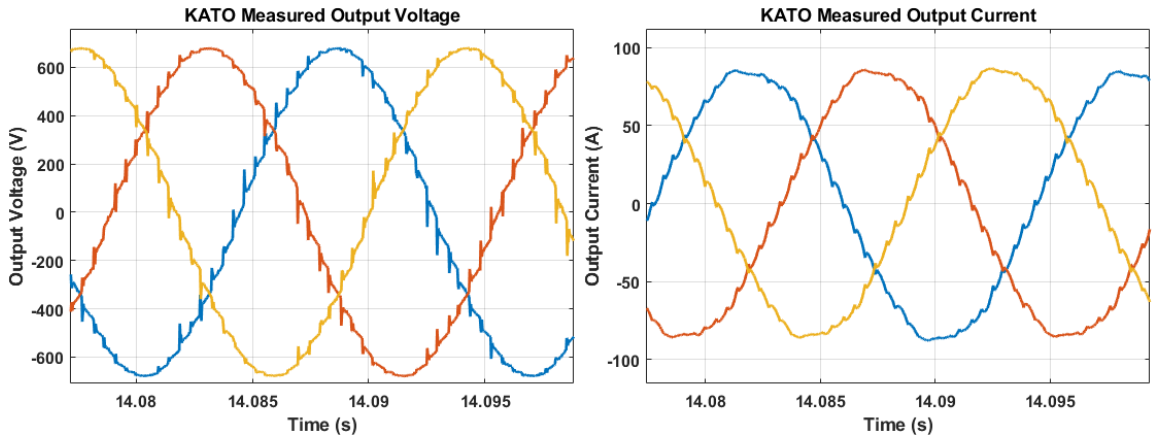

(a) (b)

Figure 4.29: Output voltage and current measured from the output of the KATO motor-generator during the test scenario, enhanced to show detail.

This is done because these systems are more of a black box, and cannot be fully analyzed within the scope of this testbed.

The first of these models to be implemented is the model of the GE MV6 unit. While not a comprehensive model of the system, this model presented here presents the main operational characteristics of the unit. This has been done to better analyze

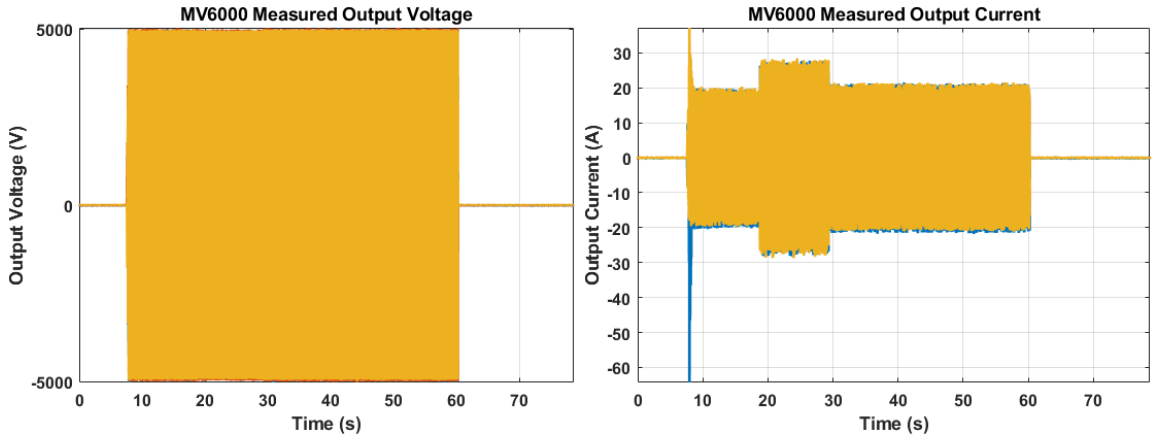

(a) (b)

Figure 4.30: Output voltage and current measured from the output of the MV6000 during the test scenario.

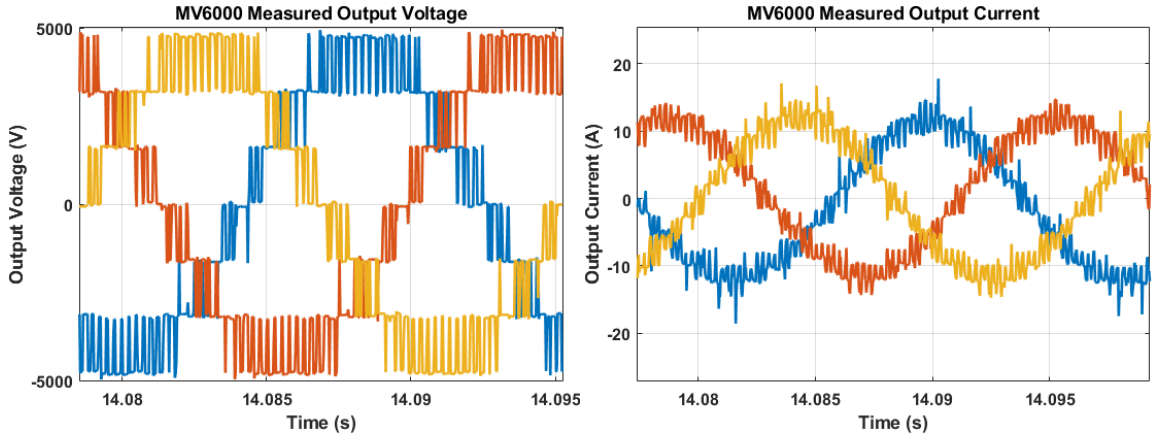

(a) (b)

Figure 4.31: Output voltage and current measured from the output of the MV6000 during the test scenario, enhanced to show detail.

and predict the operation of the unit when subjected to load profiles that are more transient in nature. The model is shown in Figure 4.36.

For the simulation that was performed on the model, a stiff 480 VAC input is used. This input is ideal, meaning that it will not droop or deviate in voltage or frequency like a rotating generation source would when loaded or unloaded. This

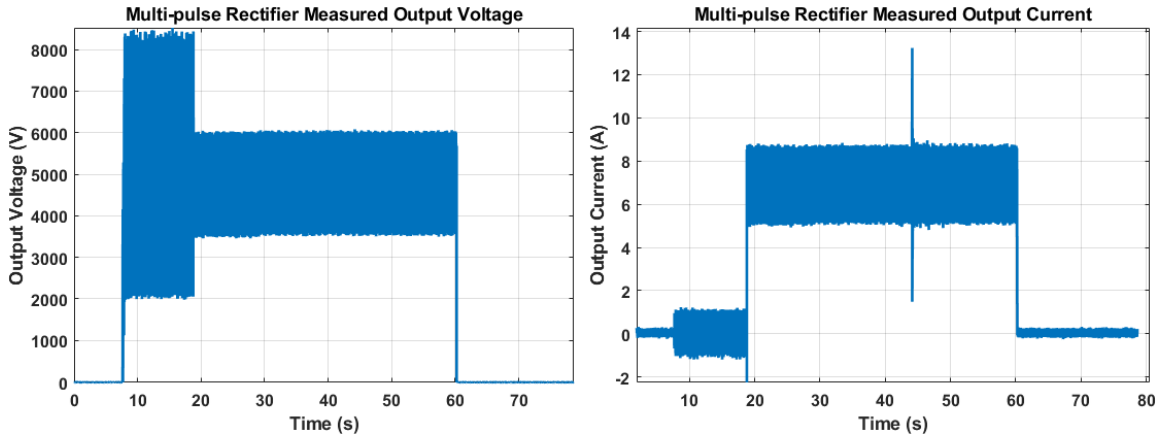

(a) (b)

Figure 4.32: Output voltage and current measured from the output of the multi-pulse rectifier during the test scenario.

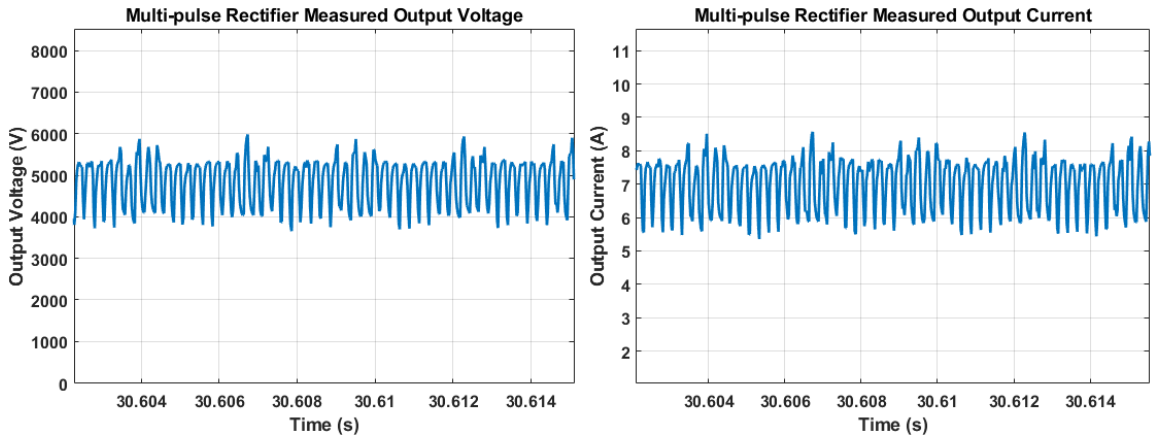

(a) (b)

Figure 4.33: Output voltage and current measured from the output of the multi-pulse rectifier during the test scenario, enhanced to show detail.

source is fed into a transformer model that represents the input transformer within the MV6 unit. Parameters have been obtained from the manufacturer's testing and characterization procedures for this transformer, and these have been implemented. This transformer takes the three phase 480 VAC input and splits it into 18 phases of 800 VAC voltages. These voltages are then passed into a collection of series-connected

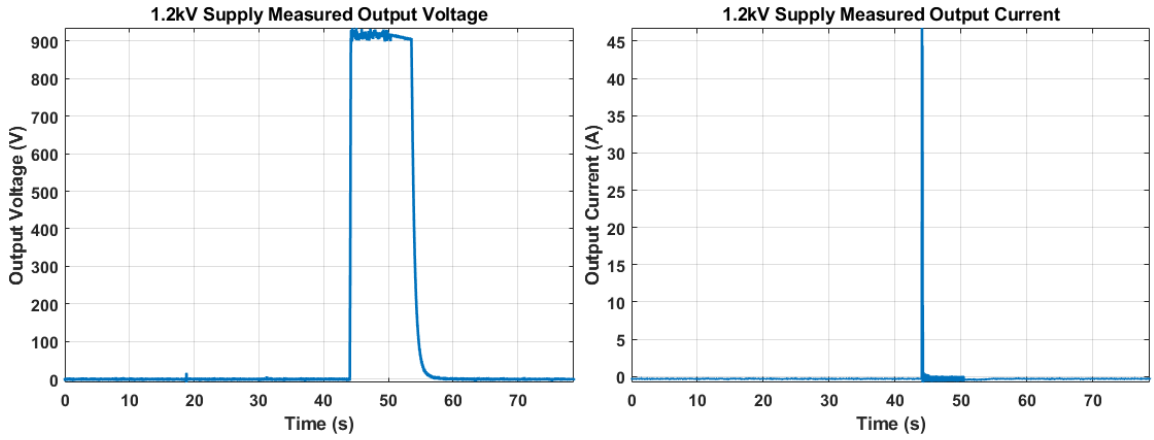

(a) (b)

Figure 4.34: Output voltage and current measured from the output of the 1.2 kV power supply during the test scenario.

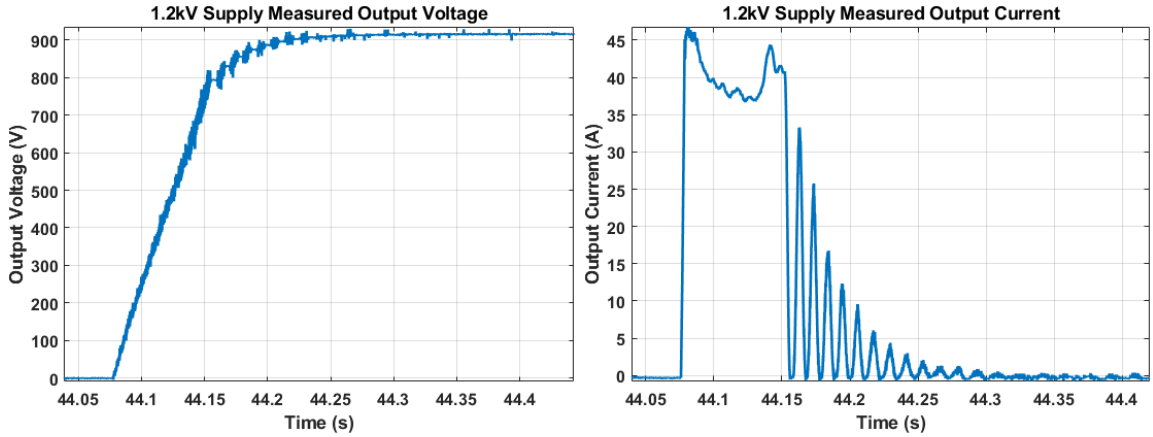

(a) (b)

Figure 4.35: Output voltage and current measured from the output of the 1.2 kV power supply during the test scenario, enhanced to show detail.

full bridge three phase rectifiers, making a total of six rectifiers for the six separate phase groups that constitute the 18 phases. The output of these rectifiers, now DC, is then fed onto a split-bus DC link capacitor, which has also been modeled. This DC link voltage has a magnitude of approximately 6 kVDC. Lastly is the inversion process within the output of the unit, in which three phase AC is generated from the

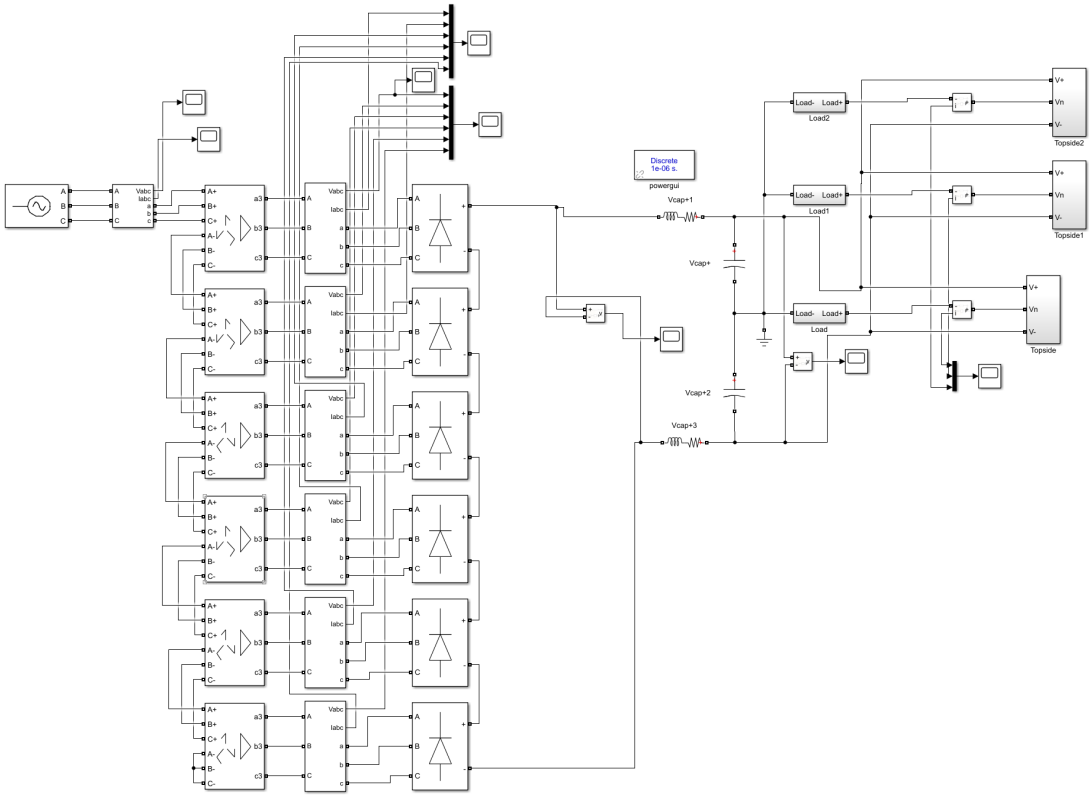

Figure 4.36: Detailed model of the GE MV6 unit created in Simulink.

DC link voltage. This is done with 5 level-converters utilizing fly-caps and IGBTs. Each phase's five-level converter is comprised of eight precisely timed half-bridge IGBT stacks that are used to generate the square wave pulses. These pulses are alternated in a sinusoidal pulse width modulation (SPWM) pattern to created a fair representation of a sinusoidal output voltage. Each of these three phases are offset by 120° from each other to create a controllable three-phase 4160VAC output that can vary in amplitude and frequency. The variance on these setpoints for voltage amplitude and frequency can be controlled in real-time utilizing an analog input

voltage generated by an OPAL-RT or similar HIL system. More is discussed on this later.

The modeled waveforms of the MV6 unit are given in Figures 4.37 through 4.39.

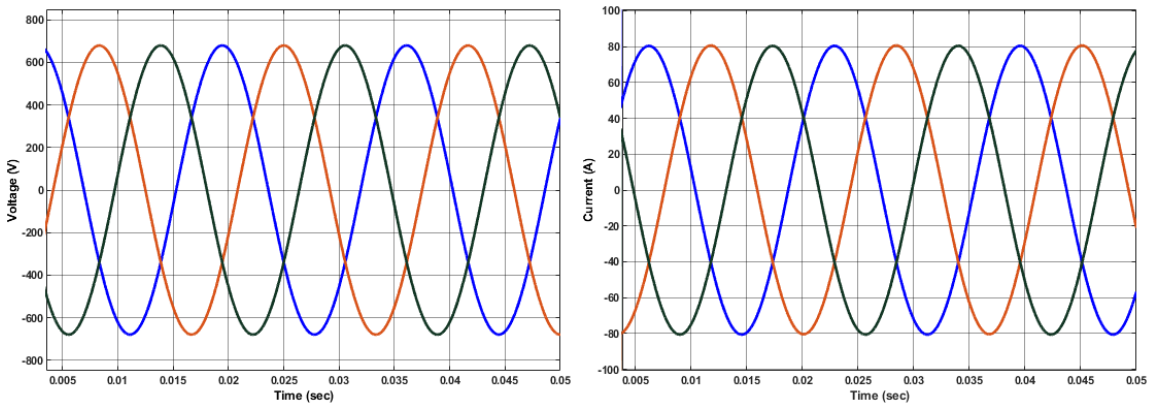

(a) (b)

Figure 4.37: Waveforms from the MV6 model showing the input voltage (a) and input current (b) into the system.

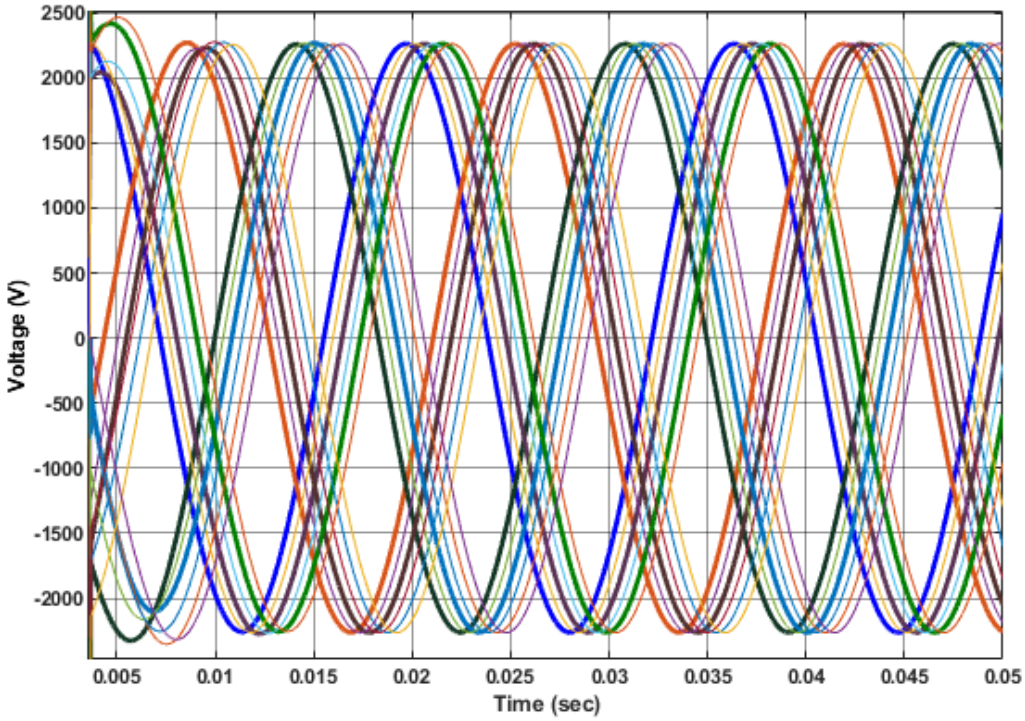

Figure 4.38: Waveformes from the MV6 model showing the 18 phases that are generated from the output of the phase-shifting transformer.

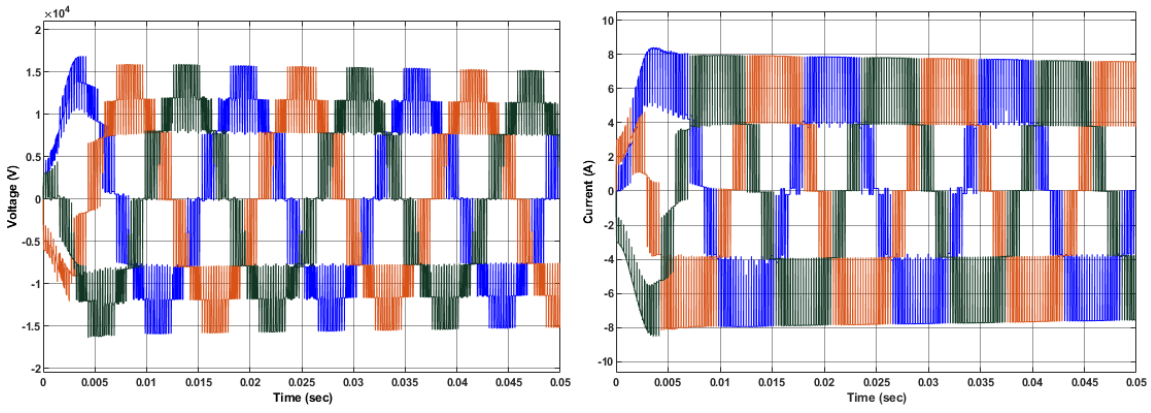

(a) (b)

Figure 4.39: Waveforms from the MV6 model showing the output voltage (a) and output current (b) from the system. The five-level converter operation can be seen here.

This MV6000 model, along with models of other subsystems, are integrated into a representative, overall model of the MVDC testbed. This model is comprised of the previously mentioned 1000 V lithium ion battery model, as well as detailed models of the KATO motor-generator set and the previously shown MV6000 model. For the other units within the testbed, representative models are used to capture the general form of operation, though these pieces of equipment (like the TDK-Lambda 303 series supplies) are a closed system that has little information available. This overall model is shown in Figure 4.40.

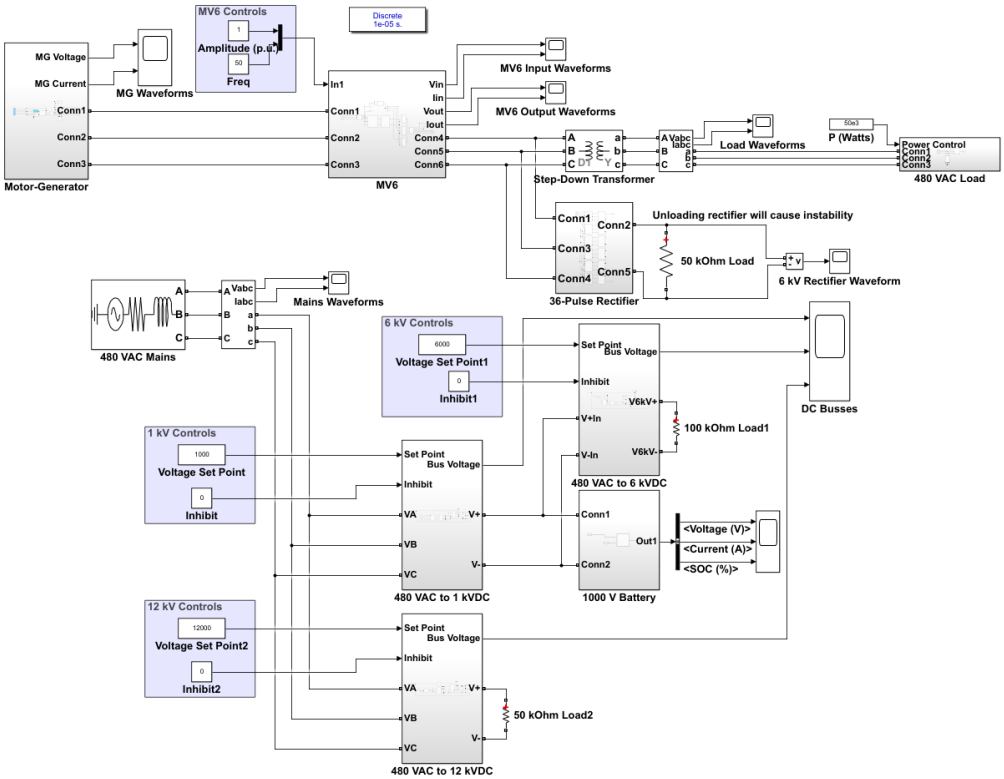

Figure 4.40: Comprehensive model of the MVDC testbed implemented in the MATLAB/Simulink environment.

4.6 OPAL-RT Real-Time Modeling and Control

An example of power hardware-in-the-loop control has been performed within the MVDC testbed to demonstrate the capabilities and possibilities of HIL integration with the real equipment. For this example, the KATO motor-generator set has been coupled with the Mosebach 480 VAC loadbank. The load has been set to start at an open circuit, then step load on 150 kW of resistive load to the output of the KATO. After enough time has passed to allow for settling of the transient to occur, the load is removed, resulting in a second transient. While this is occuring, a model of a gas turbine generator is implemented with the OPAL-RT unit that is running in real time, modeling the dynamics of the simulated gas turbine generator as it is loaded in-model. This model is derived from previous work and is shown in Figure 4.41. An example of a gas turbine generator model that could be used would be for a unit like the GE LM2500, which is massive in size and cost and entirely unfeasible for implementation in a medium-scale testbed. Instead, the LM2500 generator's defining characteristics could be implemented with a system like the KATO motor-generator coupled with OPAL-RT real-time modeling and control. This is a similar concept to utilizing a programmable power supply, but for a larger power level with a system that is comprised of a real rotating machine.

This gas turbine generator model is then used to control the voltage and frequency setpoints of the KATO motor-generator's controller, allowing for dynamic and emulative control of the actual hardware in an attempt to capture dynamics from a gas turbine generator that is not physically in the testbed. There are a total of four test scenarios. These are outlined below.

1. KATO motor-generator step loaded/unloaded with 150 kW with static setpoints of 480 VAC and 60 Hz.

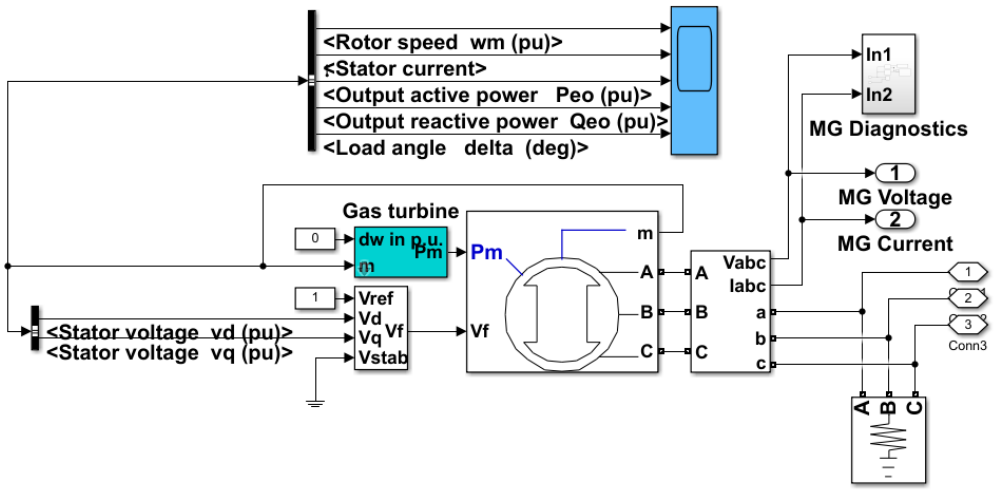

Figure 4.41: Gas turbine generator model implemented in the MATLAB/Simulink environment for the purpose of controlling the transient dynamic operation of the KATO motor-generator set.

2. KATO motor-generator controlled with gas turbine generator HIL model that has been step loaded/unloaded virtually, but with not real load.

3. KATO motor-generator step loaded/unloaded with 150 kW while simultaneously being controlled with gas turbine generator HIL model that is step loaded/unloaded virtually.

4. Gas turbine generator HIL model response to virtual step loading/unloading.

The significance of showing these four test scenarios are to highlight the performance of the KATO motor-generator's controller when given static setpoints and step loaded in case 1, and also to shown the capability and viability of HIL control with test cases 2 and 3. The raw HIL model output, derived in case 4, is the ideal response of the generator if it was replaced physically with a gas turbine generator. The resulting outcomes from these four test cases are shown in Figures 4.42 and 4.43.

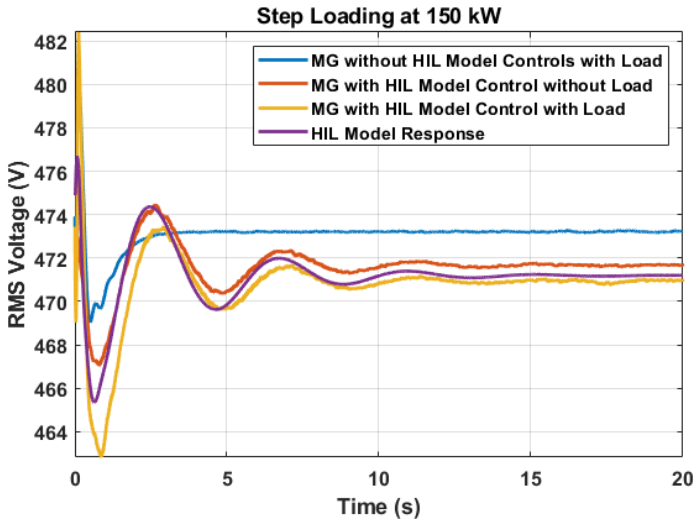

Figure 4.42: Transient voltage characteristics for diesel generator model and MG set with and without HIL model during step loading.

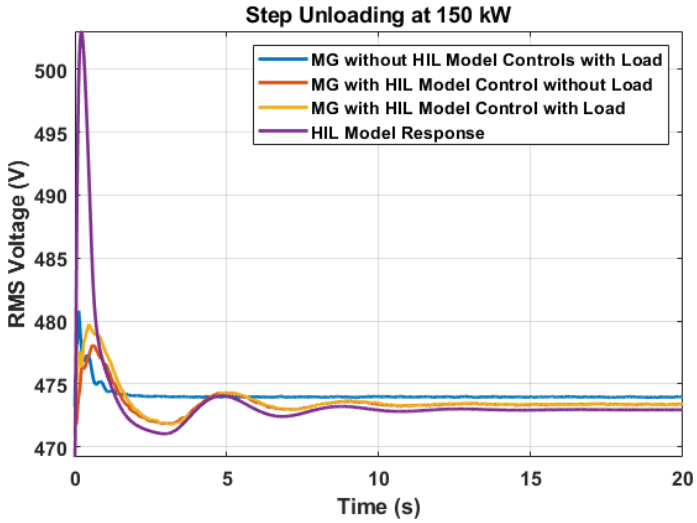

Figure 4.43: Transient voltage characteristics for gas turbine generator model and MG set with and without HIL model during step unloading.

As can be seen in Figures 4.42 and 4.43, there is good agreement in the overall dynamic operation between the HIL gas turbine model and the KATO motor-

generator set when being controlled in real time by this model. In other words, this is a viable method of operation and can set the foundation for further, more advanced evaluations to be performed with this MVDC testbed equipment.

CHAPTER 5

CONCLUSION

The work presented here has been done in an effort to construct a large-scale, representative testbed of equipment that can be used to represent microgrid systems at significant power and voltage levels, while maintaining a level of controllability and flexibility to allow for implementation of experimental techniques and to facilitate the implementation of studies concerning modern microgrid systems. Many different voltage levels have been combined, including three phase AC systems at 480 VAC and 4160 VAC, and DC systems at voltages of 1000 VDC, 6000 VDC, and 12000 VDC. A large number of these different electrical busses are generated from equipment that has been specifically designed and implemented to allow for real-time control of the bus voltages and currents for the purpose of emulation of real fielded equipment used in modern isolated microgrid systems. This includes generation sources like diesel and gas turbine generators. Controllable load banks are implemented at various points in the overall testbed system to allow for emulation of different realistic load profiles for the purpose of modeling a number of anticipated microgrid loads, such as communications equipment that can require large amounts of power for short amounts of time, or base loads such as lighting or heating systems.

Energy storage has been a major focus in the development of this medium voltage DC testbed, and the complete design process has been presented here on the design and construction of a 1000 V lithium ion battery, starting from the initial testing done to study viability at the single cell level. The design process has also included implementation of a liquid cooling solution, requiring the evaluation of cool-

ing at the module (10 cell) level. Finally, the full battery design has been discussed and the installation described, as well as the satellite systems such as thermal monitoring in the form of traditional T-type thermocouples and through an innovative fiber optic system, individual cell monitoring through a battery management system, and cell health monitoring through the usage of electrolyte-sensing technology. The conglomeration of all of these designs and systems has created a safe and robust battery system that can operate at the voltage and power levels required to incorporate energy storage at the power system level for evaluation in the overall testbed system. Work has also been shown in the modeling and simulation of this battery system at the cell level all the way to the full-scale battery for the purpose of accurately describing the electrical, thermal, and lifetime performance of this battery system.

The successful commissioning of all of the equipment has been presented, as well as efforts in the modeling of the various subsystems and overall testbed systems. These models have been designed to allow for operational analysis of the testbed to be performed, as well as for the implementation of the hardware-in-the-loop (HIL) control shown using an OPAL-RT real-time simulation platform. This system is integral for the emulation of equipment and control schemes that are not physically present within the testbed, such that these systems and schemes can be tested and vetted for viability without requiring purchase, accommodations, or control. This can allow for scaled-down evaluations to be performed for higher power systems as well, which could otherwise not be possible to evaluate in a controlled and instrumented laboratory setting. The framework for a large amount of possibilities has been created through the creation of this testbed and all of its constituent components.

This material is based upon work supported by US Office of Naval Research (ONR) under contract numbers N00014-15-1-2178, N00014-18-1-2286, N00014-17-1-2288, and N00014-16-1-3001 in support of the ONR Multi-function Energy Storage

Module (MF-ESM) program. The author would like to express thanks to ONR for their continued support. Any opinions, findings, and conclusions or recommendations expressed in this publication are those of the author and do not necessarily reflect the views of the US Office of Naval Research.

REFERENCES

[1] J. Valiani, "Power and energy storage requirements for ship integration of solid state lasers on naval platforms," *Thesis, Naval Post Graduate School*, June 2016.

[2] N. Doerry and J. Amy, "Dc voltage interface standards for naval applications," May 2018. [Online]. Available: http://doerry.org/Norbert/papers/PID3681535.pdf

[3] O. of Naval Research, "Hybrid energy storage module (hesm): Amendment 001," *13-SN-0007*, 2013. [Online]. Available: http://www.onr.navy.mil/ /media/Files/Funding-Announcements/Special-Notice/2013/13-SN-0007-Amendment-0001.ashx

[4] D. B. G. Ball and M. Hamon, "1,000 vdc utilization voltages," *SolarProfessional.com*, 2018 March. [Online]. Available: http://solarprofessional.com/articles/design-installation/1000-vdc-utilization-voltages?v=disable$_p aginationnopaging = 1.WrCOmGAm6Uk$

[5] J. Morgenson, "The commercial promise of 1,000 vdc pv design," *Solar Industry magazine*, December 2012. [Online]. Available: solarindustrymag.com

[6] "Power smoothing of large solar pv plant using hybrid energy storage." [Online]. Available: http://ieeexplore.ieee.org/abstract/document/6777277/

[7] "Off-grid power systems." [Online]. Available: http://ieeexplore.ieee.org/abstract/document/5490003/

[8] *CD UPS12 VRLA Datasheet*, CD Technologies, 2014. [Online]. Available: www.cdtechno.com

[9] N. G. S. K. D. M. N. B. . J. J. S.T. Kreger, N.A. Abdul Rahim and R. Gamber, "Optical frequency domain reflectometry: Principles and applications in fiber optic sensing," *Proc. SPIE 9852, Fiber Optic Sensors and Applications XIII, 98520T*, May 2016. [Online]. Available: https://doi.org/10.1117/12.2229057

[10] M. F. E. S. D. G. J. Bos, J. Klein, "Fiber optic strain, temperature and shape sensing via ofdr for ground, air and space applications," *Proc. SPIE 8876, Nanophotonics and Macrophotonics for Space Environments VII, 887614*, September 2013. [Online]. Available: https://doi.org/10.1117/12.2025711

[11] *ODiSI*, Luna Innovations Inc., March 2018. [Online]. Available: http://lunainc.com/odisi

[12] *Li-Ion Tamer*, Nexceris Inc., March 2018. [Online]. Available: https://liiontamer.com/

[13] N. Frank, "Safety assurance," *Electric and Hybrid Marine Technology International*, April 2017. [Online]. Available: http://viewer.zmags.com/publication/ddc293b8/ddc293b8/91

[14] *Saft VL30AFe Datasheet*, Saft Americas Inc., 2015. [Online]. Available: www.saftbatteries.com

[15] C. W. K. M. I. C. C. G.-D. D.A. Wetz, M.J. Martin and J. Heinzel, "Design of 1000 v valve regulated lead acid (vrla) and lithium-iron-phosphate lithium-ion (lfp-li) battery test beds for driving high rate, pulsed loads," *Proceedings of the 2016 Advanced Machinery Technology Symposium (AMTS)*, May 2016.

[16] ——, "Design of 1000 v valve regulated lead acid (vrla) and lithium-iron-phosphate lithium-ion (lfp-li) battery test beds for driving high rate, pulsed loads," *Naval Engineers Journal, Vol. 129, No. 3*, September 2017.

[17] D. W. K. M. C.L Williams, M.J. Martin and J. Heinzel, "High rate comparison of lithium-ion, valve regulated lead acid, and nickel metal hydride batteries for use in

pulsed power applications," *Proceedings of the 2015 IEEE International Pulsed Power Conference*, June 2015.

[18] ThermAvant Techonologies LLC., March 2018. [Online]. Available: https://www.thermavant.com/custom-thermal-solutions

[19] *650 Series Polyimide Datasheet*, Jaro Corp., 2016. [Online]. Available: http://www.jarocorp.com/docs/jaro$_6$50$_s$*eries.pdf*

[20] *FlexBMS Datasheet*, K2 Energy, 2016. [Online]. Available: http://www.k2battery.com/

[21] A. A. B. M. A. N. L. T.-S. S. S. C. M. K. J. B. D. Hill, B.H. Gully, "Detection of off gassing from li-ion batteries," *Proceedings of the 2013 IEEE EnergyTech Conference*, May 2015.

[22] Mathworks, "Battery," *R2018b Documentation*, 2008. [Online]. Available: https://www.mathworks.com/help/physmod/sps/powersys/ref/battery.html

[23] e. a. J. Thongam, "All-electric ships—a review of the present state of the art," *8th International Conference and Exhibition on Ecological Vehicles and Renewable Energies, pp. 1-8*, March 2013.

[24] "Next generation integrated power system," *NGIPS Technology Development Roadmap, Ser 05D / 349*, November 2007.

[25] B. S. J. H. D.A. Wetz, P.M. Novak and S. Donahue, "Electrochemical energy storage devices in pulsed power," *IEEE Transactions on Plasma Science, Vol. 42, No. 10, Part 2, pp. 3034 – 3042*, October 2014.

[26] B. S. D.A. Wetz and P. Novak, "Pulsed evaluation of high power electrochemical energy storage devices," *IEEE Transactions on Dielectrics and Electrical Insulation, Vol. 20, No. 4, pp. 1040 – 1048*, August 2013.

[27] D. K. J. H. J. D. S. Cohen, I.J.; Wetz, "Evaluation of a high rate hybrid energy storage module (hesm)," *Electromagnetic Launch Technology (EML), 2014 17th International Symposium on , vol., no., pp.1,7*, July 2014.

[28] O. of Naval Research, "Hybrid energy storage module (hesm): Amendment 001," *13-SN-0007*, December 2013. [Online]. Available: http://www.onr.navy.mil/ /media/Files/Funding-Announcements/Special-Notice/2013/13-SN-0007-Amendment-0001.ashx

[29] P. N. D.A. Wetz, B. Shrestha and Y. Chen, "Cycling of electrochemical energy storage devices at elevated rates," *Journal of Directed Energy, Vol. 4, No. 4, pp. 211 – 231*, July 2012.

[30] B. S. D.A. Wetz and P. Novak, "Pulsed evaluation of high power electrochemical energy storage devices," *' IEEE Transactions on Dielectrics and Electrical Insulation, Vol. 20, No. 4, pp. 1040 – 1048*, August 2013.

[31] B. S. J. H. D.A. Wetz, P.M. Novak and S. Donahue, "Electrochemical energy storage devices in pulsed power," *IEEE Transactions on Plasma Science, Vol. 42, No. 10, Part 2, pp. 3034 – 3042*, October 2014.

[32] D. W. C.L. Williams, M.J. Martin and C. Gnegy-Davidson, "Study of the impedance growth and capacity fade of high power lithium-iron phosphate, valve regulated lead acid, and nickel metal hydride batteries when cycled in high rated pulsed profiles," *228th Electrochemical Society Meeting, Electrochemical Society Transactions, Pending Publication*, October 2015.

[33] D. W. K. M. C.L Williams, M.J. Martin and J. Heinzel, "High rate comparison of lithium-ion, valve regulated lead acid, and nickel metal hydride batteries for use in pulsed power applications," *Proceedings of the 2015 IEEE International Pulsed Power Conference*, May 2015.

[34] D. Wetz and C. Westenhover, "Current sharing of lithium-ion cells in parallel," *Proceedings of the 47th Power Sources Conference*, June 2015.

[35] B. H. C. W. M. M. J.M. Heinzel, D.A. Wetz and C. Gnegy-Davidson, "Evaluations of cell parallelization effects in high power batteries utilized for directed energy weapons and electric guns," *Proceedings of the 2016 Advanced Machinery Technology Symposium (AMTS)*, September 2016.

[36] M. M. C. G.-D. D.A. Wetz, C.S. Westenhover and J. Heinzel, "Measurement of current sharing in multi-parallel cell batteries," *7th Hypervelocity Gun Weapon System Workshop*, September 2016.

[37] C. W. K. M.-I. C. C. G.-D. D.A. Wetz, M.J. Martin and J. Heinzel, "Design of 1000 v valve regulated lead acid (vrla) and lithium-iron-phosphate lithium-ion (lfp-li) battery test beds for driving high rate, pulsed loads," *Proceedings of the 2016 Advanced Machinery Technology Symposium (AMTS)*, May 2016.

[38] C. W. D. D. D.A. Wetz, M.J. Martin and J. Heinzel, "Design of two 1000 v batteries for evaluation as pulsed power prime power supplies," *7th Hypervelocity Gun Weapon System Workshop*, September 2016.

[39] D. W. I.J. Cohen, J.P. Kelley and J. Heinzel, "Evaluation of a hybrid energy storage module (hesm) for pulsed power applications," *IEEE Transactions on Plasma Science, Vol. 42, No. 10, Part 2, pp. 2948 – 2955*, October 2014.

[40] J. H. I. Cohen, D.A. Wetz and Q. Dong, "Design and characterization of an actively controlled hybrid energy storage module (hesm) for high rate directed energy applications," *IEEE Transactions on Plasma Science, Vol. 43, No. 5, pp. 1427 – 1433*, March 2015.

[41] Q. D. J. H. I. Cohen, D.A. Wetz and S. Veiga, "Fuzzy logic control of a hybrid energy storage module for system level control of cots components driving pulsed loads," *International Journal of Fuzzy Logic Systems (IJFLS) Vol.6, No.1*, January 2016.

[42] ——, "Evaluation of an actively controlled battery-capacitor hybrid energy storage module (hesm) for use in driving pulsed power applications," *6th DoD Innovative Science Technology EM Railgun Workshop*, September 2015.

[43] D. W. I. C.-J. H. B.J. McRee, D.A. Dodson and Q. Dong, "Investigation of harmonic distortion in multi-pulse rectifiers for large capacitive charging applications," *Proceedings of the 2016 IEEE International High Voltage and Power Modulator Conference (IHVPMC)*, July 2016.

BIOGRAPHICAL STATEMENT

David A. Dodson was born in Irving, Texas in 1993. He received a B.Sc. degree majoring in Electrical Engineering and minoring in Nuclear Engineering from the University of Texas at Arlington in 2015. He continued his academic work and performed research at the University of Texas at Arlington under Dr. David Wetz in the Pulsed Power & Energy Laboratory. He has been involved as a student member of IEEE and the IEEE PES. His interests include electrochemical energy storage and renewable energy technologies, power electronic systems and controls, design and research in microgrid applications, and power system design.